

# Tailoring neuroelectronic interfaces via combinations of oxides and molecular layers

Xiaobo Yuan

Schlüsseltechnologien / Key Technologies

Band / Volume 246

ISBN 978-3-95806-572-7





Forschungszentrum Jülich GmbH  
Institute of Biological Information Processing  
Bioelectronics (IBI-3)

# **Tailoring neuroelectronic interfaces via combinations of oxides and molecular layers**

Xiaobo Yuan

Schriften des Forschungszentrums Jülich  
Reihe Schlüsseltechnologien / Key Technologies

Band / Volume 246

---

ISSN 1866-1807

ISBN 978-3-95806-572-7

Bibliografische Information der Deutschen Nationalbibliothek.  
Die Deutsche Nationalbibliothek verzeichnet diese Publikation in der  
Deutschen Nationalbibliografie; detaillierte Bibliografische Daten  
sind im Internet über <http://dnb.d-nb.de> abrufbar.

Herausgeber  
und Vertrieb:           Forschungszentrum Jülich GmbH  
                                  Zentralbibliothek, Verlag  
                                  52425 Jülich  
                                  Tel.: +49 2461 61-5368  
                                  Fax: +49 2461 61-6103  
                                  zb-publikation@fz-juelich.de  
                                  www.fz-juelich.de/zb

Umschlaggestaltung:   Grafische Medien, Forschungszentrum Jülich GmbH

Druck:                    Grafische Medien, Forschungszentrum Jülich GmbH

Copyright:              Forschungszentrum Jülich 2021

Schriften des Forschungszentrums Jülich  
Reihe Schlüsseltechnologien / Key Technologies, Band / Volume 246

ISSN 1866-1807  
ISBN 978-3-95806-572-7

Vollständig frei verfügbar über das Publikationsportal des Forschungszentrums Jülich (JuSER)  
unter [www.fz-juelich.de/zb/openaccess](http://www.fz-juelich.de/zb/openaccess).



This is an Open Access publication distributed under the terms of the [Creative Commons Attribution License 4.0](https://creativecommons.org/licenses/by/4.0/),  
which permits unrestricted use, distribution, and reproduction in any medium, provided the original work is properly cited.

## Abstract

In this work we introduce a novel method to tailor the interface of neuroelectronic devices in a way that (i) it becomes biocompatible and (ii) at the same time allows a guided growth of neurons on the substrate. By using different oxides which are functionalized with the organic molecules 3-aminopropyltriethoxysilane (APTES), we can generate areas onto which neurons either adhere, grow and mature, or preferably don't adhere. Furthermore, the resulting cell-chip interface is extremely thin (molecular monolayer) and robust, and therefore promises an optimal electronic signal transfer in neuroelectronic devices.

In a first step, surface potential analyses are used to record and optimize the gas-phase deposition of self-assembled monolayers (SAMs) of APTES on SiO<sub>2</sub> and to determine the resulting change of the electrokinetic potential and charge at the solid-liquid interface. We found that (i) an adequate post-deposition treatment is crucial to the formation of perfect molecular APTES SAMs. (ii) The activation state of the SiO<sub>2</sub> surface which determines the amount of binding docking sites for the molecules, and the stability of the APTES coating is characterized by electrokinetic potential measurement.

In a second step, we demonstrate that cell adhesion and neuron maturation can be guided by patterned oxide surfaces using different oxides functionalized with an organic molecular layers of APTES. It seems that only physisorbed layers (no chemical binding) can be achieved for some oxides (Ta<sub>2</sub>O<sub>5</sub> and TiO<sub>2</sub>), whereas self-assembled monolayers (SAM) form on other oxides (SiO<sub>2</sub> and Al<sub>2</sub>O<sub>3</sub>). As a result of the different types of APTES binding and the difference in the electrokinetic potential, a large cell density contrast is obtained for SiO<sub>2</sub> and Ta<sub>2</sub>O<sub>5</sub>. The cell density and coverage with dendrites and growth cones are ~ 8 respectively ~ 3.2 times larger on SiO<sub>2</sub> compared to Ta<sub>2</sub>O<sub>5</sub> both coated with APTES.

Finally, we test the different oxides in multi electrode array (MEA) devices using the different oxides (Al<sub>2</sub>O<sub>3</sub>, TiO<sub>2</sub>, Ta<sub>2</sub>O<sub>5</sub>) as passivation and at the same time for the guidance of cell growth. Impedance measurements indicate, that, due to the thinness of the passivation, the feedlines strongly couple into the electrolyte. Nevertheless these novel MEAs work perfectly in HL-1 cell culture experiments showing smaller action potential

signals but at the same time a signal-to-noise ratio ( $\text{SNR} \approx 3$ ) which is comparable to conventional polyimide passivated MEAs. Finally, tests with neuronal cell cultures show guided cell adhesion, however the patterns chosen for the cell guidance in these experiments turn out to be too small to allow the development of neuronal networks.

In conclusion, the combination of organic SAMs and patterns of different oxides (especially  $\text{SiO}_2$  and  $\text{Ta}_2\text{O}_5$ ) allows guided neuron cell growth. Simultaneously the oxide can be used as passivation in neuroelectronic devices. This complete package could represent a promising option for the development of robust neuroelectronic devices that might enable guided neuron growth as well as a good cell-chip communication.

## Zusammenfassung

In dieser Arbeit stellen wir eine neue Methode vor, um die Schnittstelle von neuroelektronischen Bauelementen derart anzupassen, dass sie (i) biokompatibel wird und (ii) gleichzeitig ein geführtes Wachstum von Neuronen auf dem Substrat ermöglicht. Durch die Verwendung unterschiedlicher Oxide, die mit dem organischen Moleküle 3-Aminopropyltriethoxysilan (APTES) funktionalisiert werden, können wir sowohl Oberflächen erzeugen, auf denen Neuronen anhaften, wachsen und reifen als auch solche, an denen sie vorzugsweise nicht anhaften. Darüber hinaus ist die resultierende Zell-Chip-Schnittstelle extrem dünn (molekulare Monolayer) und robust und verspricht daher eine optimale elektronische Signalübertragung in neuroelektronischen Geräten.

In einem ersten Schritt werden Oberflächenpotenzialanalysen zur Erfassung und Optimierung der Gasphasenabscheidung von Self-Assembled Monolayers (SAMs) von APTES auf  $\text{SiO}_2$  und zur Bestimmung der resultierenden Änderung des elektrokinetischen Potentials und der Ladung an der Fest-Flüssig-Grenzfläche eingesetzt. Wir fanden heraus, dass (i) eine adäquate Nachbehandlung nach der Abscheidung der Moleküle entscheidend für die Bildung perfekter molekularer APTES-SAMs ist. (ii) Der Aktivierungszustand der  $\text{SiO}_2$ -Oberfläche, der die Anzahl der Andockstellen für die Bindung der Moleküle und die Stabilität der APTES-Beschichtung wiedergibt, wird durch die Messung des elektrokinetischen Potentials charakterisiert.

In einem zweiten Schritt zeigen wir, dass Zelladhäsion und Neuronenreifung durch strukturierte Oxidoberflächen unter Verwendung verschiedener Oxide, die mit einer organischen Molekularschicht aus APTES funktionalisiert sind, gesteuert werden können. Es scheint, dass für einige Oxide ( $\text{Ta}_2\text{O}_5$  und  $\text{TiO}_2$ ) nur physisorbierte Schichten (keine chemische Bindung) erzielt werden können, während sich auf anderen Oxiden ( $\text{SiO}_2$  und  $\text{Al}_2\text{O}_3$ ) selbstorganisierte Monoschichten (SAM) bilden. Infolge der verschiedenen Arten der APTES-Bindung und des Unterschieds im elektrokinetischen Potential ergibt sich für  $\text{SiO}_2$  und  $\text{Ta}_2\text{O}_5$  ein großer Zelldichtekontrast. Die Zelldichte und die Bedeckung mit Dendriten und Wachstumskegeln ist auf  $\text{SiO}_2 \sim 8$  bzw.  $\sim 3,2$  mal größer als auf  $\text{Ta}_2\text{O}_5$ , beide wurden mit APTES beschichtet.

Schließlich testen wir die verschiedenen Oxide in Multi-Elektroden-Arrays (MEA) mit den

unterschiedlichen Oxiden ( $\text{Al}_2\text{O}_3$ ,  $\text{TiO}_2$ ,  $\text{Ta}_2\text{O}_5$ ) als Passivierung und gleichzeitigen Steuerung des Zellwachstums. Impedanzmessungen zeigen, dass aufgrund der Dünne der Passivierung die Zuleitungen stark in den Elektrolyten einkoppeln. Dennoch funktionieren diese neuartigen MEAs in HL-1-Zellkulturexperimenten einwandfrei. Sie zeigen zwar kleinere Aktionspotentialsignale, aber besitzen gleichzeitig ein Signal-Rausch-Verhältnis ( $\text{SNR} \approx 3$ ), das mit herkömmlichen polyimid-passivierten MEAs vergleichbar ist. Abschließend zeigen Versuche mit neuronalen Zellkulturen eine geführte Zelladhäsion, jedoch erweisen sich die für die Zellführung in diesen Experimenten gewählten Strukturen als zu klein, um die Entwicklung neuronaler Netzwerke zu ermöglichen.

Zusammenfassend lässt sich sagen, dass die Kombination von organischen SAMs und Strukturen aus unterschiedlichen Oxiden (insb.  $\text{SiO}_2$  und  $\text{Ta}_2\text{O}_5$ ) ein geführtes Neuronenzellwachstum ermöglicht. Gleichzeitig kann das Oxid als Passivierung in neuroelektronischen Bauelementen verwendet werden. Dies Gesamtpaket könnte ein vielversprechender Weg für die Entwicklung robuster neuroelektronischer Bauelemente sein, die ein geführtes Neuronenwachstum sowie eine gute Zell-Chip-Kommunikation ermöglichen könnten.

## CONTENTS

1. Introduction.....	1
2. Theoretical background and state of the art.....	5
2.1 Cell-substrate interface .....	5
2.1.1 Cell-substrate adhesion.....	6
2.2 Engineering the cell-substrate interface .....	7
2.2.1 Engineering the cell-substrate interface towards biocompatibility .....	7
2.2.2 Engineering the cell-substrate interface towards guided growth .....	8
2.3 Surface functionalization with organic SAMs.....	13
2.3.1 Silane SAM on oxides .....	14
2.3.2 The role of the functional group .....	17
2.4 Electronic cell-chip coupling.....	19
2.4.1 Action potential and cell-electrolyte interface.....	20
2.4.2 Electrode-electrolyte interface.....	22
3. Sample preparation, characterization and experimental techniques .....	26
3.1 Deposition techniques.....	26
3.1.1 Molecule layer deposition.....	26
3.1.2 Atomic layer deposition.....	29
3.1.3 Electron beam evaporation .....	31
3.2 Lithography and lift-off technique.....	32
3.2.1 Design.....	32
3.2.2 Lithography and lift-off.....	33
3.2.3 Etching.....	35
3.3 Characterization methods .....	38
3.3.1 Ellipsometry.....	38
3.3.2 Contact angle measurements.....	39
3.3.3 Surface potential measurement.....	41
3.3.4 X-ray photoelectron spectroscopy.....	43
3.3.5 X-ray diffraction .....	44
3.3.6 Scanning electron microscope.....	45
3.3.7 Fluorescence microscopy .....	46
3.4 Cell culture .....	48
3.4.1 Cortical neuron culture .....	48
3.4.2 HL-1 cell culture.....	49
3.4.3 Live-dead staining.....	49
3.4.5 Critical point drying .....	50
3.5 Electrical characterization .....	51
3.5.1 Multi electronic arrays.....	51

3.5.2 MEA Encapsulation.....	52
3.5.3 BioMAS.....	52
4. Results and discussion.....	54
4.1 Vapor-phase deposition and electronic properties of APTES SAMs on SiO <sub>2</sub> .....	54
4.1.1 Deposition of self-assembled APTES monolayers .....	55
4.1.2 Titration analysis .....	61
4.1.3 Evaluation of the electrokinetic charge.....	62
4.1.4 Conclusion .....	66
4.2 Guided neurons growth on patterned functionalized oxides.....	66
4.2.1 Functionalization of different oxides with APTES.....	67
4.2.2 Neuronal cell growth on SiO <sub>2</sub> and Ta <sub>2</sub> O <sub>5</sub> .....	70
4.2.3 Guided cell growth on patterned oxides.....	74
4.2.4 Conclusion .....	78
4.3 Cell-chip coupling on ALD passivated MEAs.....	80
4.3.1 Development and characterization of MEAs.....	80
4.3.2 Cell chip coupling for the different MEAs.....	88
4.3.3 Neuron cultures on ALD MEAs .....	96
4.3.4 Conclusion .....	98
5. Conclusion and outlook.....	99
References.....	103
Acknowledgements.....	112

# 1. Introduction

Already in the ancient times, human beings have tried to replace nonfunctional or damaged parts of their bodies. Even though less knowledge on medical sterilization, or foreign body reaction was present, people used different materials like wood or metals as substitute of arms or legs. For instance, Marcus Sergius, a Roman general, was the first recorded person in the history using a prosthesis. His right hand was cut in the Second Punic War (218 to 201 BC) and replaced by an iron hand as a substitution to hold his shield. In fact, many East Asia people, with their different culture background compared with Europe, are deeply impressed by the famous pirates' character captain Hook (originate from the famous pirate Edward Thatch) with his wooden prosthetic leg and metal hook. For sure, by that time, the refunction of the human bodies via this simple prosthesis was strongly limited. However, even with the development of modern technology the functionality of modern prostheses are still very limited. This could change, if prostheses could be directly addressed by the nervous system of the body. The signal transfer from sensors in the prosthesis to the nervous system would be the ultimate step for a perfect substituting prosthesis. This innovation would require a perfect and stable neuroelectronic interface between prosthesis and neurons of the human body.

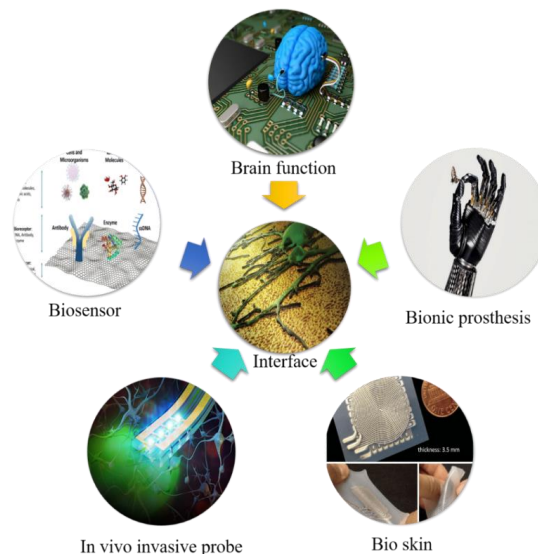


*Figure 1.1 Schematic of the different fields of neuroelectronic applications, ranging from brain function investigation, bionic prosthesis, artificial skin, in vivo invasive shank and biosensor, all the listed neuroelectronics request or pose a strong demanding of the interface. Individual images are taken from [1-6].*

Neuroelectronic devices, for example neurocognitive prostheses, which can sense or modulate neuron function in order to reconstitute or improve moving functions or cognitive processes, have been largely investigated. Implantable neurocognitive brain-computer interfaces have been proposed to help treatments of strokes, brain injuries and Alzheimer's diseases. These devices have to be able to transfer signal information between neuron cells and the electronic implants. Also, artificial skin in combined with implanted sensors can help a person to get back the sense of feeling and touching by picking up the signal via sensors and feed it into the nervous system. In fact, the application of neuroelectronic devices is quite broad, ranging from the investigation of human brain function, controlling of prosthetic limbs, wearable artificial skin, deep brain stimulation probes and various lab-on-chip biosensors for monitoring the health condition (Figure 1.1).

However, in despite of the fruitful prospect of the neuroelectronic devices, the most serious obstacle for most applications is given by the interface between the electronic and the cell. This interface has to fulfil a number of important requirements:

- It should enable a good cell-electrode coupling, which allows a suitable transfers of the signal information between the cells system and the external device.
- It should be biocompatible (non-toxic) and not lead to foreign body response (FBR).
- It should be robust and withstand a long-term use.

With the purpose to achieve this aim, quite a lot of approaches have been tested. The most representative techniques are based on:

- Modification of the surface of the electronics with extracellular matrix (ECM) proteins for instance, laminin, collagen or fibronectin or
- Tailoring the surface of the electronic contact with polypeptides like ploy-L-lysine (PLL) and ploy-D-lysine (PDL).

Although ECM proteins and polypeptides are probably the most natural way to functionalize the surface, they still have drawbacks, for instance:

- ECM proteins are macromolecules which will lead to a few hundred nanometer [7] distance between sensing electrodes and cells. Moreover, ECM proteins can easily change their conformation and become denatured in a harsh environment at the electrode.
- Polypeptides (Ploy-L-lysine (PLL) and Ploy-D-lysine (PDL)) also lead to a considerable distance between cells and electronics [8] and since it is only physically adsorbed, it easily peels off with the cells and, thus, strongly reduces the contact.

An Alternative is given by a coating of the electronic contact with a self-assembled monolayer (SAM). This layer can form a thin, stable, robust, reusable and biocompatible surface for neuronal devices, as shown in this work. SAMs of organic molecules are monolayers of a typical thickness of nanometer or below. They can be used to mimic the ECM proteins for neuron adhesion.

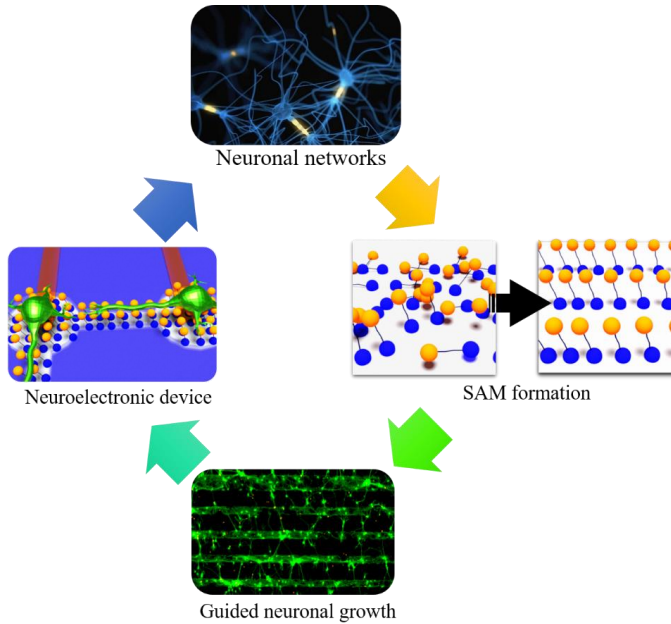


*Figure 1.2 Scope of this work, aiming a guided neuronal networks and starting with the analyses of the SAM formation, guided neuronal growth on different APTES coated oxides, finally, the test of neuroelectronic patterns. Neuronal networks' image taken from [9].*

In this work, we demonstrate that neuroelectronic interface can be tailored via combinations of oxides and SAMs of a short and simple organic molecule (3-aminopropyltriethoxysilane (APTES)) to obtain areas of different oxides onto which neurons either adhere or preferentially not adhere. This way we obtain a robust, reusable interface for guided cell growth, which provides a good and stable cell adhesion at predefined areas, for example, the electronic contacts. The precondition including the growth of the SAMs, comparison of different oxides and their cell compatibility are pioneered and discussed in this work.

This work is structured in the following parts:

**Chapter 2** provides fundamentals of the theoretical background relevant to this field, starting with the cell-substrate adhesion process, techniques to improve the cell adhesion

ability of surfaces, patterning technologies for guided cell growth, basic information on the formation of SAMs, and the properties of cell-substrate interface.

**Chapter 3** describes the fabrication and patterning techniques, characterization methods and cell culture recipes used in this work.

**Chapter 4** represents the discussion of the results separated in three sections (Figure 1.2):

- Chapter 4.1 discusses the formation and electronic characterization of monolayers of APTES on SiO<sub>2</sub>.
- Chapter 4.2 shows a guide neurons growth on test structures fabricated by patterned and oxides functionalized with APTES.
- Chapter 4.3 investigates the cell-chip coupling for HL-1 cells and guided cell growth for rat cortical neurons on a new concept of neuroelectronic devices - ALD oxide passivated MEAs.

**Chapter 5** provides the results and an outlook for future improvements.

## 2. Theoretical background and state of the art

In general, interfaces play a very important role in bioelectronics. Especially in neuroelectronics, the interface between cells and the inorganic electronics has to be robust, biocompatible, and should also allow a large electronic signal transfer, which requires adequate mechanical, chemical as well as electronic properties of the interface. This leads to a strong requirement in engineering suitable neuroelectronics interfaces for the guided cell growth on substrates and electronic devices.

In this chapter, we will highlight the theoretical background and state-of-art of engineering the cell-substrate interface. Starting with the fundamental information concerning cell-substrate interface in chapter 2.1, the state-of-art of engineering the interface is shown in chapter 2.2. In chapter 2.3 we offered a detailed introduction to self-assembled molecules that can be used to fabricate thin films and coatings with on-demand tailored compositions and architectures in a highly controlled way. Finally in chapter 2.4, the basic information of electronic cell-chip coupling is shown.

### 2.1 Cell-substrate interface

Cell-substrate interfaces are essential in cell communication and stimulation, and are of fundamental importance in the development and maintenance of tissues. A huge amount of investigation has been developed on the factors that could have an impact on the cell-substrate interface, including the surface chemistry, topography, mechanical property and stiffness. These physical and chemical factors affect the adhesion, spreading and shape of the cell [10].

Since the micro-fabrication techniques which was initially developed in semiconductor and electronics industry, came into use for the study of the cells' behavior on micro- and nano-structured surfaces a few decades ago [11]. Many studies are performed to investigate the interaction between cell and surfaces [12-19]. It turned out that cellular functions can be affected and sometimes even improved by mimicking the extracellular matrix (ECM) molecules. Thus the substrate can not only be used as a support but also guides cell adhesion, proliferation, and spreading due to physical or chemical stimulations [15]. Depending on the cell type, pattern size and geometry, stiffness and chemical properties of the substrate, substrate topography can affect the cellular functions [20]. Furthermore, nanoscale topographies affect the cell growth directly since they possess a similar size compared to ECM proteins like fibronectin, collagen and laminin [20].

### 2.1.1 Cell-substrate adhesion

Cell adhesion represents the cell's ability to stick to another cell, an extracellular matrix (ECM) or a bare substrate. The affinity of cells to a substrate represents an important issue for the design and development of biomaterial. In a static medium culture, the process of cell adhesion can be subdivided into three stages (Figure 2.1):

- (i) Initial attachment of the cell to the substrate,
- (ii) Flattening and spreading of the cell,
- (iii) Formation of a focal adhesion of the cell on the substrate.

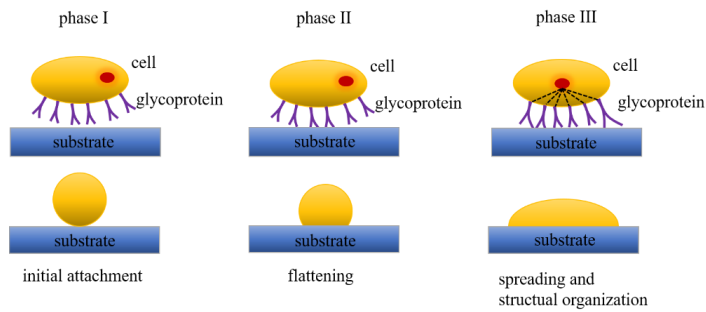


Figure 2.1: Schematic of the different phases of cell-substrate adhesion, adapted from [21].

*Phase I:* The adhesion property of cells in stage I is dominated by electrostatic interaction that is mainly due to the fact that the glycoproteins on the cell membrane are negatively charged compared to the substrate, therefore a positive charged surface is more attractive to the cells. Studies show that moderately hydrophilic surfaces lead to a better adhesion, spreading, proliferation, and differentiation of cells on a surface [22, 23]. For example, the attachment and spreading of osteoblast and fibroblast can be enhanced when the substrate's surface is positively charged compared to negative and neutral [24].

*Phase II:* Following the initial attachment, cells continue to flatten and spread on the substrate, resulting in a decrease of cell height and an increase of contact area. For example, the contact area of rabbit articular chondrocyte with the substrate increases by a factor 3 within 6 h [25].

*Phase III:* Finally in this process of adhesion, the cell spreads beyond the area of the spherical cell. This spreading process requires a continuous adhesion process with reorganization and distribution of the skeleton around the cell's body edge. The cells will finally reach their maximum spread area via expansion and reaching a strong adhesion [21, 26].

## 2.2 Engineering the cell-substrate interface

As indicated before, there are many factors that affect the cell adhesion, such as surface chemistry, topography, stiffness and so on. By changing one or more of these factors, the cell-substrate affinity properties can be modified. In fact, for neuroelectronic applications, the engineering of the cell-substrate interface has been widely investigated in order to achieve biocompatibility. This will be sketched in chapter 2.2.1. Furthermore, the ability to construct patterns with different cell-substrate affinity, a network of cells or even guided growth of cells can be achieved. Detailed information on ways to obtain guided growth will be provided in chapter 2.2.2.

### 2.2.1 Engineering the cell-substrate interface towards biocompatibility

It has been repeatedly shown that the cell-substrate adhesion depends strongly on the physic-chemical properties of the material surface. The chemical composition at the surface represents an important factor for the surface energy, polarity, wettability, surface potential and as a consequence for the cell-substrate interaction [27] (Figure 2.2).

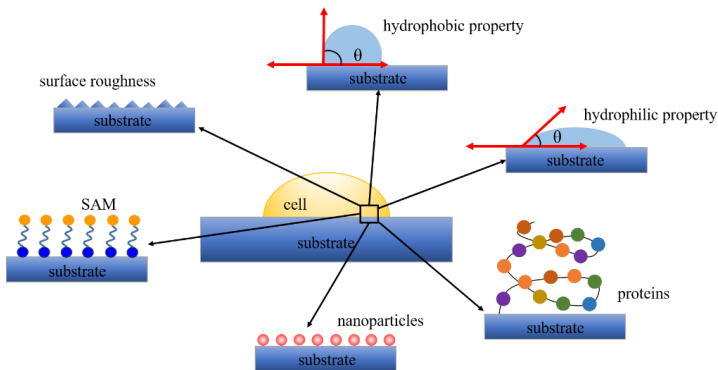


*Figure 2.2: Schematic of different physic-chemical properties that have an influence on the cell-substrate interaction.*

For example, the polar functional groups on the surface increase the energy, and wettability of the material, and support the adhesion and growth of cells on the surface [28]. If the surface is hydrophobic, the cell adhesion protein is adsorbed in a denatured configuration, thus specific amino acid sequences which should be working as ligands for adhesion receptors, will not or only partly be accessible. Then receptors cannot cluster into focal

adhesion plaques and associate with other structural and signaling proteins. Whereas, on moderate hydrophilic surfaces, proteins are adsorbed in a more natured and organized way. The receptors then cluster into focal adhesion plaques and communicate with other focal adhesion proteins and the actin cytoskeleton [29, 30].

Various biomolecules [31] and nanoparticles [32] have been widely used in regulating cell-substrate adhesion. For example, in one study fibronectin patterns are designed with the structures of circles, squares, rectangles, pentagons and stars, and the cells are distributed on these structures [33]. Gold nanoparticles significantly increased the attractiveness of the polyethylene surface for the adhesion and growth of rat vascular smooth muscle cells [34].

Self-assembled monolayers (SAMs) are highly controllable in modifying surfaces and have been employed to mimic the ECM for cell-related studies. On self-assembled monolayers terminated with positively charged  $-NH_2$  groups, a much higher number and larger area of bovine aortic endothelial cells are obtained than on the negatively charged  $-COOH$  groups [35]. The negative charge seems to reduce the cell-material adhesion and also the cell-to-cell adhesion [36-38]. Sulfonate groups represent another typical example of negatively charged groups which suppress the cell adhesion. For example, they can be used for developing anticoagulant blood-contacting surfaces [39].

Another important factor for cell-substrate interaction is the roughness and topography of the surface. Generally, nanostructured substrates are considered to be beneficial for cell adhesion and growth. The reason is that nanostructures mimic the nano structure of natural ECM, for example nanofibers, nanocrystals or nanosized folds of ECM molecules. On nanostructured surfaces, ECM molecules can be adsorbed in the appropriate geometrical orientation which allows cell adhesion receptors to access to specific sites in the ECM [27]. However, cells typically spread incompletely on rougher surfaces since they can adopt an irregular, elongated shape, whereas the cells homogeneously covered on well-flattened smoother surfaces [40].

### 2.2.2 Engineering the cell-substrate interface towards guided growth

Patterned neuronal cells and guided neurite growth are important for applications such as prostheses, biosensors, and tissue engineering. Recently, technological advances allow us to precisely engineer the geometry and chemistry of substrate surfaces which enables the control of the cell interaction with the substrate or even the guided cell growth. These methods allow the production of substrate features on a nano and micron level. Micropatterned surfaces allow a selective cell adhesion and guided growth, which can be used in tissue engineering, neuroelectronics and biosensors [27]. Nanopatterned surfaces

represent an effective method for controlling the spacing and distribution of ligands for cell adhesion receptors on surfaces [27]. Therefore, the cell proliferation, differentiation and other functions can also be manipulated. Some of the most commonly used surface engineering methods are microcontact printing, photolithography and electron beam lithography. In the following examples of different patterning methods are subdivided in two categories: starting with *additive* or *bottom-up methods* followed by *subtractive* or *top-down methods*.

*Additive* or *bottom-up methods* (Figure 2.3):

In additive or bottom-up methods target material or biomolecules are locally added onto the desired surface via either a stamp/probe contacting or a print head shooting drops. There are certain advantages of these methods. For instance, they are economic, productive, straightforward, local distributed and don't require a harsh environment (cleanroom). However, the disadvantages are also quite obvious. The resolution is not that high compared with the subjective methods (as shown later). An exception is obviously the scanning probe lithography (Figure 2.3c) which is very complex and definitely not suitable for mass production.

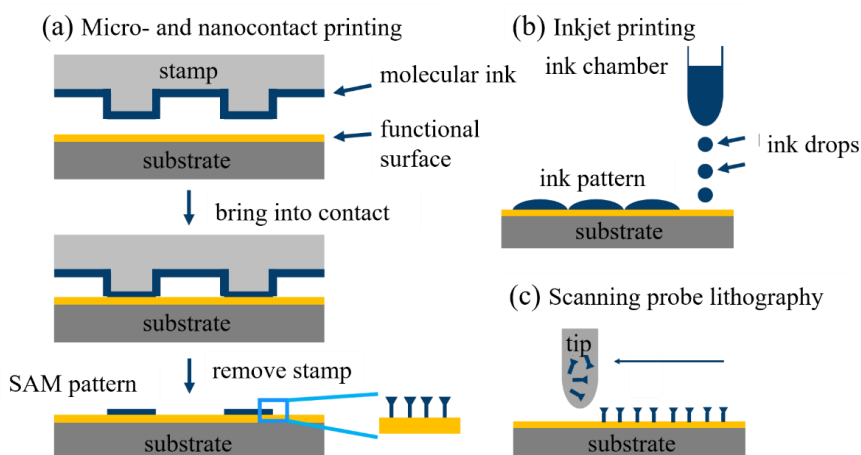


Figure 2.3: Examples of additive patterning techniques. (a) Micro- and nanocontact printing, SAM or proteins patterns are achieved by region-selective transfer of a molecular ink onto the substrate using an elastomeric stamp. (b) Inkjet printing, ink drops of SAMs or proteins are dropped on to a substrate via a print head. (c) Scanning probe lithography, by using nanoscopic probe tips which locally add molecules. Adapted from [41].

(i) *Micro- and nanocontact printing*

Nanocontact printing which represents an extension of microcontact printing, is a highly parallel, manufactural, and additive process that allows printing of 100 nm structures. It uses a stiffer elastomeric stamp and high molecular weight inks to limit the diffusion and guarantee the spatial resolution. Typically, microstructured elastomer PDMS stamps are used to transfer the intended molecules onto substrates (Figure 2.3a). The straightforward stamp-dependent method also has limitations and disadvantages. For instance, in the sub-micrometer regime, the PDMS stamps can lose their mechanical integrity and deform which leads to an inherently limited spatial resolution [42].

(ii) *Inkjet printing*

The adaptation of ‘standard office printers’ for the deposition of bioinks leads to another additive technique. In this technique even individual neurons can be printed. These deposition devices are typically composed of commercial printer parts, i.e. ink reservoir, print head, and a movable substrate table (Figure 2.3b). Piezoelectric or thermal inkjet printers can be used to release a certain fluid volume onto the substrate. For example, PLL has been printed as an adhesive material bioink on polyethylene glycol (PEG) substrates showing a strict pattern of neurons over 25 days without any detriment of the electrophysiological properties or the synaptic distribution [43].

(iii) *Scanning probe lithography*

Scanning probe lithography techniques have a lot of advantages compared with other conventionally used fabrication techniques. Not only that it can create nano-size patterns but also it can be performed under ambient condition. For example, dip-pen nanolithography (DPN) utilizes functionalized atomic force microscope (AFM) tips to directly transfer molecules in the defined pattern on the substrate (Figure 2.3c). Different patterns are directly produced by coating tips with the biomolecules of interest typically in a humid chamber, this technique provides extremely flexibility in the fabrication of nanostructures.

Up to now, DPN has been already used for creating protein nanoarrays on nickel oxide, silicon oxide, and gold surfaces [44-46]. However, this technique still has its drawbacks. For instance, the development of adequate inks, the stiffness of the tip and, last not least, this is a time-consuming process which doesn’t allow large area processing or mass production [47-49].

*Subtractive or top-down methods* (Figure 2.4):

In contrast to additive or bottom up methods, the subtractive or top-down methods represent another way of constructing patterns. In these methods, normally a photo resist has to be prepared on the substrate beforehand. Then, depending on the unique properties of the photo resist, after exposed either to UV light or electron beams, the photo resist will crack and can be removed during development (or, alternatively, the photo resist will be polymerized, and the rest will be removed). This way the designed structure can be achieved. Although these methods are more complicated, they will lead to a high resolution, and allow large area and mass production.

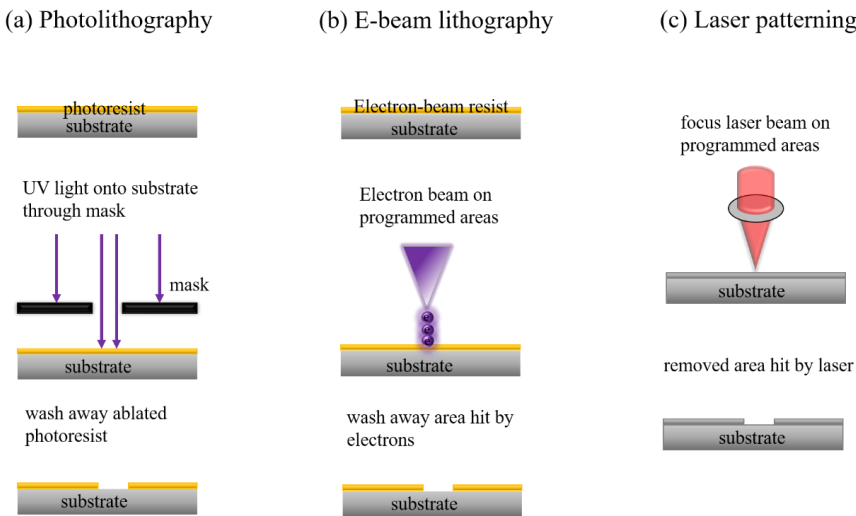


Figure 2.4: Example of subtractive patterning techniques showing photolithograph (a), e-beam lithography (b) and a direct method, laser ablation (c), where a focused laser beam generates the surface topography. Adapted from [50, 51].

(i) *Photolithography*

As shown in Figure 2.4a, photolithography starts by coating the substrate with a photoresist. Then, the resist is exposed to UV light through a mask with the desired pattern. At the exposed area the photoresist will be ‘cracked’, and in the final step is washed away using a developer solution.

Photolithography is a powerful technology for micropatterning. However, it requires the expensive clean room facilities and is limited to micrometer resolution. For most biological applications which only require micron level precision this is sufficient. Nevertheless, some experiments do require submicron resolution, which can be accomplished by e-beam

lithography.

*(ii) Electron beam lithography*

Electron-beam (e-beam) lithography (EBL) represents a maskless lithography method. It uses an electron gun similar to a scanning electron microscope. In contrast to photolithography, the resolution of EBL reaches a level down to a few nanometer. Similar to photolithography, the substrates are first coated with a resist which alters when exposed to the e-beam [52]. Similar to photolithography, EBL requires a cleanroom facility. However, it is very flexible (patterns are programmed) and provides sub-micron resolution.

*(iii) Laser patterning*

Surface patterns can also be achieved directly, for example by pulsed laser ablation. In this process a high-intensity laser pulse is focused on a spot on the substrate where the absorbed electromagnetic radiation excites electrons and is converted into heat. If the energy is large enough material is removed by melting and vaporization (Figure 2.4c). Laser patterning can be employed for a wide range of materials like polymers, semiconductors, ceramics, or metals. This technique allows a submicrometer which largely depends on parameters of the laser beam such as laser wavelength, beam profile, pulse duration, physical properties of the sample material, and environmental gas pressure.

The main advantage of the direct writing technique lies in its flexibility, which allows to obtain arbitrary patterns and even morphologies in a single step and without a mask. However the processing time depends on the resolution, sample size, and laser repetition rate and therefore is usually quite low. Unlike ion or electron beams, which represent alternative sources for the direct writing, laser surface patterning doesn't require a vacuum or cleanroom. Moreover, it isn't limited to planar substrates and relatively inexpensive [53].

### 2.3 Surface functionalization with organic SAMs

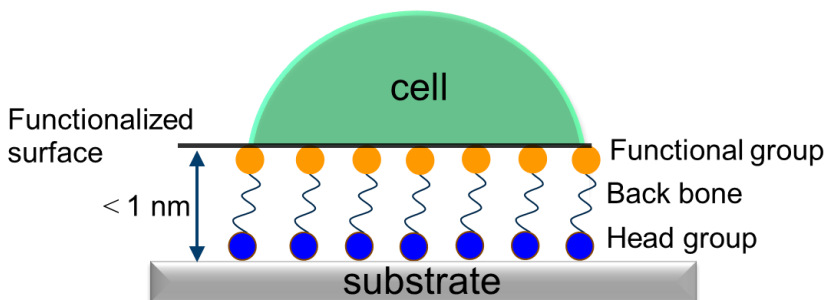


*Figure 2.5: Schematic of the functionalization of a substrate with a SAM consisting of organic molecules (blue circle indicates the chemisorbing head group and orange circle functional group) which can be chosen with a variety of chemical functionalities. The green half circle represents the biological object (e.g. a cell), the interface between substrate and cell is modified by the molecular monolayer. Adapted from lab collection.*

Self-assembled monolayers (SAM) are ordered molecular assemblies that form spontaneously with a specific affinity of their head groups to the substrate. Figure 2.5 shows a schematic, including the constituents of a SAM-molecule (head group, back bone, functional group). SAMs can be utilized in various technical applications, for example, protective coatings [54, 55], adhesion [56], building blocks in heterostructure and chemical anchors [57], surface chemistry, electronic properties [58], biointerface applications [59]. As shown in Figure 2.5, SAMs can behave as a link between organic cells and inorganic substrates, i.e. they are ideal for interfacing biological materials.

There are different types of organic SAMs with respect to their head group, such as thiols, silanes or phosphonates (Table 1). For sure the kinds of the different SAMs are far beyond the given examples in Table 1. It is also worth noting that each head group also has its preferable type of substrate, to which it binds.

Table 1: Examples of typical SAMs for different head groups and their corresponding substrates

SAMs	Head group	Preferred substrate	Possible application	reference
silanes	-SiCl <sub>3</sub>	SiO <sub>2</sub>	bio-interface modification; interlinker	[60-62]
	-Si(OCH <sub>3</sub> ) <sub>3</sub>			
	-Si(OC <sub>2</sub> H <sub>5</sub> ) <sub>3</sub>			
phosphates	-PO(OH) <sub>2</sub>	TiO <sub>2</sub>	electronics; FET	[63, 64]
		Al <sub>2</sub> O <sub>3</sub>		
		Ta <sub>2</sub> O <sub>5</sub>		
		Nb <sub>2</sub> O <sub>5</sub>		
thiols	-SH	Au	biosensors; electrodes modification	[58, 65]
		Pt		
		Ag		

In general, the self-assembling molecule consists of three parts: the head group, the back bone and the functional group. The head group is responsible for the anchoring of the molecule onto the substrate. Therefore, different head groups have their preferred substrates to which they bind. The alkyl (back bone) chain provides the stability of the molecular monolayer. Due to the van der Waals interactions between adjacent molecules, it also has a significant impact on the ordering of the SAM. Finally, the terminal end group provides the chemical functionality of the monolayer system and therefore it defines the overall property of surface. To a certain extent suitable molecules are commercially available or can be prepared by known chemical reactions.

### 2.3.1 Silane SAM on oxides

The typical process of SAM formation of silanes on SiO<sub>2</sub> consists of two steps (Figure 2.6):

- (i) Activation of the SiO<sub>2</sub> surface which leads to a reconstruction of the silanol bonds at the surface,
- (ii) Binding of silanes with their headgroups to the open silane groups.

Freshly prepared SiO<sub>2</sub> possesses silanol groups on the surface. If the surface is exposed a humid environment, Si-OH undergoes a condensation reaction, forming the more stable siloxane group Si-O-Si. In this state, the Si surface possesses fewer open bonds and, as a result, the quality of a silanization would be poor. The activation, for instance, with an oxygen plasma leads to a recovery of the silanol groups and allows a dense coverage of the surface with silane molecules.

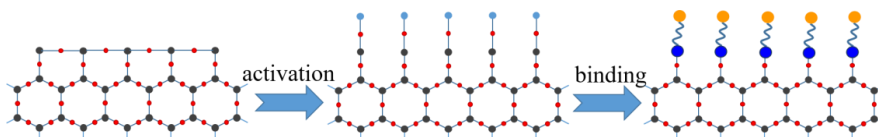


Figure 2.6: Schematic of the structure of  $\text{SiO}_2$ , activation and binding of silanes.

*Role of water:* It is known that the presence of water at the interface has a large impact on the reaction of the open silanol group therefore the water content is carefully controlled during the silanization. As shown in Figure 2.7, only without water or little water, there is a chance of forming a perfect monolayer, whereas excess water facilitates polymerization and the formation of thick polymer films. One way to avoid the problem of moisture is the use of a gas-phase deposition technology which allows a precise control of the deposition condition. This is one of the reasons, why we developed a gas-phase based deposition technique for the deposition of silane SAMs.

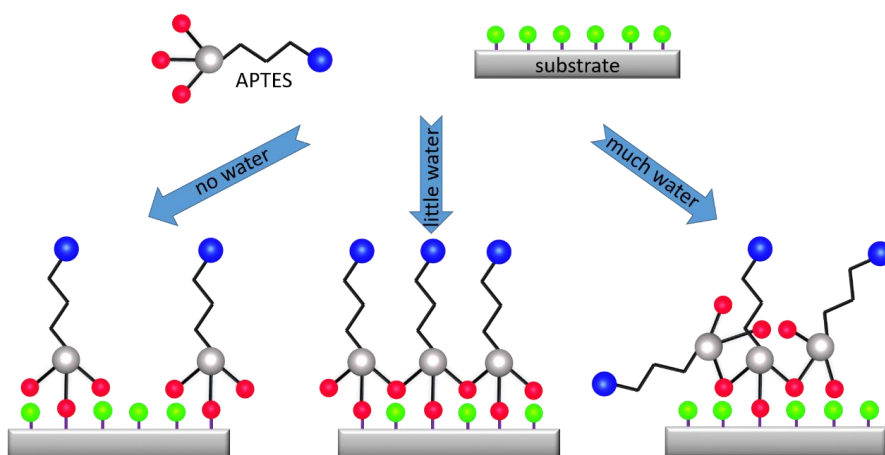


Figure 2.7: Schematic representation of the structure of silane layers for different water content. Adapted from [66].

#### *Liquid phase deposition (LPD):*

The simplicity and the low costs are important reasons for the use of LPD for the deposition of organic molecules. In principle, the cleaned (and maybe activated) sample has to be submerged into a molecule solution for a certain time, and a molecular layer automatically assembles (Figure 2.8a). For silane-based systems, for example, the water content is extremely important for the proper preparation of the SAM. Additionally a proper outgassing of the solution is important and after completion of the SAM, an appropriate

rinsing procedure has to be applied. Therefore, although the process is simple, the resulting film quality and properties are often not reproducible.

*Vapor phase deposition (VPD):*

The principle of VPD can also be very simple. For this method substrate and molecular source are placed in a chamber. By evacuating the chamber, molecules are evaporated onto the substrate (Figure 2.8b). The molecular source can be heated moderately to increase the vapor pressure of the molecules. While employing a vacuum chamber generally is more expensive, the advantages of VPD over LPD are in the protection of the environment, the better control of the process, and last but not the least, the avoidance of moisture. These are the reasons why we choose VPD in this work.

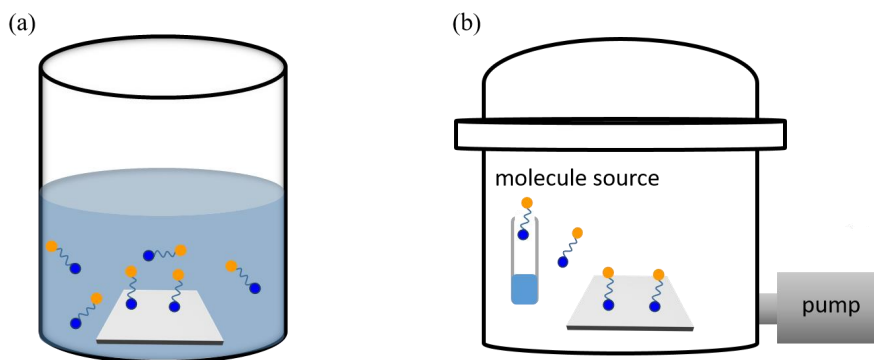


Figure 2.8: Schematic of LPD and VPD routes of the deposition of molecular SAMs.

*Silanes on other oxides:* As discussed above, the adhesion of silanes on  $\text{SiO}_2$  involves condensation reactions between the hydroxyl groups of the  $\text{SiO}_2$  substrate and the silane. Therefore the concentration of the Si-OH groups on the surface is an important parameter to optimize the SAM's quality. A classification of adhesiveness of organosilanes on various inorganic substrates is given in Figure 2.9. Aluminum ( $\text{Al}_2\text{O}_3$ ) has a better adhesion compared with other inorganic oxides [67, 68], but all of them show a worse adhesion behavior compared with  $\text{SiO}_2$ . This difference in adhesiveness results mainly from the different structures of the oxides and the resulting concentration of hydroxyl bonds.

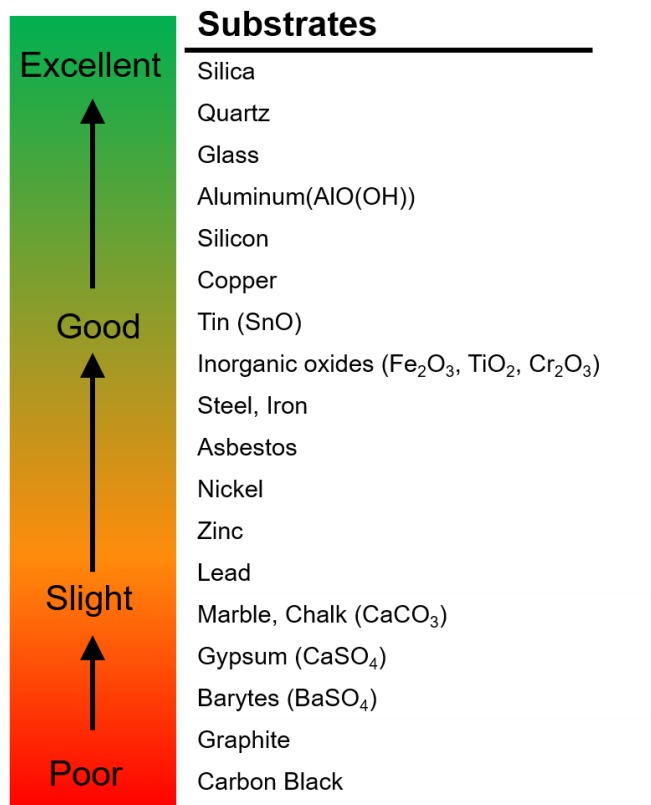


Figure 2.9: Binding effectiveness of silanes on different inorganic oxides, taken from [68].

### 2.3.2 The role of the functional group

As indicated in Figure 2.5, the interface between the object (here a cell) and substrate has been functionalized by a SAM. The new interface is determined by the property of the functional group of the SAM. Since we are working with silanes, their head groups have similar chemical properties, which allow to bind to  $\text{SiO}_2$  surface. However, silanes can differ in the length of the backbone and the choice of the functional group. Table 2 lists similar silanes with commonly used functional groups.

Table 2: Examples of silanes with different functional groups and their applications.

Functional group	examples	application	property	references
trifluoromethyl/trimethyl-(CF <sub>3</sub> )/(CH <sub>3</sub> )	propyltriethoxysilane(CH <sub>3</sub> (CH <sub>2</sub> ) <sub>2</sub> Si(OC <sub>2</sub> H <sub>5</sub> ) <sub>3</sub> );  trichloro(3,3,3-trifluoropropyl)silane (C <sub>3</sub> H <sub>4</sub> Cl <sub>3</sub> F <sub>3</sub> Si)	stamp fabrication; hydrophobic modification; friction control in micro machines	hydrophobic	[69, 70]
amino-NH <sub>2</sub>	3-aminopropyltriethoxysilane (APTES)  N-(2-aminoethyl)-3-aminopropyltrimethoxysilane (EDA)  (3-trimethoxysilylpropyl) diethylenetriamine (DETA).	immobilization of biomolecules; cells adhesion	protonated at pH7.4	[71-74]
thiol-SH	(3-mercaptopropyl)trimethoxysilane (MPTS)	metal nanoparticles	bond to metal	[75]
epoxy-C <sub>2</sub> H <sub>3</sub> O	(3-Glycidyloxypropyl)trimethoxysilane (GLYMO)	immobilization of biomolecules; bio incompatible interface	very reactive	[76]

As shown in Table 2, there are different functional groups which can be chosen to modify the substrate's surface and achieve the desired properties. For example, -CF<sub>3</sub>/CH<sub>3</sub> is often used in stamps fabrication due to its excellent hydrophobic properties. -SH groups can be used to link gold nanoparticles. Epoxy groups are very reactive and can be used to immobilize biomolecules.

In our case we wanted a SAM that is suitable for guided cell growth. It is known that proteins on the cell membrane have negative charges. Therefore, in order to make the surface attractive for cells, the surface should be positively charged. The amino group (-NH<sub>2</sub>) can fulfill this task, since it becomes positively charged in an electrolyte. Therefore, it might be a good candidate for the functionalization of a "bio-unfriendly" surface and turns it into a biocompatible surface.

## 2.4 Electronic cell-chip coupling

A central goal of neuroelectronics is the understanding of the functional connectivity of neuronal circuits, for example, to learn more about their physiological functions. Nowadays, the available methods for the recording of neural activity include [77]:

- (i) Intracellular recording and stimulation using either sharp or patch electrodes,
- (ii) Extracellular recording and stimulation using substrate-integrated microelectrodes or microelectrode arrays (MEAs),
- (iii) Magnetic resonance imaging (MRI), electroencephalography (EEG) and magnetoencephalography (MEG), which allows to record activities of large-scale neural populations and therefore isn't suitable for single-neuron resolution.

The advantage of intracellular recording systems is that they exhibit very large signals and provide accurate readouts of the entire dynamic voltages range of the cells during the measurement. However, the use of sharp or patch microelectrodes is first of all limited to individual neurons and, second, it is not suitable for a long-term and multiple network measurement. Furthermore, the neurons will die during or shortly after the measurement.

In contrast, the non-invasive extracellular MEAs enable the simultaneous recording and stimulation of a larger population of cells, and for a period of days and months without or little damage to the neuron's membrane [78, 79]. However, in order to achieve a good signal-to-noise ratio of recording as well as allowing stimulation of cells, it is of vital importance to achieve a good cell-chip coupling. If we neglect the relatively high conductance of the electrolyte, the cell-chip coupling is determined by two factors (Figure 2.10):

- (i) interfaces, namely the cell-electrolyte interface and the electrode-electrolyte interface, and
- (ii) the sealing resistance  $R_{\text{seal}}$ , defined by the cleft.

These interfaces' impedance can be represented by the parallel arrangement of a resistor and a capacitor (Figure 2.10). Whereas the cell-electrolyte interface is determined by the cells and medium, we can only affect the second interface, i.e. the electrode-electrolyte interface, by modifying the surface of the electrode.

The leakage current is mainly defined by the size of the cleft. The smaller the cleft, the larger is the leakage resistance  $R_s$  and the smaller is the loss of signal transfer. Since the cleft size strongly depends of the cell adhesion, this aspect is in principle already discussed in the previous sections.

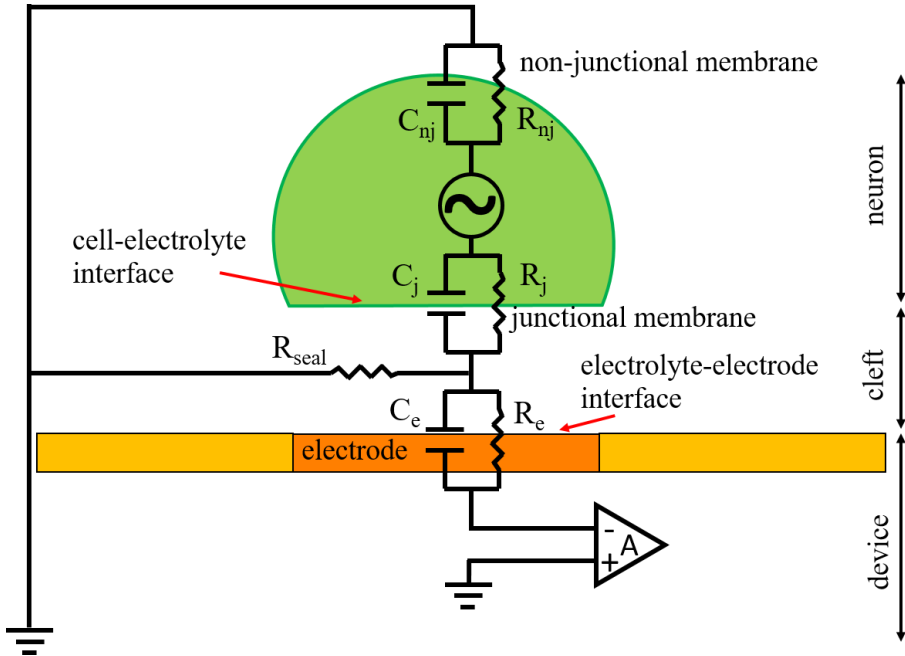


Figure 2.10: Schematic of a neuron on a substrate-integrated planar electrode as well as the corresponding analogue electrical circuit. The neuroelectronic hybrid consists of a neuron, a cleft between neuron and substrate, and an electrode.

The structural relationship between a neuron and a substrate-integrated planar electrode and the corresponding electrical circuit is shown in Figure 2.10. The neuroelectronic interface is composed of three components, a neuron, a cleft between the neuron and the substrate surface, and an electrode. For the simplified model shown in Figure 2.10, the neuron surface can be further divided into a junctional membrane which faces the sensing pads (with  $R_j$  and  $C_j$  as the junctional resistance and junctional capacitance, respectively), and the non-junctional membrane (with  $R_{nj}$  and  $C_{nj}$ ) which faces the culture medium. The cleft, between neuron and electrode causes an electrode-electrolyte impedance (with  $R_e$  and  $C_e$ ) and a resistance, called seal resistance ( $R_{seal}$ ) [80].

#### 2.4.1 Action potential and cell-electrolyte interface

The action potential (AP) represents an electronic pulse during which the cell's membrane potential quickly raises and falls. Such APs can propagate through cellular layers and are responsible for a large variety of organism functions like sensing, thinking, moving and heart beating.

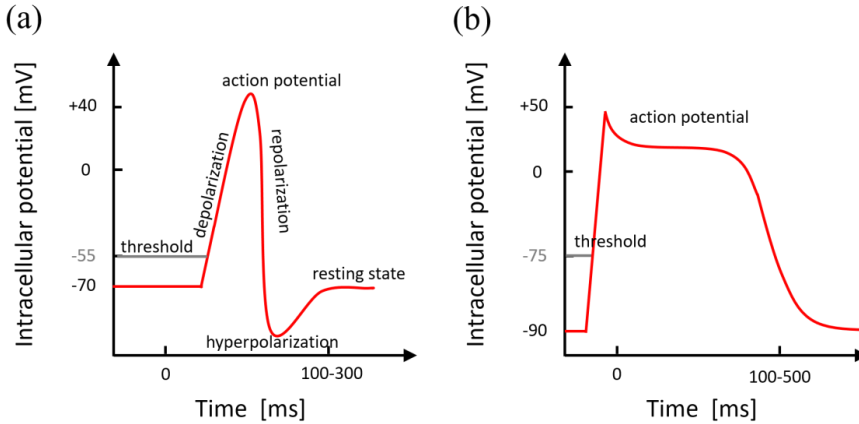


Figure 2.11: schematic of action potentials of a neuronal cell (a) and a cardiac muscle cell (b). The action potential duration of a neuronal cell is short ( $<5$  ms), compared with the duration of HL-1 cell lasts tens of ms with a long repolarization period of up to 200ms. Adapted from [81-84].

Typical neuronal and cardiac APs are shown in Figure 2.11. In equilibrium, the cells are at resting potential, which is usually around  $-70$  mV for neuronal cells and  $-90$  mV for cardiac muscle cells. An electronic stimulation can temporarily depolarize the membrane. If the stimulation is not strong to reach the threshold of  $-50 \pm 5$  mV or  $-75$  mV for neuronal cells and cardiac muscle cells respectively, the action potential will not be fired. Otherwise if depolarization potential reaches the threshold value, the protein channels in the membrane which control the sodium will open and sodium ions ( $\text{Na}^+$ ) flow into the cell due to the chemical gradient. The concentration of  $\text{Na}^+$  is enhanced in neuronal and cardiac cells which will increase the membrane potential to  $+40 \pm 10$  mV. While the accumulation of  $\text{Na}^+$  in the cell, there are too much positive ions, therefore the potassium ions ( $\text{K}^+$ ) channel will open and  $\text{K}^+$  leaves the cell. The efflux of  $\text{K}^+$  is the reason that results in a membrane hyperpolarization, the membrane potential can reach even values lower than the resting potential. The principle of a cardiac muscle AP is very similar (Figure 2.11b), the first repolarization step is caused by the potassium efflux that is the same with neuronal cells (Figure 2.11a), however, there is a characteristic plateau caused by the impact of slow  $\text{Ca}^{2+}$  channels, keeping the membrane potential at a high potential for around 200 ms. The final repolarization is due to the ongoing efflux of  $\text{K}^+$  ions [81-84].

The cell-electrolyte interface is in principle defined by the membrane of the cell which is made of bilayer phospholipid molecules. The membrane has an approximate thickness of 5 nm, and in general it represents a perfect insulator. However, in the case of electro active cells such as neurons or cardiac muscle, the membrane incorporates ion selective channels

and pumps, allowing ions to flow in and out of the cell's cytosol. There is a variety of factors which can affect the ion channel's conductivity, and therefore can cause the changes in the ionic concentration, and consequently lead to depolarization and repolarization of the membrane [81].

#### 2.4.2 Electrode-electrolyte interface

As discussed above, the cell-electrolyte interface heavily depends on the medium that the cells are placed in. Therefore there is little we can do to modify this interface and its properties. However, the electrode-electrolyte interface can be manipulated, for instance, to achieve a high signal recording. One can:

- (i) introduce a better mechanical coupling (see sections above) and, thus, a smaller cleft, which in the end leads to smaller signal losses, or
- (ii) modify the electrode-electrolyte interface by modification of the interface and, thus, reduce the electrode-electrolyte impedance.

Our option is the functionalization of the surface with organic molecules, which could affect not only the cleft size but also the impedance of the interface.

##### *Sealing resistance:*

It is obvious that the amplitude and shape of the recorded AP signal depend on  $R_{\text{seal}}$ . Studies of the cell-electrode interface show typical cleft size between 40-100nm [7, 85-87]. For most cell types this corresponds to an  $R_{\text{seal}}$  value of the order of 1-2M $\Omega$  and APs recordings of 10-100 mV [80].

##### *Electrode-electrolyte impedance:*

Another component which affects the electronic coupling of cells and electrodes is the input impedance  $Z_c$  of the electrode. The type of charge transfer of a living cell and an electronic device are fundamentally different, i.e. the former is formed by ion transport and motion in a solution whereas the latter is given by electron motion in metals [88, 89]. Due to this difference the electronic coupling is represented by an impedance. Typically the impedance of the sensing electrode is attributed to the 'blocking' ion bilayer, Helmholtz layer (Figure 2.12) which forms on any surface in an ionic solution. Reducing the surface area of an individual electrode to match the dimensions of individual neurons allows a local measurement of neuronal signal and, in case of the use of MEAs, an increase of the spatial resolution [90-92]. However, this automatically reduces the amplitudes of the recorded signal and consequently reduces the signal-to-noise ratio. Therefore, the electrode's

geometry and the resulting impedance lead to constraints on the electrode size. Typical approaches to increase the surface area are nanostructures, for instance spongy platinum black or  $\text{Ti}_3\text{N}_4$  [93], gold nanoflakes and nanopillars [94, 95], or carbon nanotubes [96]. According to our group's research, using organic molecules to functionalize the metal surface could also affect not only the cleft size but also the impedance of the interface. This will not be discussed in this work.

*Helmholtz or electrical double layer:* If a solid (insulator, semiconductor, metal) particularly an electrode, is placed into an electrolyte, an electronic interface develops in form of an electrical double layer (EDL). The EDL is an ionic arrangement at and near the surface (Figure 2.12). Its first layer is typically a layer of water molecules, especially adsorbed on the surface, while the second layer is composed of the oppositely charged hydrated ions, attracted by the Coulomb force. These ions partially screen the charge of the object. The second layer cannot be considered static, but rather diffusive.

Helmholtz firstly proposed the double layer theory that the EDL can be described as a parallel-plate capacitor [97]:

$$C = \epsilon_0 \epsilon_r \frac{A}{d} \quad (1)$$

where  $\epsilon_0$  represents the dielectric constant of vacuum,  $\epsilon_r$  indicates the relative dielectric permittivity of the solvent,  $A$  is the area of the electrode and  $d$  is the distance between the electrodes.

L.G. Gouy and D.L. Chapman observed that the EDL capacitance is not constant but frequency dependent. Therefore, they developed the Helmholtz model further by considering the thermal movement of the ions and proposed a diffuse layer of ions at the charged surface. According to this model local, the ion concentration depends on the potential  $\Phi$  at a distance  $d$  from a surface with a potential  $\Phi_0$  [98-99]:

$$\Phi = \Phi_0 \times \exp\left(\frac{-d}{\lambda_D}\right) \quad (2)$$

with the Debye length  $\lambda_D$  given by [100]

$$\lambda_D = \sqrt{\frac{\epsilon_0 \epsilon_r k_B T}{2n_0 z^2 e_0^2}} \quad (3)$$

where  $n_0$  is the bulk concentration of ions in the electrolyte,  $e_0$  is the elementary charge,  $z$  is the ion charge,  $k_B$  is the Boltzmann constant, and  $T$  is the temperature.

The excess charge at the solution side is electrostatically attracted to the electrode interface, but this attraction is counteracted by the random thermal motion which aims to equalize the concentration in the solution. The overall equilibrium can be computed via the linear

Poisson-Boltzmann equation [101]:

$$\frac{d^2\phi}{dx^2} = \frac{\phi(x)}{\lambda_D^2} \quad (4)$$

Solving the simplified Poisson-Boltzmann equation results in the Gouy-Chapman capacity [81]:

$$C_{GC} = \frac{\varepsilon_0\varepsilon_r}{\lambda_D} \cosh\left(\frac{ze_0\phi(0)}{2k_B T}\right) \quad (5)$$

The Gouy-Chapman model considers all ions as point charges, which can approach the surface infinitely close. This assumption leads to a major drawback of an unlimited increase of capacitance at high ionic concentrations. This has never been verified experimentally, therefore the model was further improved by Stern in 1924.

Stern stated [102] that ions cannot approach the electrode's surface closer than their ionic radius. The distance of the closest possible approach is called Outer Helmholtz Plane (OHP). The ion distribution of the OHP can be considered as a cloud of ions with a higher concentration at the electrode which decays away from the electrode surface. The ion cloud is called the Gouy-Chapman diffuse charge layer (GCL). Some ions even penetrate the hydration sheath and adhere to the electrode. The plane in front of the electrode surface is defined by a layer of absorbed water molecule, the Inner Helmholtz Plane (IHP) (Figure 2.12a).

The properties of the space-charge distribution is shown in Figure 2.12a and can be summarized by an equivalent electric circuit (Figure 2.12b) consisting of an electrolyte resistor  $R_{el}$  in series with the parallel connected of a charge transfer resistor  $R_{ct}$  and EDL capacitor  $C_{DL}$ .

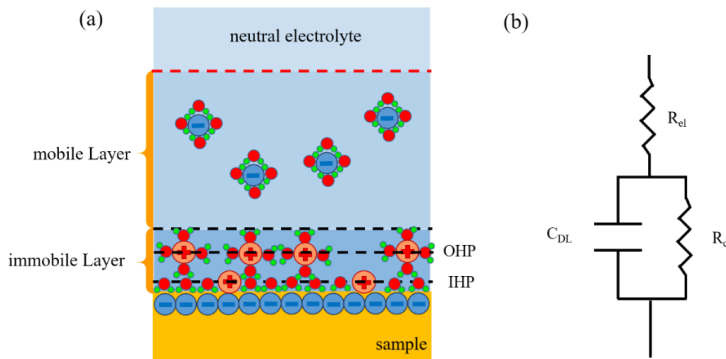


Figure 2.12: Electrode-electrolyte interface and equivalent electrical circuits. (a) Schematic representation of an electrode-electrolyte interface, (b) electrical circuit of the electrode-electrolyte interface.

The discussions above are based on bare electrode-electrolyte interfaces. In our work, we used SAMs of organic molecules to functionalize the surface of our substrate. It can be expected that this functionalization not only affects the mechanical cell-substrate interaction with all its consequences on the sealing resistance and the growth behavior, it can also directly affect the EDL and thus the electrode-electrolyte impedance. We therefore expect that the SAM might have an impact on the mechanical and electronic cell-chip coupling.

### 3. Sample preparation, characterization and experimental techniques

In this work, we applied a series of experimental techniques ranging from deposition, lithography, characterization, cell culture to electronic measurements. The techniques listed and sketched in this chapter are:

- (i) Various deposition techniques, which include molecule layer deposition (MLD), atomic layer deposition (ALD) and metal evaporation.
- (ii) Electron beam lithography including pattern design, lithography, etching and lift-off technique.
- (iii) Characterization methods such as ellipsometry, contact angle measurement, and streaming potential measurements.
- (iv) Cell culture experiments including cortical rat neurons and HL-1 cell cultures, as well as staining experiments and critical point drying.
- (v) Electronic characterization methods to analyze different types of MEAs and cell chip communication.

#### 3.1 Deposition techniques

There exists a larger number of techniques for the deposition of thin films. In this work only gas phase based technologies (VPD) are used. The deposition of organic layers is done by molecule layer deposition (MLD) and the different oxides thin films are deposited via atomic layer deposition (ALD). Furthermore, electron beam evaporation is used for the production of metal layers (i.e. electrodes).

##### 3.1.1 Molecule layer deposition

Figure 3.1 shows the image and a schematic of the MLD device used in this study. It allowed us to perform all important deposition steps including surface activation via ozone, subsequent molecular deposition from the gas phase, and post-deposition treatment without breaking the vacuum. The different components of the MLD setup (Figure 3.1) are:

- Deposition chamber, where the samples and sensors (e.g. capacitive sensor or surface acoustic wave (SAW) sensor) are placed for the activation and deposition process.
- Ozone generator, which converts  $O_2$  to  $O_3$  (ozone) for cleaning and activation of the surface.
- Molecule source, which contains the molecules, and valves for the deposition.

- Pumps and gas sources ( $O_2$ , Ar,  $N_2$ ) to keep the constant pressure of a given gas (alternatively vacuum) during deposition and post-deposition treatment.

The different process steps necessary for the deposition of molecule layers are explained in the following.

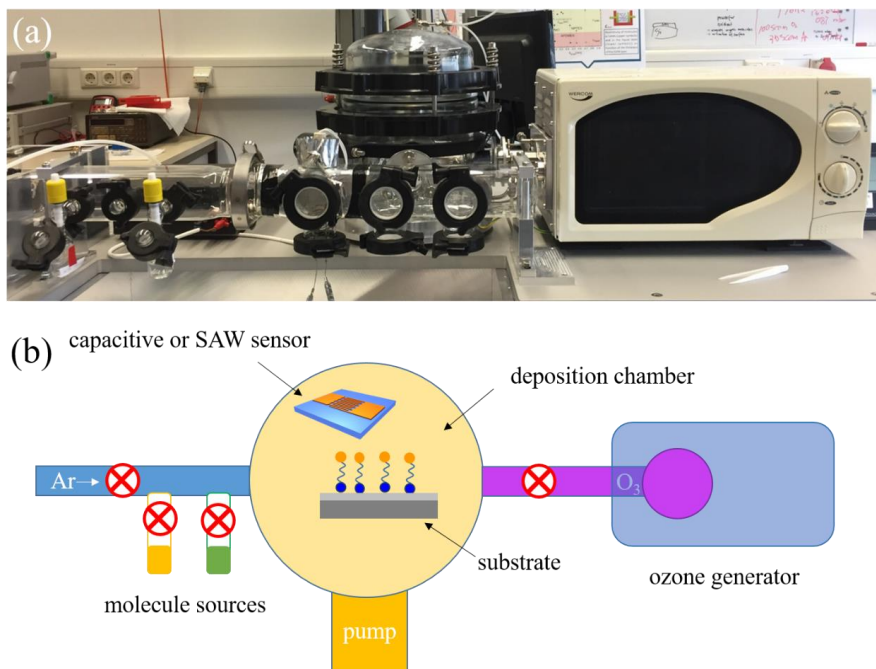


Figure 3.1: (a) Image and schematic (lab collection) of the MLD setup, which shows (from left to right) the Ar gas supply (blue) for the working gas used during the deposition, the molecule source (yellow and green), the main chamber (yellow) including the in situ capacitive or SAW sensor – where activation and deposition takes place – and the microwave oven (blue) producing ozone (purple) for cleaning and activation of the samples and sensor. All essential ingredients are separated via valves (red) from the recipient, which is pumped with a turbo pump and an oil-free forepump.

*Activation and cleaning:* First, the substrates were placed in the MLD chamber, which was then evacuated to  $\sim 10^{-5}$  hPa and flooded with oxygen (99.99% purity and a flow rate of 93 sccm), setting a pressure of 1 hPa via downstream control. Oxygen is activated and converted to ozone via a microwave discharge (2.45 GHz, 700 W), which then flows with the oxygen stream to the substrate. At the substrate, the ozone, first of all, removes organic residues from the surfaces of the substrate and recipient (cleaning) and second, can activate the surface. For example in case of Si/SiO<sub>2</sub> substrate, the SiO<sub>2</sub> surface forms open silanol

surface bonds (Si-OH) upon exposure to ozone, which are later used for the bonding of silanes (Figure 3.2).

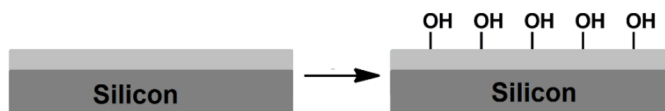


Figure 3.2: Sketch of ozone activation leading to the formation of hydroxyl groups on a  $\text{SiO}_2$  surface [104].

*Deposition process:* After surface cleaning and activation, the oxygen supply was turned off and the process gas (Ar) switched on. We used an Ar flow of 27 sccm and established a process pressure of 0.1 hPa. The actual deposition of APTES was initiated by opening the valve of the molecular source. After 10 minutes of deposition, the valve was closed and the actual deposition terminated, see Figure 3.3.

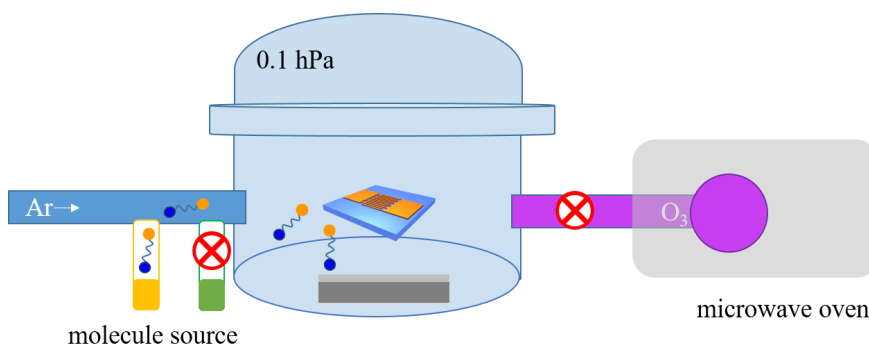


Figure 3.3: Schematic of the deposition process. During the deposition process, an Ar flow is established at a typical process pressure of 0.1 hPa. The actual deposition of APTES is initiated by opening the source for the given deposition time of typically 10 min.

*Post-deposition treatment (PDT):* In this work, we noticed that a PDT is of vital importance to achieve an integrated self-assembled monolayer via vapor phase deposition. After the actual deposition, the samples could be removed directly (no PDT, i.e.  $t_{\text{PDT}} = 0$ ), or they can be kept in the MLD device for a PDT. During the PDT the Ar supply was switched off leaving the sample at a background pressure of  $\sim 10^{-5}$  hPa for a given time. The duration  $t_{\text{PDT}}$  of this treatment was varied from 0 to 5 days. Although a higher temperature during PDT might accelerate SAM formation, the chosen conditions allowed us to observe the formation process in detail, as demonstrated in chapter 4.1.

*Capacitive sensor:* Different in situ sensors have been developed for the analysis and control of the MLD process. We used a capacitive sensor with has been developed in a previous study [105]. This capacitive sensor is based on planar interdigitated electrodes (IDE) (Figure 3.4) that allow the recording of the dielectric permittivity of the molecular layer throughout the entire deposition process. The IDEs of the capacitor consists of a combination of a Ti (5 nm) and a Pt (10 nm) layer and form a capacitor (gap size  $s = 1 \mu\text{m}$  and effective length  $l = 10.8 \text{ mm}$ ) (lab protocol).

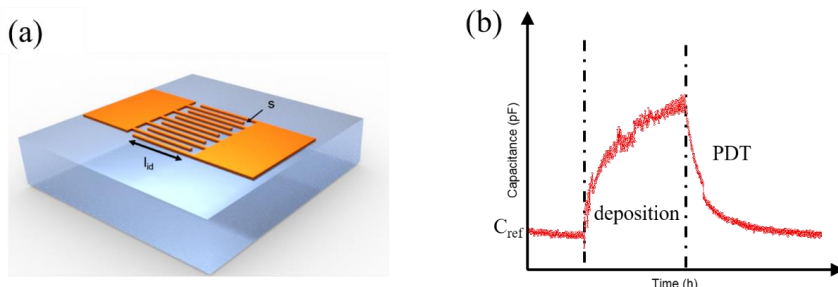


Figure 3.4: (a) Schematic of the interdigitated structure of the capacitive sensor, and example of the change of the (b) capacitive signal during the deposition of a molecular layer. Figure adapted from [105].

Since the total sensor capacitance  $C_{total}$  is given by the sum of the different contributions:

$$C_{total} = C_{gas} + C_{sub} + C_{mol} = C_{ref} + C_{mol} \quad (6)$$

arising from the reference (gas, substrate), and molecular layer. The change of the capacitance during deposition indicates the contribution from the molecular layer:

$$C_{mol} = C_{total} - C_{ref} \quad (7)$$

An example of the resulting change of the signal during deposition and PDT is shown in Figure 3.4b.

### 3.1.2 Atomic layer deposition

In ALD processes, precursors (i.e. organic molecules) containing the atoms to be deposited are individually introduced into the deposition chamber in a sequence and react with the surface or molecule on the surface. After a complete cycle, the remaining molecules that are not reacting with the surface will be pumped out. This leads to a film deposition in a layer-by-layer method. ALD offers a great potential for the production of thin, pinhole-free films with a high control of the thickness and composition of the films at the atomic level.

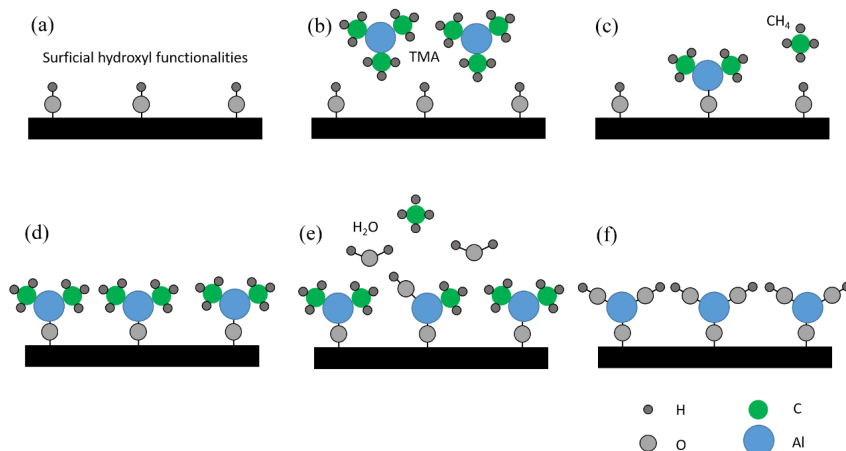


Figure 3.5: Schematic representation of a typical ALD process using the example of aluminum oxide layer. (a) The start layer has surficial hydroxyl functionalities; (b) TMA is introduced in the reaction chamber as the first precursor; (c) reaction occurs between the surficial hydroxyl functionalities and the TMA, methane is the produced as the by-product; (d) after the saturation of the surface, the TMA and methane are purged out from the chamber; (e) water is introduced as the second precursor and reacts with the surface; (f) another purge step removes all the residue water and methane. Now one layer is formed after one cycle. Adapted from [106,107].

Figure 3.5 shows the typical sequence of an ALD cycle on the formation of aluminum oxide ( $\text{Al}_2\text{O}_3$ ). Figure 3.5a presents the surficial hydroxyl functionalities on the substrate. The precursor trimethylaluminium (TMA,  $\text{Al}(\text{CH}_3)_3$ ) is evaporated into the reaction chamber (Figure 3.5b) where it reacts with the hydroxyl groups. This chemical reaction produces methane ( $\text{CH}_4$ ) as a by-product (Figure 3.5c). After saturation of the surface, the remaining TMA and methane are removed from the chamber by purging (Figure 3.5d). The second precursor ( $\text{H}_2\text{O}$ ) is introduced into the chamber and reacts with the surface (Figure 3.5e). The by-product methane and the remaining water are removed by a last purging step (Figure 3.5f). At this point an atomic layer of  $\text{Al}_2\text{O}_3$  is formed. Subsequently, further cycles can be performed to deposit additional atomic layers until a desired layer thickness is reached. The saturation of the individual precursor reactions makes ALD a self-limiting process that provides extremely high control of the deposited film thickness [106,107].

In this work, titanium oxide ( $\text{TiO}_2$ ), aluminum oxide ( $\text{Al}_2\text{O}_3$ ), and tantalum pentoxide ( $\text{Ta}_2\text{O}_5$ ) films with a typical thickness of 30 nm were deposited on  $\text{SiO}_2/\text{Si}$  substrates by atomic layer deposition (ALD) (FlexAL, Oxford Plasma Technology). The precursors (Sigma-Aldrich; St. Louis) and substrate temperatures for the different oxides were

tetrakis(dimethylamino)- titanium and 200 °C for TiO<sub>2</sub>, trimethylaluminum and 130 °C for Al<sub>2</sub>O<sub>3</sub>, and tris(diethylamido)(tert-butyylimido)tantalum(V) and 300 °C for Ta<sub>2</sub>O<sub>5</sub>. For the deposition, standard recipes of Oxford Instruments Plasma Technology were used.

### 3.1.3 Electron beam evaporation

For the deposition of metals (Cr, Pt) again a vapor deposition technique has been used, i.e. e-beam evaporation. During evaporation the material is heated to the boiling temperature, evaporate and condensed on the substrate facing the evaporation source (Figure 3.6). One type of vapor deposition is the e-beam evaporation or electron beam physical vapor deposition (EBPVD), which is shown schematically in Figure 3.6. The material is heated by an electron beam leading to a local evaporation of the material in the water-cooled crucible. The electrons are emitted from a heating cathode and subsequently accelerated by an anode. The electron beam is aligned by a magnetic field which is perpendicular to the beam. Where the beam hits the material in the crucible, the material evaporates and is transferred towards the substrate opposed the crucible. At the substrate the resulting film forms.

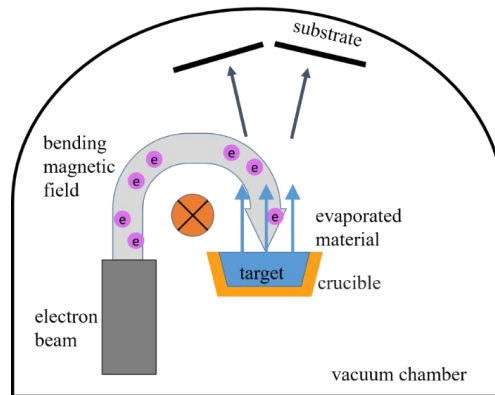


*Figure 3.6: Schematic of electron beam evaporation. An electron beam is directed onto the target via a magnetic field, which is oriented perpendicular to the beam and thus forces the electrons on a circular path. The electron beam heats the material resulting in an evaporation and thus the condensation on the substrates. Figure adapted from [106,108].*

In this work, electron beam evaporation is used to:

- (i) deposit thin chrome layers, usually 10nm thick, for e-beam lithography on non-conducting substrates, and
- (ii) deposit of Ti and Pt for the lift-off prepared electrodes.

## 3.2 Lithography and lift-off technique

Lithography represents one of the most important patterning techniques for micro and nano technology. There exist three different lithographic methods in our institute, optical, electron beam and laser lithography (see also chapter 2.2.2). Due to its high flexibility and resolution we chose e-beam lithography for this work. The complete patterning process can be divided into four process sections: design, lithography, lift-off, and etching.

### 3.2.1 Design

Electron beam lithography is also known as mask less lithography, since no mask is required to generate a wanted pattern. Instead, the pattern is created directly from a digital file which controls the electron beam as it scans across a resist-coated substrate. In this thesis, the program AutoCAD is used for all designs including the capacitive sensor, test structures for cell experiments (e.g. cell density test or guided cell growth), and the different MEA structures (Figure 3.7).

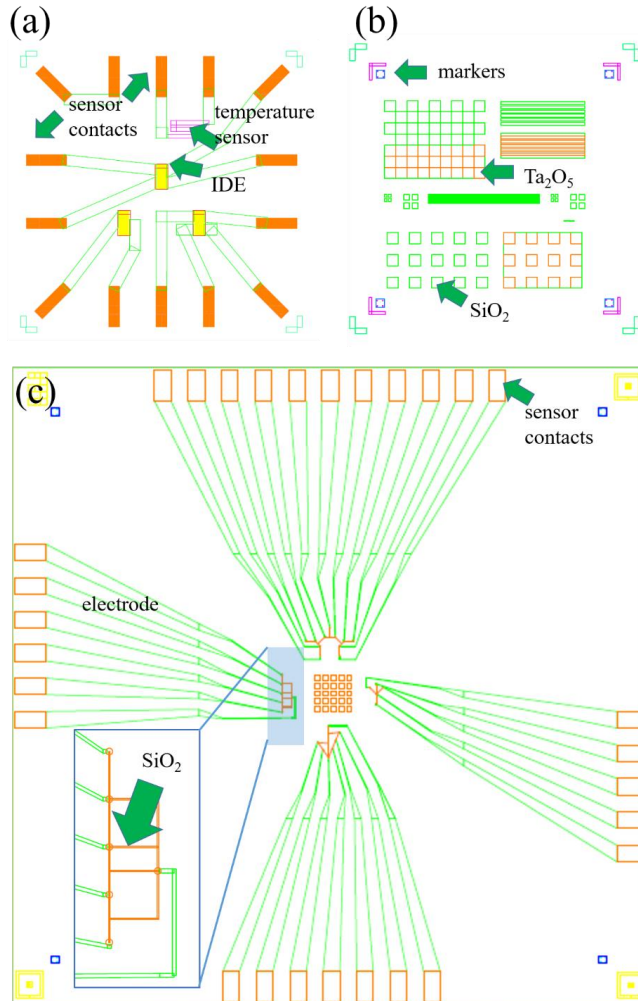


Figure 3.7: Typical structures designed via AutoCAD, (a) a capacitive sensor, (b) a test structure for analyzing the guided growth structure of cells, and (c) MEA patterns including the test structures for guiding the cells growth. Different processing steps are marked with the corresponding layer colors, for instance, in (c) the green line represents the metal electrodes formation, whereas the orange layer presents the etching step for opening both the electrode contacts on the edge and the test structures for guided growth in the center.

### 3.2.2 Lithography and lift-off

The actual patterning process includes a number of steps which are sketched and described in the following (lab protocol):

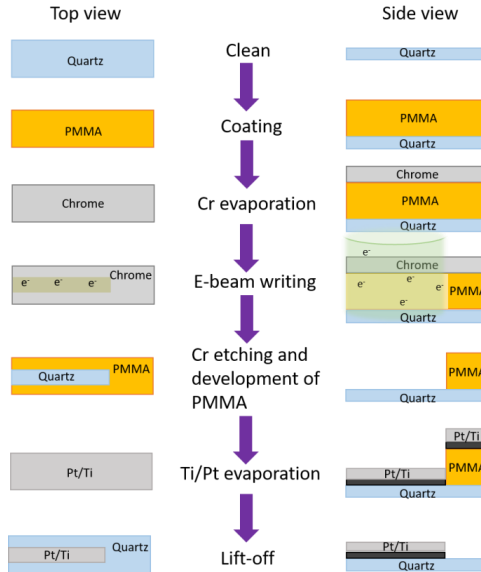


Figure 3.8: A schematic sketch of the different steps of the photolithography [101]. Note that the objects (e.g. substrate) are not up to scale.

**Cleaning:** The glass substrates are merged in acetone for 5 min in an ultrasonic bath at the highest power and repeated with propanol.

**Coating:** Photoresist poly (methyl-methacrylate) (PMMA AR-P 669.07) is spin-coated on the substrate using 4000 rpm for 60 s. The substrate is first completely covered with photoresist, the subsequent spin-coating yields a PMMA layer with a thickness of approximately 700 nm. After spin-coating, the sample should immediately transferred to a 120 °C hot plate and remain there for 15 min.

**Cr evaporation:** In order to enhance the conductivity of the PMMA, a 10 nm thick Cr layer is deposited via evaporation (PLS-500). This is necessary because the substrate is not conducting and a suitable conductance is necessary for the subsequent e-beam writing.

**E-beam writing:** The mask for the e-beam writing is designed with AutoCAD. The e-beam writer VISTEC EBPB 5000 plus is used, the exposure dose is  $500\mu\text{C}/\text{cm}^2$ . Due to the high energy of the electron beam, the PMMA polymers are cracked at the areas that are exposed to the beam. These cracked polymers are subsequently removed with a developer.

**Cr etching and development of PMMA:** To etch the Cr layer a special mixture is used, which consists of ceric ammonium nitrate, perchloric acid and water. With a Cr etching rate of about 80 nm/min, we use 12 s for etching. After that, the sample stays in propanol

for 1 min. For the development, the sample is dried with nitrogen gas and immersed in the developer AR600-55 for 90 s. Now only the inverted pattern is left.

*Ti/Pt evaporation:* For the metallic structure, first 5 nm Ti is deposited as an adhesion layer and on top 25nm Pt is deposited as the main conducting layer. Both metals are evaporated and cover the PMMA and the open areas.

*Lift-off:* To achieve the final structure, the PMMA with the Ti/Pt layer is removed (lift-off). This is done by leaving the sample in acetone for 15 min. In the end the acetone is removed with propanol (3 min ultrasonic bath) and dried with nitrogen gas. Only the final structure is left over (Figure 3.9).

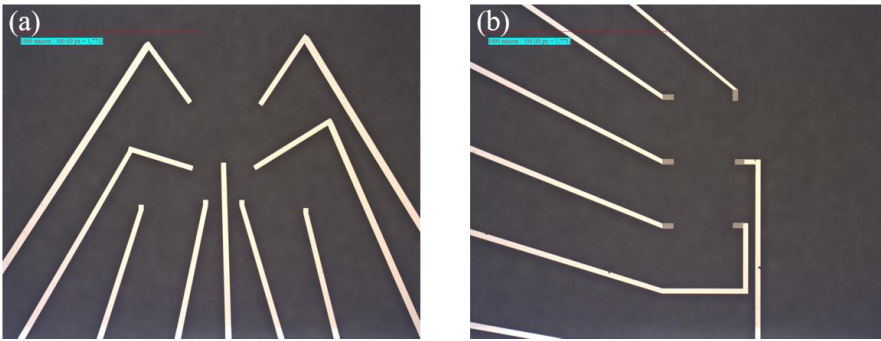


*Figure 3.9: Designed electrode structure transferred onto the quartz wafer, after all the lithography and lift-off processes, (a) and (b) are examples of electrode structures for different neuroelectronic test patterns.*

### 3.2.3 Etching

In case of high-temperature process which are, for instance, necessary for the ALD (typical 150°C to 300°C) of our oxides, the lift-off technology cannot be used for patterning. In these cases the lithography is performed on the coated substrate and the pattern is etched into the top layer. In this work, we used reactive ion etching (RIE) for the patterning of our oxides (Figure 3.10).

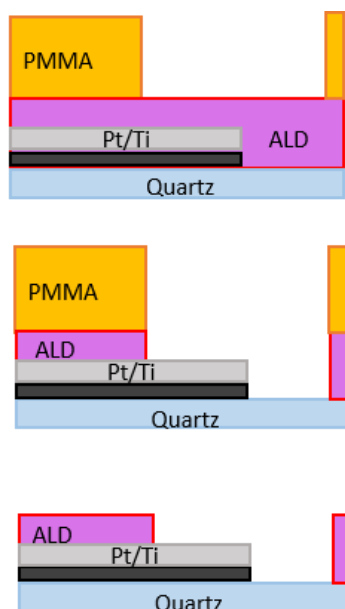


*Figure 3.10: Schematic of RIE process, the photoresist pattern obtained by electron beam lithography is physically or chemically etched (RIE). Since the protective resist and the metal parts have a much slower etching speed compared with the ALD layer, the ALD layer is removed at the open area leaving the metal electrodes unharmed. By removing the remaining PMMA the desired structure is obtained.*

The RIE process represents an inverted sputter process using chemical reactions of the process gas to selectively enhance the removal of the material (here the ALD layer) and avoid removal of PMMA and other materials (here Pt and Ti). We used an Oxford Plasmalab 100, the process parameters were a 1:10 gas mixture of O<sub>2</sub> and CF<sub>4</sub> at a pressure of 0.004 hPa, a substrate temperature of ~20 °C, and a power of 10 W yielding an etching rate of 0.6 nm/s. The remaining PMMA was removed in acetone in an ultrasonic bath for 15 min, then cleaned with propanol in an ultrasonic bath for 3 min, and dried with nitrogen gas. The resulting etching profile was checked with a Tencor Alphastep profilometer. A typical optical image of the resulting pattern is shown in Figure 3.11.

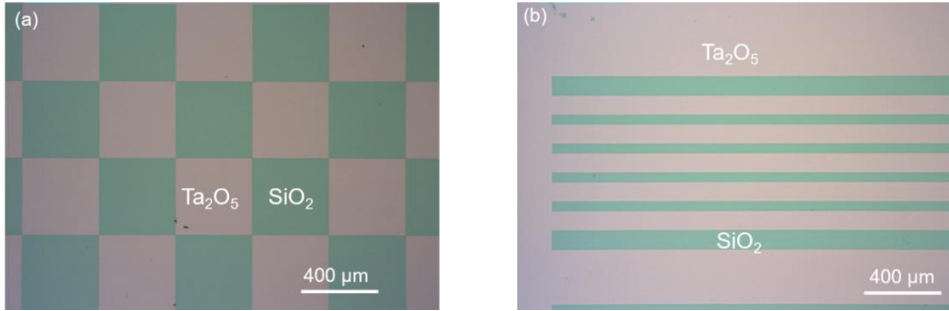


Figure 3.11: Microscope image of a patterned  $Ta_2O_5$  layer on  $SiO_2$  after  $e$ -beam lithography and RIE showing different test structures (chessboard (a) or bars (b)) consisting of  $Ta_2O_5$  surfaces (reddish) and  $SiO_2$  surfaces (greenish).

In order to ensure that after the RIE the designed structures are successfully transferred onto the ALD layer, a scan on the surface has been applied via a Dektak profilometer. Scanning position and direction are shown in Figure 3.12. The height difference between the structures with and without ALD layer is around 36 nm, which is slightly larger than the 30 nm thick ALD layer, demonstrating a slight over etching of the openings of the MEA structure.

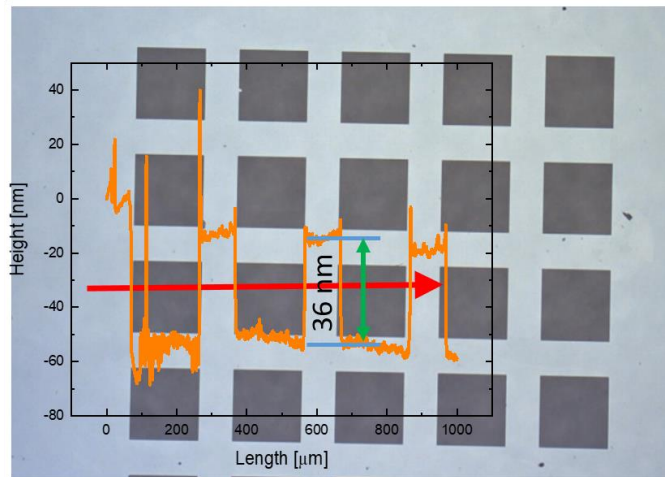


Figure 3.12: Scan of an ALD MEA test pattern via profilometer. Scan position and direction are shown as the red arrow, the background illustrates the patterned structure consisting of the ALD layer (brighter) and the openings to the metal (darker).

### 3.3 Characterization methods

In the following the different characterization methods used in this work are described.

#### 3.3.1 Ellipsometry

Ellipsometry represents a very sensitive and non-destructive optical method to determine the properties of thin film such as composition, thickness, refractive index, conductivity, or even porosity [109].

When a beam of polarized light is incident on a substrate surface, only part of the incident light is transmitted into the substrate. The reflection of the polarization is determined by the complex refractive index, incident angle, and the polarization of the light. The polarized incident light on the substrate surface can be spitted into two components:

- the  $s$  component, which oscillates perpendicular to incident plane (defined by the incident and reflect lights) and parallel to the substrate surface, and
- the  $p$  component, which oscillates parallel to the incident plane [110].

The amplitudes of the  $s$  and  $p$  components after reflection and normalized to the incident values are represented by  $r_s$  and  $r_p$ , respectively. The complex reflectance ratio  $\rho$  of the system is then given by the ratio between  $r_p$  and  $r_s$ :

$$\rho = \frac{r_p}{r_s} = \tan(\Psi)e^{i\Delta} \quad (8)$$

where  $\tan(\Psi)$  is the amplitude ratio of reflection, and  $\Delta$  is the phase shift. By choosing a suitable model to fit the data  $\Psi$  and  $\Delta$  can be analyzed, the corresponding thickness of the sample can be calculated.

A schematic sketch of an elipsometer used for the analysis of a layer system consisting of an APTES SAM on  $\text{SiO}_2$  terminated Si is shown in Figure 3.13a. We usually start with a thickness analysis of the  $\text{SiO}_2$  terminate Si wafer, which yields a typical thickness of  $\sim 90$  nm (Figure 3.13b). By repeating the experiment after the deposition of the molecular layer (here APTES) (Figure 3.13c) and inserting the refractive indices of APTES which is similar to the one of  $\text{SiO}_2$  ( $\epsilon_{opt}(\text{SiO}_2) \approx 1.416$ ), we obtain a slight increase of the total thickness (Figure 3.13c). By subtracting the substrate  $\text{SiO}_2$  value, the thickness of  $\sim 0.7$  nm for the molecular layer is obtained (Figure 3.13d).

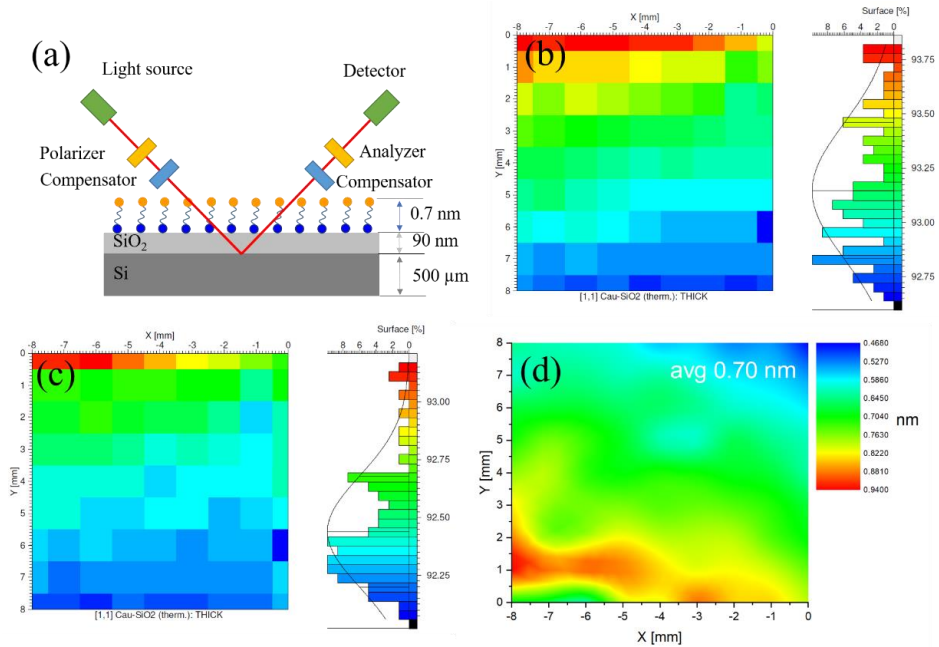


Figure 3.13: (a) Schematic of a typical ellipsometry analysis of our films. The incident laser beam is polarized via a polarizer and hits the surface, after reflection from the sample surface, the beam passes the analyzer and is collected in the detector. Depending on the coating of APTES SAM layer, there is a slight enhance of the thickness of the resulting layer. Measurements of SiO<sub>2</sub> terminate Si substrate without molecules (b) and with molecules (c) lead to the resulting contour plot (d) of the thickness of the APTES monolayer.

### 3.3.2 Contact angle measurements

Contact angle measurements are used in this work to determine the hydrophilic/hydrophobic properties of the substrates.

The contact angle measurement represents an effective method to analyze the surface interaction including three phases (solid, liquid, and air). A drop (typical water) of liquid on a flat and horizontally orientated surface forms an angle at the intersection of the liquid-vapor and liquid-solid interface as indicated by the tangent line from the contact point along the liquid-vapor interface (Figure 3.12a). This angle is the so-called contact angle  $\Theta$  (Figure 3.14a) [111]. Since air and water are not changed (also the temperature and pressure are identical for all measurements), the shape of a liquid drop on the surface, which is examined, reflects the free energy of the system and, therefore, allows to determine specific surface properties such as the surface energy.

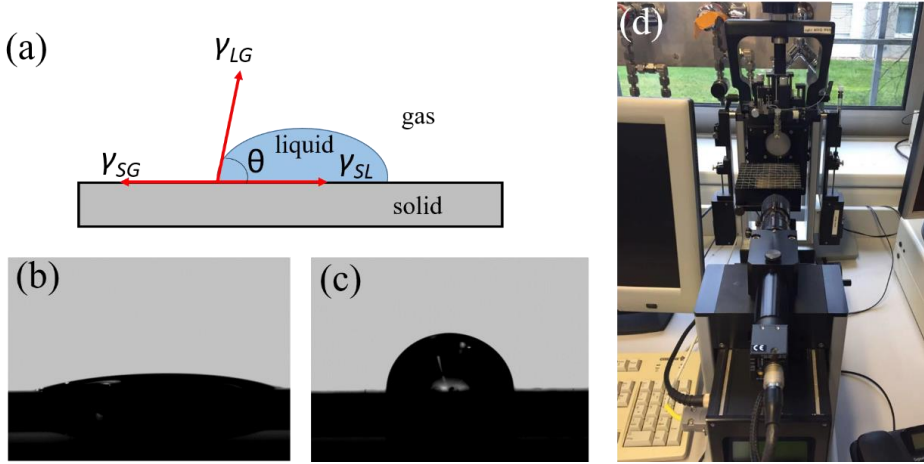


Figure 3.14: (a) Schematic of the contact angle  $\Theta$  of the solid-liquid-gas system with interfacial energies  $\gamma_{SL}$ ,  $\gamma_{SG}$ ,  $\gamma_{LG}$  of the solid-liquid, solid-gas and liquid-gas interfaces, respectively. Furthermore, water drop of  $10 \mu\text{L}$  on the hydrophilic surface (b) and on the moderate hydrophobic surface (c) and the contact angle measuring system OCA15EC (Dataphysics) used in this work (d).

Theoretically, the contact angle is expected to be a characteristic property of a given surface in the particular environment. As first defined by Thomas Young [112], the three equilibrium interfacial tensions are described by Young's equation:

$$\cos(\Theta) = \frac{\gamma_{SG} - \gamma_{SL}}{\gamma_{LG}} \quad (9)$$

where  $\gamma_{SG}$  is solid-vapor interfacial energy,  $\gamma_{SL}$  is solid-liquid interfacial energy and  $\gamma_{LG}$  is liquid-vapor interface energy.

In case of water, a large water contact angle  $\Theta > 90^\circ$  represents a hydrophobic surface whereas a small contact angle  $\Theta < 90^\circ$  is characteristic for a hydrophilic surface. Moreover, the contact angle can also be used for the characterization of a given SAM.

In this work the contact angle was measured via the "sessile drop method" using a setup OCA15EC (Dataphysics). It is based on the investigation of the complete shape of a water drop on the planar solid surface. The image of the drop is achieved with a camera and the contact angle is analyzed automatically [104].

### 3.3.3 Surface potential measurement

In this work we used the streaming current method to determine the electrokinetic potential ( $\zeta$  potential) of our samples which is correlated to the surface charge (Figure 3.15). The electrical double layer (EDL) which forms if solid surfaces get in contact with a polar medium has already been introduced in chapter 2.4.2. This EDL consists of an immobile layer and a mobile layer (Figure 3.15a). The electrical potential at the solid surface cannot be determined experimentally. However, the electrical potential at the shear plane, the boundary between the immobile layer and the mobile layer, the so called  $\zeta$  potential, can be measured and therefore represents a very important property of the solid-liquid interface. It is given by:

$$\zeta = \Psi(d) \quad (10)$$

with  $d$  the distance between shear plane and surface (Figure 3.15).

In the immobile layer the potential has a linear dependence with the distance  $x$ , whereas in the mobile layer it changes exponentially with  $x$ :

$$\Psi(x) = \Psi(d)e^{-\kappa(x-d)} \quad (11)$$

Where  $x$  represents the distance,  $d$  is distance between shear plane and surface, and  $\kappa^{-1}$  is the Debye length.

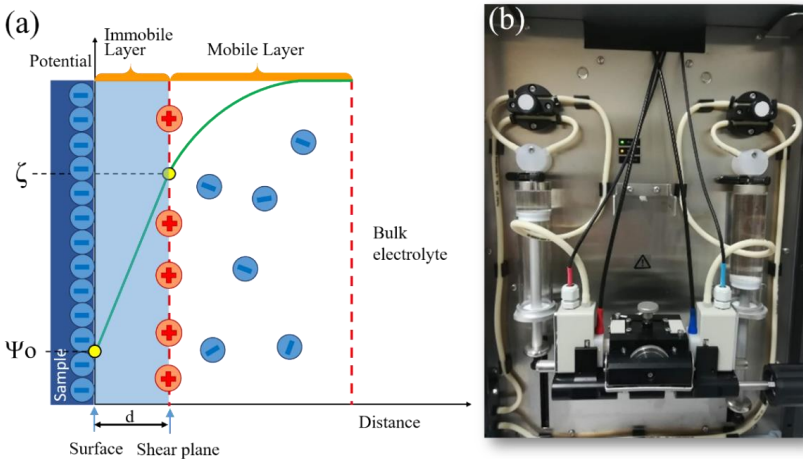


Figure 3.15: (a) Schematic of the electrical double layer (EDL) according to the Gouy-Chapman-Stern-Grahame theory and (b) image of the surface potential measurement setup (electrokinetic analyzer SurPASS).

In order to analyze the surface potential of the molecular layer, an electrokinetic analyzer (SurPASS Figure 3.15b, Anton Paar Germany GmbH) is used. A pair of identical planar substrates (10 mm × 10 mm) is placed in a clamping cell, with the surfaces facing each other and forming a microfluidic channel (Figure 3.16a). To obtain a large signal, a small separation (typically 70~100 μm) between the two plane-parallel surfaces is chosen that enabled a laminar flow of the electrolyte (Figure 3.16b). The ζ potential is determined using the Helmholtz-Smoluchowski equation [113] (lab protocol),

$$\zeta = \left( \frac{dl}{dp} \right) \left( \frac{\eta L}{\varepsilon \varepsilon_0} A \right) \quad (12)$$

where p is the pressure necessary to generate the laminar flow; η and ε are the viscosity and dielectric constant of the electrolyte; ε<sub>0</sub> is the vacuum permittivity; L and A represent the length and cross section of the flow channel, respectively; and I is the resulting current measured between two electrodes (Figure 3.16c) placed at each side of the measuring cell. The resulting ζ potential represents the electrokinetic potential at the shear plane between the mobile and immobile Helmholtz layers and is a measure of the surface potential [113].

The pH value of the electrolyte is adjusted via titration. In this work, we focused on the pH range (pH 4.5-9.5) covering the physiological conditions, pH 6-8, for the natural milieu of organism and cell systems. Electrolyte and titration solutions are aqueous solutions based on Milli-Q water containing potassium chloride (1 mM KCl) in the case of the working electrolyte and a gradual titration using a basic electrolyte of 50 mM KOH. During the experiment, the temperature of the medium was kept constant at 25 °C. Furthermore, the reservoirs for the working electrolyte and the titration electrolyte were encapsulated to minimize contact with air and a N<sub>2</sub> purger was used to suppress the formation of hydrocarbonates (HCO<sub>3</sub><sup>-</sup>), which can form if CO<sub>2</sub> is dissolved in the aqueous solution. Prior to each experiment, the experimental setup was rinsed with 2 L of Milli-Q water and subsequently with the working electrolyte solution. Before each series of measurements, pH and conductivity electrodes were calibrated with the corresponding calibration buffer solutions [114].

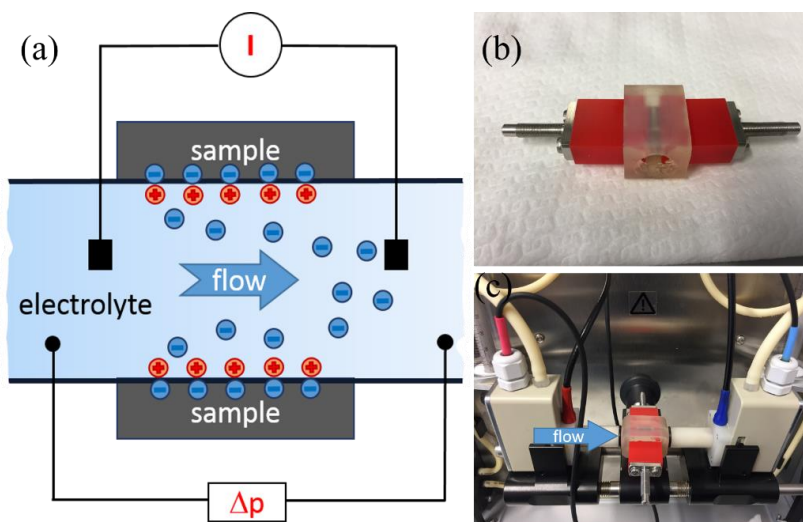


Figure 3.16: (a) Schematic of the major component of the streaming current measurements setup consisting of a pair of identical planar substrates placed in a clamping cell with the surfaces to be analyzed facing each other and forming a microfluidic channel, as well as electrodes and sensors to determine the electric current as function of the flow of the electrolyte. (b) Image of planar substrates placed in the microfluidic channel. (c) Photo of incoming electrolyte flow and the electrodes.

### 3.3.4 X-ray photoelectron spectroscopy

X-ray photoelectron spectroscopy (XPS) represents an often used nondestructive and quantitative surface analysis technique for the characterization of organic and biomaterials. It allows to determine the atomic composition at the surface, chemical bonds, oxidation states, quantification of elements, and analysis of contaminations [115].

The sample to be analyzed is exposed to an irradiation with high energy X-rays. The X-ray penetrates only 1-10 nm into the surface and are absorbed by the atoms. If the energy is large enough, electrons with a characteristic energy are ejected (Figure 3.17).

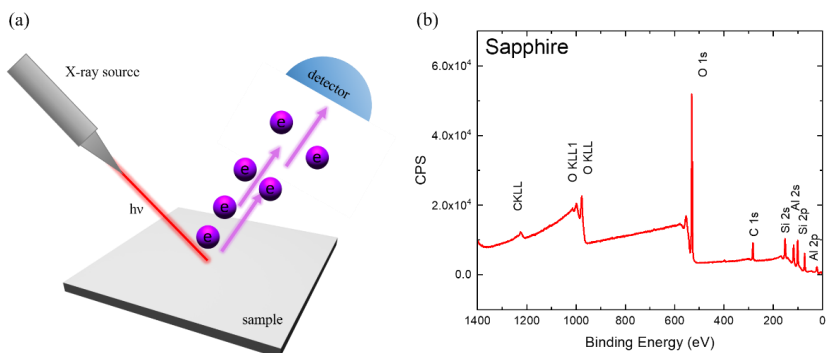


Figure 3.17: (a) Schematic of an X-ray photoelectron spectrometer. An X-ray penetrates the sample and generates electrons with characteristic energy. The detector collects and identifies the electron binding energy. (b) X-ray spectrum of a thin ALD  $\text{Al}_2\text{O}_3$  film on  $\text{SiO}_2$ .

The ejected electron possesses a kinetic energy which is defined by the energy  $h\nu$  of the incident beam, the binding energy and work function of the substrate. The XPS detector records the number of electrons with identical binding energy which is then providing the amount of the corresponding atom in the sample. This allows to detect the atomic percentage per element in the examined surfaces. The detection limit of XPS is typically 100 ppm for most elements.

The XPS device used in this thesis was a Phi5000 VersaProbeII (ULVAC-Phi Inc., USA.) with an Al K-alpha X-ray source with a photon energy of 1.486 keV and a resolution of 0.8 eV.

### 3.3.5 X-ray diffraction

The crystalline structure of samples can be analyzed by X-ray diffraction (XRD) technique. Crystals are regular arrays of atoms and X-rays can be treated as electromagnetic radiation waves. The electrons of the atoms interact with the X-ray which leads to an elastic scattering of the X-ray. For regular lattices (e.g. crystalline structure) most of the scattered waves are canceled with each other in most directions because of the destructive interference. However, in a few specific directions a constructive interference takes place. The respective angles are given by Bragg's law (see Figure 3.18a):

$$2d\sin\theta = n\lambda \quad (13)$$

where  $d$  is the spacing between diffracting planes,  $\theta$  is the incident angle,  $n$  is an integer, and  $\lambda$  is the wavelength of the incident beam.

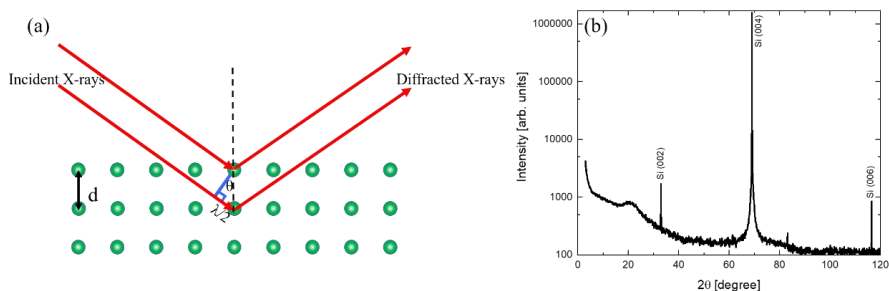


Figure 3.18: (a) Schematic representation of the Bragg equation and (b) example of a XRD spectrum of an ALD  $Ta_2O_5$  thin layer on a  $SiO_2$ -Si substrate.

In this work, XRD was used to study composition and structure of our ALD thin film. Only the crystalline substrate ( $SiO_2$ ) produced one family of peaks in the diffraction pattern (Figure 3.18b), which indicate that this ALD layer doesn't form a crystalline structure.

### 3.3.6 Scanning electron microscope

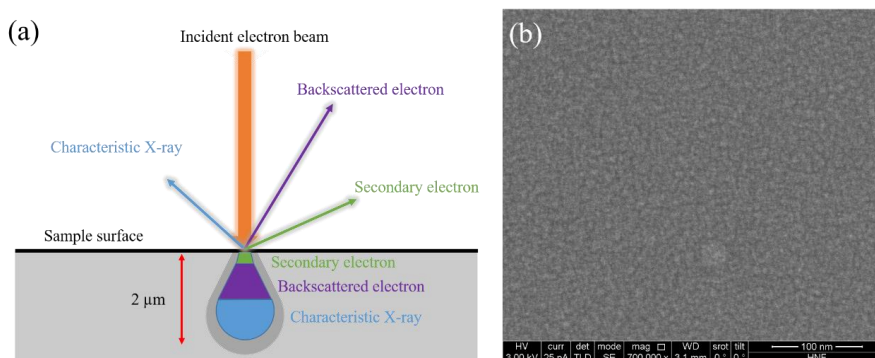


Figure 3.19: (a) Generation of electron signals emitted by the interaction between the incident electron beam and the specimen surface. (b) Surface morphology of an ALD  $Ta_2O_5$  thin film. Figure (a) adapted from [116].

The “visual” inspection of a sample is still one of the most important tools to obtain information and understand problems of a sample. Next to the simple solution, provided by optical microscopy, the scanning electron microscopy (SEM) offers images of the samples' morphology down to nm scale. SEM is based on a focused beam of high-energy electrons which generates electron signals at the surface (Figure 3.19a). The surface morphology, chemical composition, and crystalline structure affect the electron-sample

interactions and lead to various signals including secondary electrons, which are used to obtain produce SEM images of the morphology and topography of the samples.

In this work a Gemini 1550 (Zeiss) was used for the characterization of ALD films and critical point dried cell culture. Figure 3.19b shows an example of a SEM picture of an ALD Ta<sub>2</sub>O<sub>5</sub> thin film. Due to the low conductivity of the ALD sample and the dried cell cultures, a thin layer of platinum, normally 10 nm thick was sputtered onto the sample before SEM measurement.

### 3.3.7 Fluorescence microscopy

In this work, fluorescence microscopy has been used for visual detection and analysis of

- (i) APTES (combined with fluorescein isothiocyanate (FITC)) on the ALD substrates,
- (ii) live-dead staining of neuronal cells cultures stained with fluorescent dyes.

The ability of fluorescent molecules to absorb and subsequently emit light is called photoluminescence. The mechanism of absorption and emission of light of a fluorophore can be illustrated in the Jablonski energy diagram (Figure 3.20a). Upon absorption of light, an electron is excited from the ground state ( $S_0$ ) to a higher energy states (e.g.,  $S_1$  or  $S_2$ ) in a few femtoseconds (Figure 3.20a blue arrow). Within picoseconds, the electron in the excited state undergoes a relaxation within the electronic energy states (without radiation) and an internal conversion between neighboring electronic energy states (Figure 3.20a yellow arrow). After this (nanosecond-scale), the electron returns to its ground state with an emission of light at a characteristic wavelength (Figure 3.20 green arrow). This signal is then detected with a photosensitive detector [117]. Normally, the absorption happens at a small wave length (high energy) and the emission at a large wavelength (low energy), as shown in Figure 3.20b.

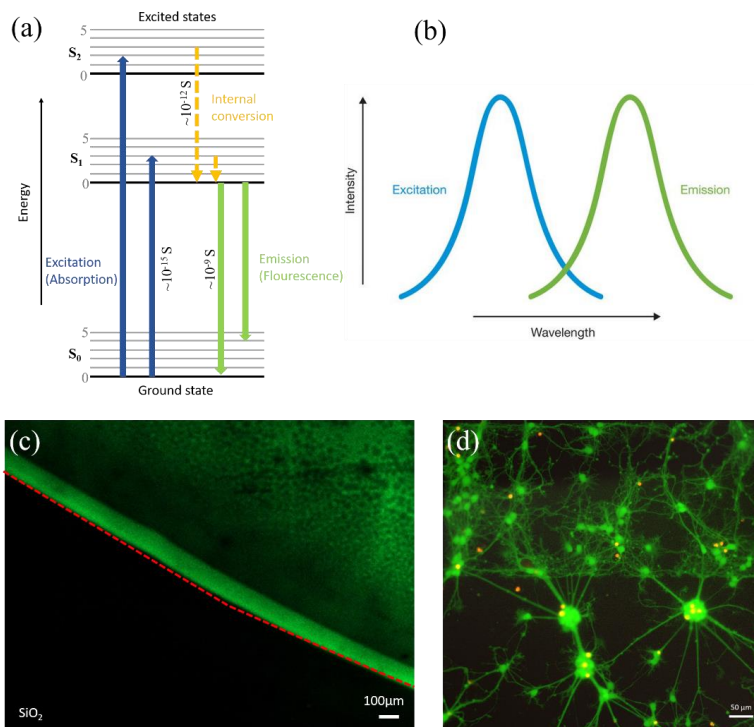


Figure 3.20: (a) Jablonski energy diagram illustrating the electronic states of a fluorophore and the different transitions between electronic states. The transitions can be nonradiative (dashed arrows) or radiative (straight arrows), and occur at different timescales.  $S_0$  is the ground state;  $S_1$  and  $S_2$  are excited energy states. (b) The emission of fluorescence signals generally occurs at a longer wavelength. (c) an example of fluorescence microscope image of a  $\text{SiO}_2$  terminated Si substrate covered with APTES molecules and FITC. (d) Neurons after live/dead staining.

In this work, fluorescence microscopy investigations of the molecular layers and cell cultures were carried out via a Zeiss Apotome microscope using the Zen software. FITC, a fluorescein molecule functionalized with an isothiocyanate reactive group replacing a hydrogen atom on the bottom ring of the structure, was used as an optical marker. It is reactive with respect to nucleophiles, including amine and sulfhydryl groups on proteins, and thus binds to APTES (the structure of FITC and its reaction mechanism is shown in Figure 3.21). FITC was mixed in Milli-Q water to a concentration of  $10 \mu\text{g/mL}$ . The samples were coated with a drop ( $45 \mu\text{L}$ ) of the FITC solution and kept at room temperature for 1 h avoiding any exposure to light. The remaining drop was then removed from the surface by rinsing with Milli-Q water and washing away the part that has not bonded to the SAM. The sample was subsequently rinsed in Milli-Q water for 5 min and purged in a  $\text{N}_2$

flow. As a result, only FITC that is bonded to chemisorbed APTES remains on the surface, unbound FITC and FITC bonded to only physisorbed APTES is removed during the rinsing (Figure 3.20c).

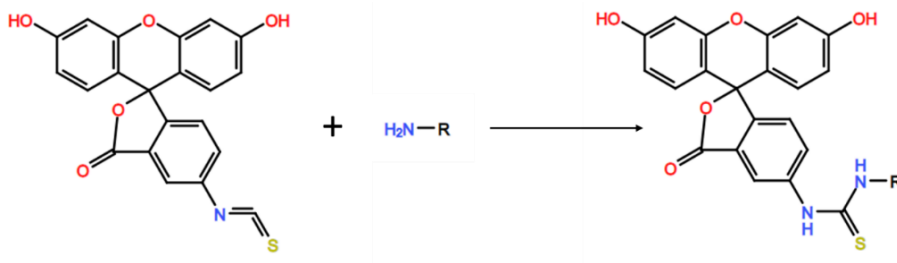


Figure 3.21: Schematic of the reaction of FITC with amine-containing compounds like APTES [118].

In case of neurons (Figure 3.20d), we used 1  $\mu\text{g/ml}$  Calcein-AM and 2  $\mu\text{M}$  Ethidium Homodimer (both Life Technologies) in supplemented cell growth medium to stain live and dead cells in green and red, respectively. After the staining the cell statistics was performed via the software ImageJ [119] as well (lab protocol).

## 3.4 Cell culture

In this work we used cortical neurons and HL-1 cells to demonstrate their biocompatibility with various oxides, with and without APTES coatings. The necessary techniques are described in this chapter.

### 3.4.1 Cortical neuron culture

Before preparation of the cell culture, the samples were sterilized by dipping them into ethanol for a few seconds and subsequently removing the ethanol in a  $\text{N}_2$  flow. Cortical neurons were obtained from E18 Wistar rat embryos. Briefly, the cortex was dissected from the embryonic brain tissue and digested with trypsin-EDTA at 37  $^\circ\text{C}$ , 5 %  $\text{CO}_2$ , and 100 % humidity for 10 min. To remove trypsin, the cortex was washed three times with neurobasal medium (Life Technologies GmbH, Germany) supplemented with 1 % B27 (Life Technologies, Germany), 0.5 mM L-glutamine, and 50  $\mu\text{g/ml}$  gentamicin. Then, the cortex was dissociated gently with a 1 mL pipette. Cell clumps and glia cells were allowed to settle for 2 min at room temperature. The supernatant was diluted in supplemented neurobasal medium, and 100 k cells per substrate per well were plated in a 12-well culture

dish. The medium was replaced completely 4 h after plating. Over the following days, half of the medium was changed twice per week. Animal work was carried out with the approval of the Landesumweltamt für Natur, Umwelt und Verbraucherschutz Nordrhein-Westfalen, Recklinghausen, Germany, number 81-02. 04. 2018. A190 [120].

### 3.4.2 HL-1 cell culture

The cardiomyocyte-like cell line HL-1 was cultured in T25 flasks. When reaching fully confluency, the cells were passaged and seeded on top of the MEAs at 10k cells per chip. The chips were then placed in an incubator (37 °C, 5% CO<sub>2</sub>) for the cells to mature. Claycomb medium, supplemented with 10% fetal bovine serum, 100 U/ml-100 µg/ml penicillin-streptomycin, 0.1 mM norepinephrine and 2 mM L-glutamine is exchanged on a daily basis and two hours before the measurement (lab protocol). [81, 121]

### 3.4.3 Live-dead staining

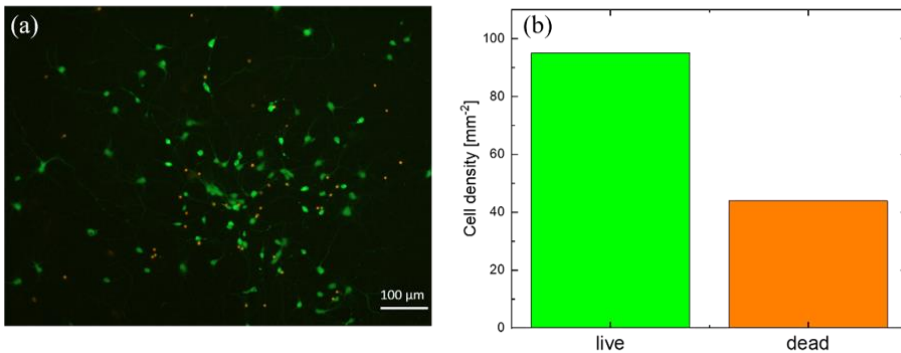


Figure 3.22: (a) Fluorescent microscope images of live/dead cell distributions for borosilicate glass (BSG) treated with PLL, (b) statistics of live/dead neurons after DIV 6 on average over several areas of size 0.6 mm<sup>2</sup>.

Live/dead staining was performed using 1 µg/mL calcein-AM and 2 µM ethidium homodimer (both Life Technologies) in supplemented cell growth medium to stain live and dead cells green and red, respectively. The calcein-AM dye shows a strong green fluorescence, with 495 nm excitation wavelength and 515 nm emitted wavelength. Live cells have intracellular esterases that convert nonfluorescent, cell-permeable calcein acetoxymethyl to the intensely fluorescent calcein. Cleaved calcein is retained within cells. In case of dead cells, the ethidium homodimer enters damaged cells and is fluorescent when

bound to nucleic acids. Ethidium homodimer produces a bright red fluorescence, excitation with 528 nm wavelength and emitting with 617 nm wavelength in dead cells. Cells and dyes were incubated for 15 min at 37 °C. An example of cortical neuronal cells live-dead staining at DIV 6 with the corresponding statistics of live/dead neurons is shown in Figure 3.22 (lab protocol). [104]

### 3.4.5 Critical point drying

In order to visualize features of cells and networks on the different oxides, the technique of critical point drying (CPD) in combination with electron microscopy (SEM) was used. For CPD, the substrate with the cell culture was rinsed 3 times with PBS (phosphate-buffered saline, 37 °C, Sigma Aldrich, USA), then fixed with diluted glutaraldehyde (Sigma Aldrich, USA) in PBS (3.2%) for 15 min at room temperature, followed by rinsing with PBS and Milli-Q water to remove the fixative residues. Subsequently, the water was exchanged via an ethanol series of 5 min in 10 %, 30 % and 50 %, 15 min in 70%, and 3 times for 5 min each in 90 % and 95 %. Then, the sample was stored in 100 % ethanol at 4 °C, and in a next step transferred into the chamber of the critical point drying (CPD) system (CPD 030, BAL-TEC Company), which was filled with 100 % ethanol. First, the chamber was slowly cooled down to 10 °C, and then ethanol was exchanged with liquid CO<sub>2</sub>. This exchange process was repeated several times until the chamber was filled mainly with liquid CO<sub>2</sub>. Then, the temperature of the chamber was increased up to 40 °C, followed by an increase in pressure to 73.8 bar causing the transformation of CO<sub>2</sub> into a supercritical form. Eventually, the chamber was evacuated, and the sample was dried and dehydrated [120].

The subsequent SEM characterization of the dried cell culture was carried out with a Gemini 1550 instrument (Leo/Zeiss) using an in-lens detector. To enhance conductivity, a thin layer of platinum (approximately 5 nm) was sputtered onto the sample. The imaging was taken at 1 kV acceleration voltage. One example of a neuronsphere on Ta<sub>2</sub>O<sub>5</sub> is shown in Figure 3.23.

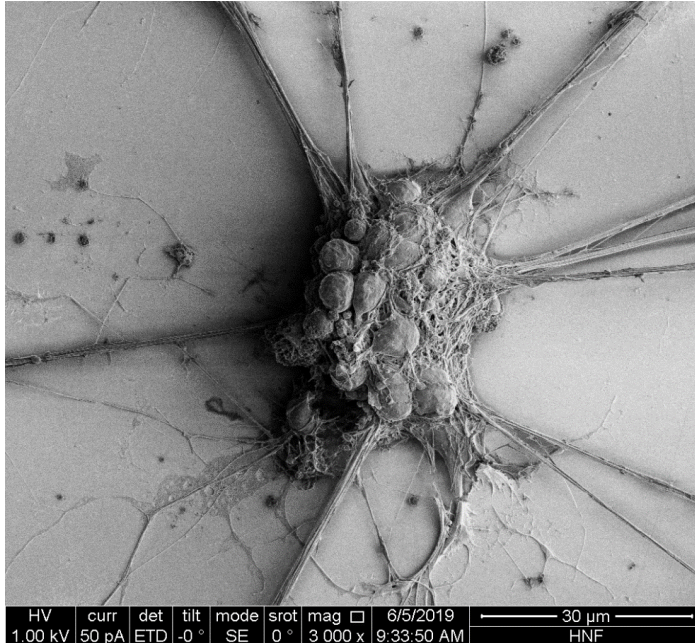


Figure 3.23: SEM morphology of cortical neuronal cells after CPD. Here is an example of neuronsphere on the  $Ta_2O_5$  surface.

### 3.5 Electrical characterization

In order to recording the electronic signal (APs) of the cells, certain preparation steps are necessary which contains MEA preparation, chip encapsulation and BioMAS system experiment.

#### 3.5.1 Multi electronic arrays

MEAs are simple electronics devices that allow to transfer the electronic signal between cell and electrode. Therefore, they can be used for the communication of cells and electronics. Figure 3.24a depicts a design of ALD layer based MEAs as employed in this work. MEAs provides a huge amount of advantages for *in vitro* cell-chip investigation, since this method is non-invasive and enables a long-term culture.

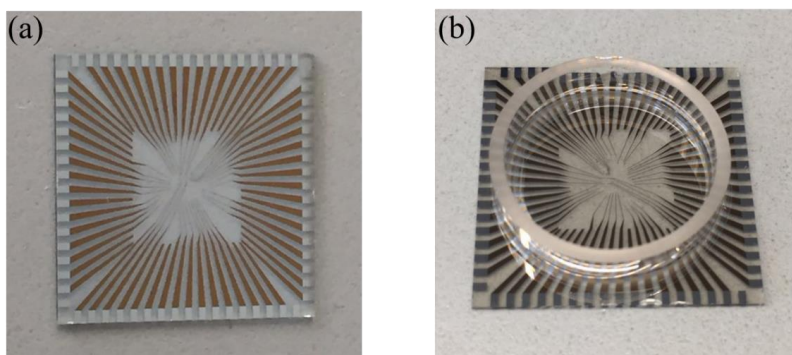


Figure 3.24: Image of the ALD layer based MEA structure without (a) and with encapsulation (b).

### 3.5.2 MEA Encapsulation

In order to perform cell cultures on the MEAs, the samples needed to be encapsulated for holding a certain amount medium for a certain time, therefore a glass ring with an outer diameter of 20 mm (17.8 mm inner diameter) was glued on top of the  $24 \times 24 \text{ mm}^2$  MEA chip using PDMS (10:1, Sylgard). The height of the glass ring is 4 mm, which allows enough volume for the culture medium (Figure 3.24b). Prior to the cell culture, the chips were coated with APTES, then transferred into the sterile bench and sterilized with 70% ethanol (lab protocol).

### 3.5.3 BioMAS

The bioelectronic Multifunctional Amplifier System (BioMAS) is an in-house developed set-up, aimed for versatile and standardized measurements of different kind devices on a single platform. The platform consists of a pre-amplifier (head stages, designed by Jan Schnitker (Forschungszentrum J lich), Figure 3.25a) and a main amplifier ( $1\times$ ,  $10\times$  or  $100\times$  amplification) (built by Stefan Eick Schnitker (Forschungszentrum J lich)).

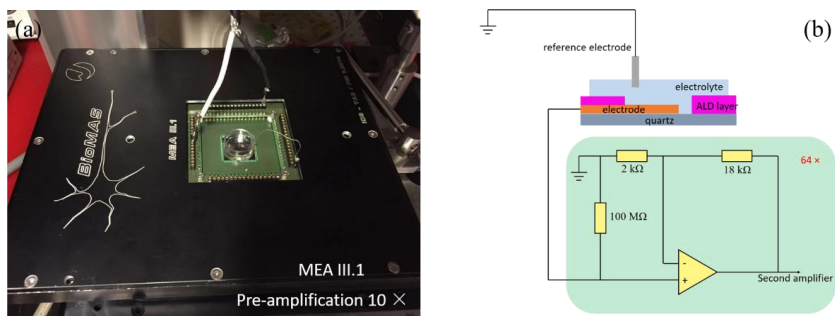


Figure 3.25: (a) Image of the BioMAS headstage, (b) simplified schematics of the MEA headstage. Each of the 64 electrodes is sampled separately but simultaneously and each signal is pre-amplified by a factor of ten.

The headstage is customized to a specific device type and geometrical layout of its I/Os, and comprises of a chip holder, operational amplifiers and some control circuits. For high input impedance, the MEA headstage is acting as a non-inverting amplifier it performs a first amplification by a factor of ten. The schematic circuit of the 64 channels MEA headstage is shown in Figure 3.25b.

The measured signal from the MEA headstage will be transported to the main amplifier, the further main amplifier contains two amplification stages and a high pass filter. The main amplifier, apart from amplifying, has other functions: it has some pre-installed low-pass filters. The analog to digital converter (ADC) unit converts voltages, coming out from the main amplifier to 16-bit digital values. The ADC has a voltage range of  $\pm 10$  V, a sampling rate of  $1.25 \times 10^6$  samples per second on a single channel or  $750 \times 10^3$  samples per second, if distributed on all channels. The 64-electrode measurements therefore result in a typical sampling frequency of 10 k Hz. The control of the measurements is done via LabVIEW-based software, developed by Dieter Weber (Forschungszentrum J lich), updated by Fabian Brings (Forschungszentrum J lich) and Jan Schnitker (Forschungszentrum J lich) in the institute. The data is processed by the BioMAS viewer in Python software wrote by Fabian Brings (Forschungszentrum J lich) and Johannes Lewen (Forschungszentrum J lich). In order to minimize any disturbance noise of the measurement, the setup is placed in a custom-made Faraday cage on a vibration isolated table (lab protocol). [81]

## 4. Results and discussion

In this work, we are aiming to fabricate a neuroelectronic device that can be used for guided neuron cell growth as well as good cell-chip communication. Therefore, the experimental results of this work are divided in three steps:

- (i) First, the understanding of the MLD process is the fundamental for achieving a biocompatible neuroelectronic interface, therefore a systemic investigation of the vapor-phase deposition and APTES SAMs' electronic properties on  $\text{SiO}_2$  is shown in chapter 4.1.
- (ii) Then, the deposition of APTES on various ALD oxides ( $\text{TiO}_2$ ,  $\text{Al}_2\text{O}_3$  and  $\text{Ta}_2\text{O}_5$ ) and a test guided neuron cell growth structure is produced via combination of ALD oxides and APTES SAMs, see details in chapter 4.2.
- (iii) Finally, ALD MEAs are designed and characterized for the aim of achieving guided growth and signal recording with HL-1 cells and cortical neuron cells. This is discussed in chapter 4.3.

### 4.1 Vapor-phase deposition and electronic properties of APTES SAMs on $\text{SiO}_2$

In this chapter, we carefully analyze the molecular layer deposition of APTES on ozone-activated  $\text{SiO}_2$  substrate. Electrokinetic potential analyses are applied to record and optimize the gas-phase deposition of molecular SAMs and to determine the resulting change of the  $\zeta$  potential and charge at the solid-liquid interface of substrate and electrolyte.

The following topics are discussed:

- (i) The key aspects of APTES SAM deposition, characterization, and the resulting optimization of the deposition process are presented. It turns out that a stable  $\zeta$  potential can only be obtained for perfect SAMs which requires an adequate post-deposition treatment (PDT). This is discussed in chapter 4.1.1.
- (ii) In contrast to bare and untreated substrates, we observe a significant decrease of the electrokinetic charge and potential for the activated  $\text{SiO}_2$  and a small increase of the electrokinetic charge and potential for the APTES-coated  $\text{SiO}_2$ . The corresponding titration analysis of the surface potential is given in chapter 4.1.2.
- (iii) Finally, the resulting modification of the electrokinetic charge at the solid-liquid interface caused by the molecular layer is analyzed in chapter 4.1.3.

### 4.1.1 Deposition of self-assembled APTES monolayers

All our APTES layers are deposited from the gas phase using a specially developed MLD deposition device [102] that allows all process steps to be performed without breaking the vacuum. The deposition steps include:

- (i) Cleaning and activation of the substrates via ozone exposure.
- (ii) Deposition of the molecules, typically at room temperature in Ar gas at 0.1 hPa.
- (iii) Post-deposition treatment (PDT) in vacuum, which as will be shown in this chapter, is essential for the APTES SAM formation.

In process (i), the substrate's surface can be in different states, defined as:

- *chemical cleaned*: The 'virgin' sample is only cleaned in alcohol.
- *ozone-cleaned/inactive*: Additionally to the chemical cleaning, the substrate is exposed to an ozone treatment to remove residual organic impurities. In order to remove the activation of the surface, the sample is stored in a container for at least 2 weeks.
- *ozone-cleaned/activated*: Similar to ozone-cleaned/inactive, however the sample is used in the activated state, i.e. directly or shortly after ozone exposure.

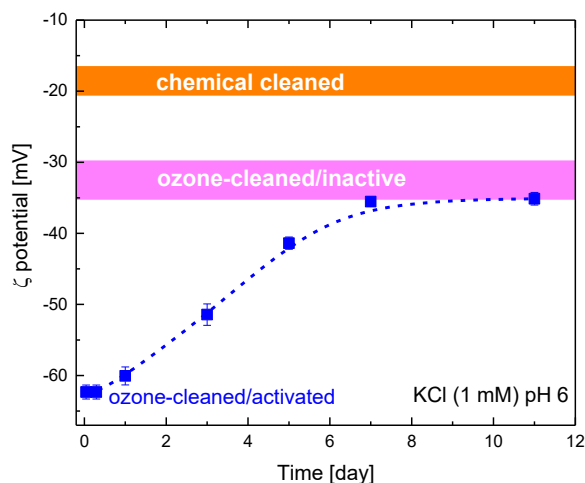


Figure 4.1:  $\zeta$  potential of ozone-cleaned/activated Si/SiO<sub>2</sub> as a function of time for a 1 mM KCl electrolyte. The two bars indicate the  $\zeta$  potential for the chemical cleaned state and the ozone-cleaned/inactive state achieved after both cleaning steps and recovery of the siloxane state.

Since not all contaminations are removed from the substrate surface via the chemical cleaning step, we added the ozone cleaning step to especially remove organic residues from the surface. For ozone cleaning and activation, the Si/SiO<sub>2</sub> substrates are placed in the MLD chamber, ozone is generated from O<sub>2</sub> via a microwave discharge. At the substrate, the ozone removes residual organic impurities and activates the SiO<sub>2</sub> surface by enabling open silanol surface bonds (Si-OH). The degree of activation can be seen in the strongly reduced  $\zeta$  potential. An exposure of the SiO<sub>2</sub> surface to ozone for 3 minutes is sufficient to reduce the potential from  $\sim (-18.5 \pm 1)$  mV in the chemical cleaned state to  $\sim (-62 \pm 1)$  mV in the ozone-cleaned/activated state (1 mM KCl electrolyte at pH 6). This activation is stable for a few hours, with the silanol groups returning to the more stable Si-O-Si siloxane configuration over time. At room temperature, it takes about 1 week in the electrolyte to finally achieve the non-activated yet stable *ozone-cleaned/inactive state* with a  $\zeta$  potential of  $\sim (-32 \pm 1)$  mV (Figure 4.1). This is the potential we consider to represent the pure SiO<sub>2</sub> surface state. Measurements of the wetting angle confirm this observation. [106]

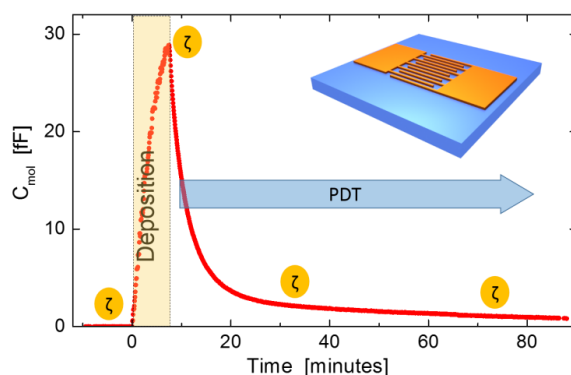


Figure 4.2: APTES deposition process demonstrated via the time-dependent signal of the in situ capacitive sensor (red solid symbols). This begins with the pre-deposition process ( $t < 0$ ) where  $C_{mol} \approx 0$ , followed by the onset of deposition at  $t = 0$  with the first increase of the capacitive signal, and finally, post-deposition treatment (PDT) after closing the molecular source characterized by a decreasing capacitive signal. The inserted schematic shows the interdigitated sensor structure for the capacitive recording of the deposited molecular layer. The differently placed  $\zeta$  symbols indicate that the surface potential is measured for deposition processes terminated at different states (chemical cleaned, ozone cleaned/activated, and for different PDT durations). Inset schematic adapted from lab collection.

The essential process steps, (ii) and (iii), and typical properties of the resulting layer are illustrated in Figure 4.2. It shows the contribution of the molecules to the capacitive signal

recorded by the in situ capacitive sensor of the MLD device during deposition [105]. After opening the APTES source (start of deposition), the signal increases continuously, indicating the deposition of molecules on the sensor and substrates. After closing the source (end of deposition), the signal decreases, indicating that molecules are removed (desorption) from the substrate. After several hours, the capacitive signal stabilizes at a value that is characteristic for the capacitive signal of the resulting APTES layer [105].

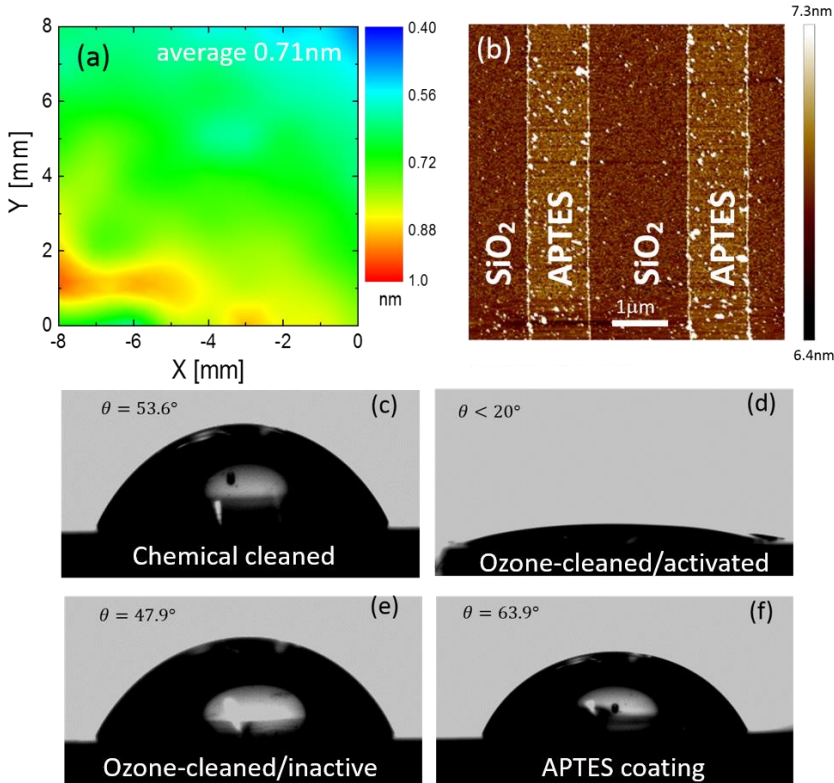


Figure 4.3: (a) Thickness distribution of an 8 mm  $\times$  8 mm APTES SAM ( $t_{PDT} = 24$  h) obtained via ellipsometry, (b) surface morphology of a patterned APTES film ( $t_{PDT} = 24$  h) on SiO<sub>2</sub> obtained via AFM, and contact angle measurements of the different surface states, ((c) chemical cleaned, (d) ozone-cleaned/activated, (e) ozone-cleaned/inactive, and (f) coated with an APTES SAM ( $t_{PDT} = 24$  h)). The resulting average thickness of the APTES layer obtained via (a) ellipsometry and (b) AFM of  $\sim 0.71$  nm agrees with the literature [122].

The presence and quality of the resulting APTES layer is demonstrated by contact angle analysis, fluorescence microscopy, ellipsometry, surface potential measurements, and atomic force microscopy. For example, ellipsometry data and AFM scans of a patterned

APTES layer reveal a film thickness of  $\sim 0.71$  nm and the comparison of the contact angle for the different surface states (chemical cleaned:  $\Theta = 53.6^\circ$ ; ozone-cleaned/activated:  $\Theta < 20^\circ$ ; ozone-cleaned/inactive:  $\Theta = 47.9^\circ$ ; covered with an APTES SAM:  $\Theta = 63.9^\circ$ ) demonstrate the different states of the surface and reveal that APTES SAMs are obtained via this process (Figure 4.3) [123]. However, the duration of PDT proves to be vital to the success of SAM formation (PDT of 24 h was chosen for the results shown in Figure 4.4). To analyze the role of PDT in more detail, we measure the surface potential for the different states (chemical cleaned, ozone-cleaned/activated, and ozone-cleaned/inactive) and at different durations of PDT, as indicated by the  $\zeta$  symbols in Figure 4.2.

Streaming current measurements are performed to analyze the surface potential. In a first step, the stability of the surface potential is examined by recording the  $\zeta$  potential for a given electrolyte and pH value for a longer duration (typically 6 hours). Figure 4.4 shows typical examples of the time-dependent measurement of the Si/SiO<sub>2</sub> sample for different states using 1 mM of KCl in Milli-Q water at a fixed pH value of 6. The Si/SiO<sub>2</sub> surfaces exhibit stable surface potentials in the chemical cleaned, ozone-cleaned/activated, and ozone-cleaned/inactive, i.e. the  $\zeta$  potential is unaltered during the complete measuring time of 6 hours. However, the potentials are quite different in all states.

After activation treatment, the surface potential shows a significant decrease by  $\sim 45$  mV, i.e. from  $-(18 \pm 0.5)$  mV in the chemical cleaned state to  $-(63 \pm 0.5)$  mV in the ozone-cleaned/activated state. The reduction of the surface potential during the ozone treatment (activation) is caused by the formation of Si-OH silanol groups, which introduce a negative charge at the surface if exposed to the electrolyte. With time, and especially if exposed to a humid environment, these silanol groups undergo a condensation reaction and return to the more stable siloxane configuration Si-O-Si. This process takes several days (Figure 4.1).

The resulting surfaces are then ozone-cleaned/inactive (organic contaminations of the surface are removed) and stable, but no longer activated, and are therefore less likely to bind APTES [124]. The resulting ozone-cleaned/inactive state of the Si/SiO<sub>2</sub> surface possesses a slightly smaller surface potential of  $-(31 \pm 0.5)$  mV and a smaller wetting angle of  $47.9^\circ$  compared to the chemical cleaned state, which most likely indicates that organic contaminations of the chemical cleaned surface are removed by ozone cleaning.

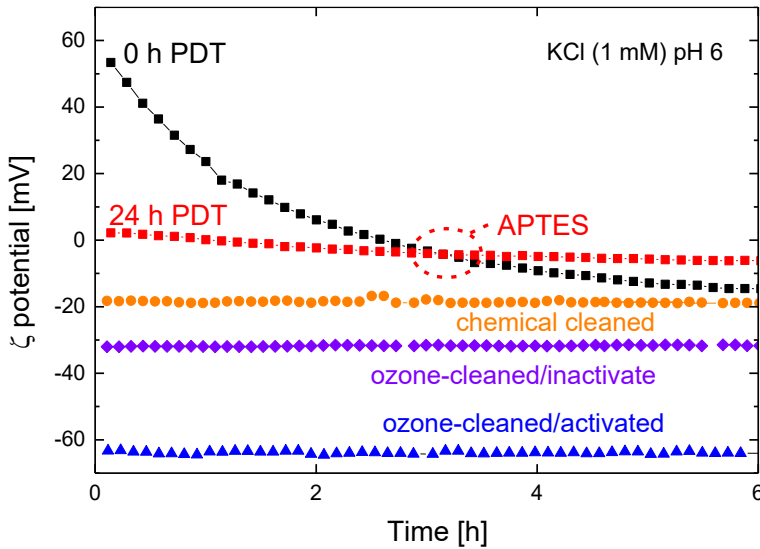


Figure 4.4: Time-dependent measurement of the  $\zeta$  potential for chemical cleaned Si/SiO<sub>2</sub> substrates (orange circles), ozone-cleaned/activated Si/SiO<sub>2</sub> substrates (blue triangles), ozone-cleaned/inactive Si/SiO<sub>2</sub> substrates (purple diamonds), and Si/SiO<sub>2</sub> substrates after APTES deposition, directly after deposition (black squares), and after 24 hours PDT (red squares). All measurements are performed in Milli-Q water with 1mM KCl at pH 6.

In contrast to the chemical cleaned, ozone-cleaned/activated, and an ozone-cleaned/inactive states, the Si/SiO<sub>2</sub> covered with APTES does not show a stable surface potential on the timescale of hours. The  $\zeta$  potential decreases strongly with time (Figure 4.4). Moreover, this decrease depends on the PDT duration. The shorter the PDT duration is, the more pronounced the potential drop is - i.e. it starts at a higher potential and ends at a lower potential for shorter PDT treatments. This is shown in Figure 4.4 for two examples with different PDT durations,  $t_{\text{PDT}} = 0$  h (i.e. measured directly after deposition) and  $t_{\text{PDT}} = 24$  h.

In order to analyze this behavior in more detail, we plotted the starting point (recorded at  $t_{\text{PDT}}$ ) and end point (recorded after  $t_{\text{PDT}}$  plus 24 h exposure to the electrolyte) of the surface potential measurement for APTES-coated samples as a function of PDT time. This plot (Figure 4.5) shows a number of interesting features:

- (i) Generally, there is a clear decrease of the  $\zeta$  potential during the exposure of the sample to the electrolyte.

- (ii) For the samples, which are analyzed directly after termination of the deposition ( $t_{\text{PDT}} \approx 0$ ), the  $\zeta$  potential measured after 24 h exposure to the electrolyte is identical to the  $\zeta$  potential measured for the ozone-cleaned/inactive substrate (solid line in Figure 4.5).
- (iii) With increasing PDT duration, the difference between the  $\zeta$  potential measured at the starting point and end point decreases (from  $\sim 80$  mV to  $\sim 8$  mV for  $t_{\text{PDT}} = 0$  and 112 h, respectively) and the  $\zeta$  potential converges to a value of approximately  $-(6 \pm 2)$  mV.

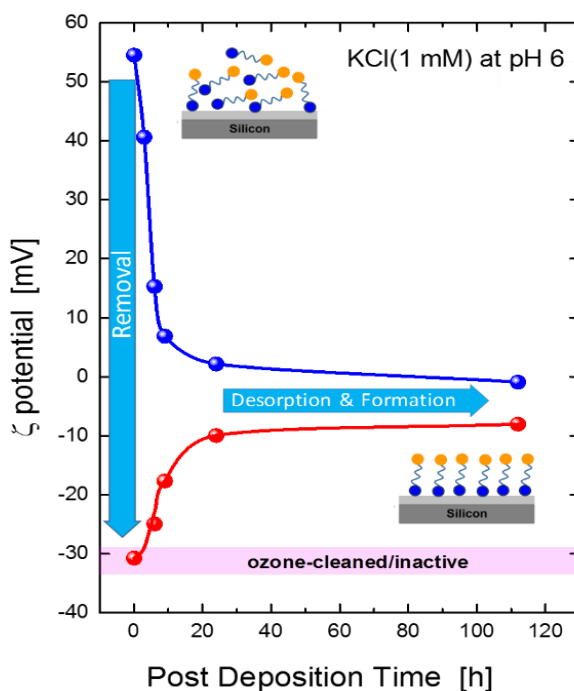


Figure 4.5: Surface potential measurement for APTES-coated Si/SiO<sub>2</sub> substrates as a function of PDT duration, comprising the starting point (blue symbols) and end point (red symbols) of the time-dependent surface potential measurements. All the measurements are performed at pH 6 in 1 mM KCl; the end point is recorded after 24 h exposure to the electrolyte; the purple shaded area represents the surface potential of ozone-cleaned/inactive Si/SiO<sub>2</sub>; the schematics demonstrate the different states of the APTES SAM formation starting with a disordered physisorbed molecular layer for a short PDT to an ordered SAM layer for long PDTs, the blue and orange dots symbolize the APTES head group and amino group, respectively.

These observations are explained by the schematics and arrows in Figure 4.5:

- Exposure to the electrolyte appears to lead to the removal of unbound APTES molecules. The originally high  $\zeta$  potential of the physisorbed (but not chemisorbed) APTES layer reduces over time and, finally, a low  $\zeta$  potential is measured.
- Without PDT, the final  $\zeta$  potential is identical to the  $\zeta$  potential of the ozone-cleaned  $\text{SiO}_2$  surface, thus indicating that nearly all molecules are removed and that hardly any APTES molecules are bound to the  $\text{SiO}_2$  surface.
- With increasing PDT duration, the initial value of the  $\zeta$  potential decreases, indicating that APTES is also removed from the surface during PDT (i.e. desorption into the gas phase). At the same time, the end point ( $\zeta$  potential measured after 24 h in the electrolyte) increases. This indicates that more and more APTES molecules are bound to the  $\text{SiO}_2$  surface, thus forming an APTES SAM during PDT.

The PDT therefore seems to be of vital importance for the formation of APTES SAMs. After PDT of approximately 24 h, we achieve a reasonable APTES SAM. However, a longer PDT duration might lead to an even larger density of APTES molecules in the SAM. Since the complete deposition, including PDT, is performed at room temperature, an increase of the process temperature, for instance during PDT, might accelerate the SAM formation process.

#### 4.1.2 Titration analysis

In a second step, we analyze the pH dependence of the surface charge density for the different states of the substrates, i.e. the chemical cleaned, ozone-cleaned/activated, ozone-cleaned/inactive, and coated (here APTES SAM for 24 h PDT) states. We therefore record the  $\zeta$  potential of the different states as a function of the pH value.

Figure 4.6 shows a set of titration experiments for chemical cleaned  $\text{Si}/\text{SiO}_2$ , ozone-cleaned/activated  $\text{Si}/\text{SiO}_2$ , ozone-cleaned/inactive  $\text{Si}/\text{SiO}_2$ , and  $\text{Si}/\text{SiO}_2$  coated with an APTES SAM obtained after 24 h PDT. In all cases, the titration measurement starts with a 1 mM KCl electrolyte, i.e. at  $\text{pH} \sim 5.5$ , with the pH value being gradually increased or decreased via titration with a basic (50 mM KOH) or acidic (50 mM HCl) electrolyte, respectively.

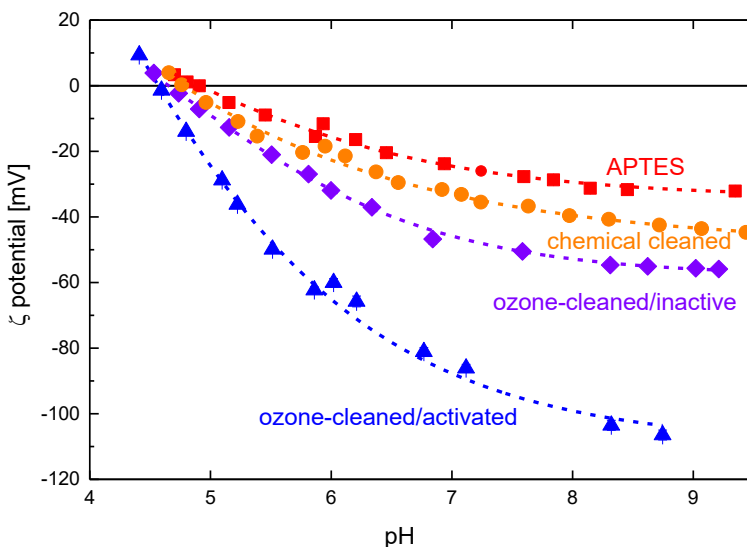


Figure 4.6:  $\zeta$  potential of Si/SiO<sub>2</sub> in the chemical cleaned state (orange circles), ozone-cleaned/activated state (blue triangles), ozone-cleaned/inactive state (purple diamonds), and coated with an APTES SAM with 24 h PDT (red squares) as a function of the pH value for 1 mM KCl electrolyte.

All experiments show the typical pH dependence of the  $\zeta$  potential in the pH regime above 4.5. The  $\zeta$  potential decreases with increasing pH, since a negative surface charge builds up when the sample is exposed to a more basic (higher pH) environment [125]. The pH dependence in this regime can be fitted with an exponential function (dotted lines in Figure 4.6). The absolute values of the  $\zeta$  potential differ for the various states. The lowest  $\zeta$  potential is observed for the ozone-cleaned/activated substrate with the negatively charged Si-OH silanol groups, whereas the highest potential is observed for the APTES layer. The latter is caused by the amino functional group of APTES that reacts with the electrolyte and forms NH<sub>3</sub><sup>+</sup> (ammonium cation) [126]. A repetition of the  $\zeta$  potential measurement after 2 months exposure to the electrolyte demonstrated that the APTES-coated substrate with 24 h PDT is stable.

#### 4.1.3 Evaluation of the electrokinetic charge

Due to the interaction between partial charges (created due to the asymmetric distribution of electrons in chemical bonds) on the surface and ions in the electrolyte, surfaces develop

a net surface charge. This net charge results in a surface potential and therefore the formation of a shielding ion and counterion layer, the electric double layer (EDL). The first layer of adsorbed ions refers to the immobile inner Helmholtz layer, whereas the second layer of non-specifically adsorbed, hydrated counterions represents the mobile outer Helmholtz layer; mobile and immobile layers are separated by the shear plane (inset Figure 4.7).

The  $\zeta$  potential, also known as the electrokinetic potential, describes the charging behavior at the shear plane. This shear plane actually represents the interface between the mobile (liquid) phase and the immobile (solid plus adsorbed ions) phase, which is crucial for most solid-liquid interface applications.

The relation between surface charge and surface potential can be expressed by the Grahame equation [127]. It is derived from the Gouy-Chapman theory by assuming electroneutrality, i.e. the surface charge is counterbalanced by the total charge of the EDL. By means of analogy, it is possible to derive the electrokinetic charge density  $\sigma_{ek}$ , which represents the charge density at the shear plane between the mobile and immobile Helmholtz layers [128]:

$$\sigma_{ek} = \sqrt{8c\epsilon_0\epsilon RT} \sinh\left(\frac{F\zeta}{2RT}\right) \quad (14)$$

Here,  $\epsilon_0$  and  $\epsilon$  represent the vacuum permittivity and dielectric constant of the electrolyte;  $R$ ,  $T$ , and  $F$  are the gas constant, the absolute temperature, and the Faraday constant, respectively; and  $c$  is the solute concentration of the electrolyte. Inserting reasonable values for the permittivity ( $\epsilon = 78.14$ ) [129], we obtain the resulting electrokinetic charge density for the different states (Figure 4.7). Although we use a relatively small concentration of 1 mM KCl, the enhancement of the concentration due to the titration with KOH can be disregarded. Noteworthy, the electrokinetic charge density depends on the concentration of the electrolyte. A larger concentration would lead to an increase of the electrokinetic charge density, since  $\sigma_{ek}$  is almost proportional to  $\sqrt{c}$  (disregarding the small concentration dependence of the  $\zeta$  potential).

The impact of the functional groups - silanol and amino for activation and APTES SAM, respectively - can be evaluated from the difference of the electrokinetic charge density obtained for the respective state (ozone-cleaned/activated or APTES SAM) and the ozone-cleaned/inactive state (Figure 4.7).

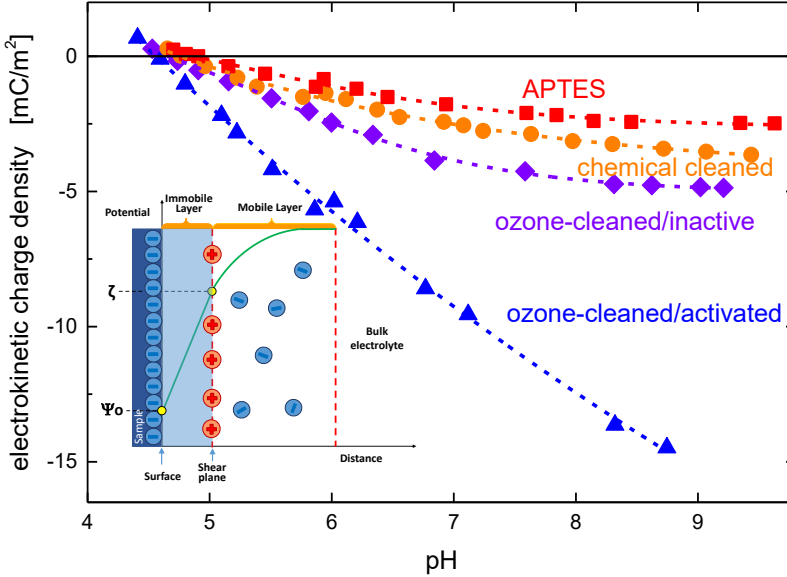


Figure 4.7: Electrokinetic charge density of Si/SiO<sub>2</sub> in the chemical cleaned state (orange circles), ozone-cleaned/activated state (blue triangles), ozone-cleaned/inactive (purple diamonds), and coated with an APTES SAM with 24h PDT (red squares) as a function of the pH value for 1 mM KCl electrolyte using the  $\zeta$  potential shown in Figure 4.6 and eq. (1). The inset shows a sketch of the different layers and charge distribution at the solid–electrolyte interface, uncharged atoms or molecules and ions compensated by counter ions are not shown.

In terms of activation, one in two Si atoms of the SiO<sub>2</sub> surface can be activated and therefore form a silanol functional group (schematic in Figure 4.8a), according to the literature. The resulting density of the silanol group is thus expected to be  $n = 4.6 \text{ nm}^{-2}$  [130]. If we assume that the total change of the electrokinetic charge density,  $\Delta\sigma_{ek,OH}$ , is due to the local changes,  $\Delta q_{FG}$ , resulting from the formation of the silanol function group, which accumulate to

$$n \cdot \Delta q_{FG} = \Delta\sigma_{ek,OH} \quad (15)$$

we can estimate the impact of the individual silanol on the electrokinetic charge density. Figure 4.8a shows the resulting plot of  $\Delta q_{FG}/e$  as a function of the silanol density,  $n$ , for a given pH value of 6. If we assume a reasonable density,  $n \approx 4.6 \text{ nm}^{-2}$ , for the silanol, [122] we obtain an effective charge contribution per OH of approximately -0.45 % of the elementary charge at pH 6 (Figure 4.8a). Evidently, this value also depends on the

electrolyte, especially its concentration (here 1 mM KCl). It increases with electrolyte concentration

Similarly, we can estimate the impact of individual amino groups of the APTES SAM on the electrokinetic charge density. If we assume a similar density of functional groups,  $n = 4.6 \text{ nm}^{-2}$ , in the case of the APTES SAM (i.e. for optimized APTES SAMs, each silanol group is replaced by an APTES molecule), we obtain a positive but roughly 3 times smaller value of  $\Delta q_{\text{FG}}/e \approx 0.18 \%$  for each amino functional group at pH 6 (Figure 4.8a). A larger concentration would again lead to a larger contribution of the APTES molecule to the electrokinetic charge density.

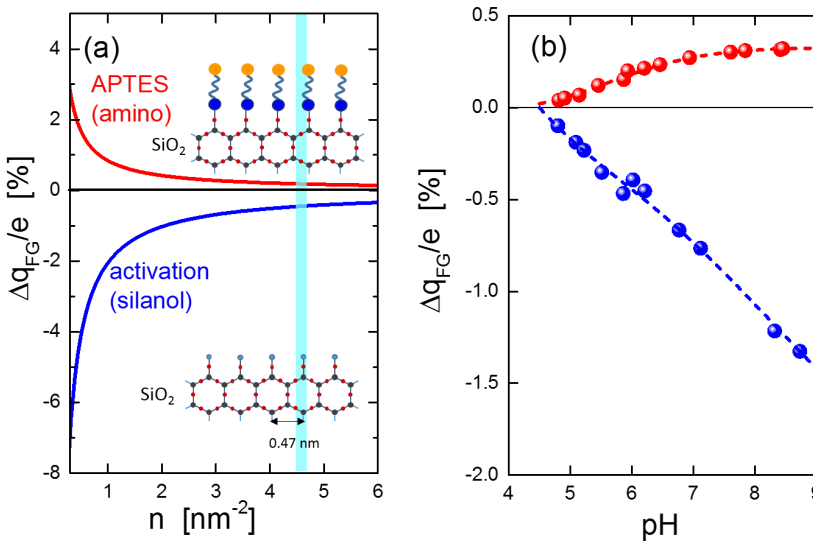


Figure 4.8: Impact of individual silanol (blue) and amino (red) functional groups on the electrokinetic charge density of  $\text{SiO}_2$  for 1mM KCl (a) as a function of their density for pH 6 and (b) as a function of the pH value for a density of  $n = 4.6 \text{ nm}^{-2}$ . The cyan shaded area in (a) depicts the literature value for the expected density  $n = 4.6 \text{ nm}^{-2}$  of functional group [130, 131]; the schematics show the expected structural arrangement of APTES (head group in blue, amino group in orange) and silanol (light blue) on the  $\text{SiO}_2$  surface (hexagonal structure).

If we extend this consideration to other pH values, we actually obtain a near-linear dependence of  $\Delta q_{\text{FG}}$  for both modifications, i.e. silanol group and amino group in the case of activation and APTES SAM, respectively. This is shown in Figure 4.8b for a 1 mM KCl electrolyte. For the negatively charged silanol group,  $\Delta q_{\text{FG}}$  decreases with the pH value, whereas  $\Delta q_{\text{FG}}$  increases with the pH value for the positive amino group. A larger concentration would again lead to a larger contribution of the activation and APTES SAM

to the electrokinetic charge density. A linear extrapolation of the pH dependence of  $\Delta q_{FG}$  to lower pH values indicates a  $pK_a$  value of pH ( $4.4 \pm 0.2$ ) for both modifications of the  $SiO_2$  surface, which is in agreement with the literature [105, 132, 133].

#### 4.1.4 Conclusion

In this section, we analyzed and optimized the growth and properties of self-assembled APTES monolayers deposited from the gas phase onto  $SiO_2$  surfaces. By recording the  $\zeta$  potential and its development after deposition of the molecules, we were able to demonstrate that:

- (i) A post-deposition treatment (PDT) is crucial to the formation of APTES SAMs. We showed how a thick layer of APTES molecules is initially adsorbed at the surface, although the molecules do not bind to the  $SiO_2$  and are thus removed if the film is exposed to an electrolyte. Only if the film is kept in a gaseous environment (preferable at low pressure) do APTES molecules start to bind to the surface and form the SAM layer. Superfluous molecules are removed.
- (ii) In our setup (at room temperature and  $\sim 10^{-5}$  hPa), a PDT duration of at least 24 hours was necessary to achieve a stable and good-quality SAM of APTES on  $SiO_2$ .
- (iii) Furthermore, we analyzed the impact of ozone activation and APTES SAM on the electrochemical properties of the solid–liquid interface by evaluating the electrokinetic charge at the shear plane between the immobile and mobile Helmholtz layers. The electrokinetic charge density is strongly reduced by the activation of the  $SiO_2$  surface (due to the formation of silanol groups), whereas it is enhanced by the APTES SAM (due to the APTES amino group).

The understanding and tailoring of inorganic surfaces via organic self-assembled monolayers, demonstrated for the combination of  $SiO_2$  and APTES, represents first step towards robust and potentially reusable substrate with optimized interfaces for neuroelectronic applications.

## 4.2 Guided neurons growth on patterned functionalized oxides

In this chapter we demonstrate that guided growth of neurons can be achieved by patterned oxide surfaces, which are functionalized with organic molecules. The discussion is divided into three sections:

- (i) In chapter 4.2.1, we demonstrate that silanization with APTES is only possible for some of the examined oxides, whereas no APTES SAM forms on others. As a result, we obtain a large difference in the surface potential as well as functionalization via APTES for the different oxides.
- (ii) In chapter 4.2.2, we show that this difference leads to a large discrepancy in the compatibility with neuronal cell for these functionalized oxides.
- (iii) In chapter 4.2.3, we demonstrate guided cell growth using patterned samples consisting of different oxides with APTES coating.

#### 4.2.1 Functionalization of different oxides with APTES

In this chapter, the surface potential of different oxides and their ability to be functionalized using APTES SAMs are discussed. Four candidates are examined, i.e. SiO<sub>2</sub> terminated Si, and Al<sub>2</sub>O<sub>3</sub>, TiO<sub>2</sub>, and Ta<sub>2</sub>O<sub>5</sub> films on Si/SiO<sub>2</sub>.

The ALD preparation of the films is described in the chapter 3.1.2. The resulting films are examined via X-ray photoelectron spectroscopy (XPS), X-ray diffraction (XRD) and scanning electron microscopy (SEM) in order to control the quality of the films. As an example, the characterization of Ta<sub>2</sub>O<sub>5</sub> films deposited via ALD is discussed below, some of the characterization details are shown in Figure 4.9.

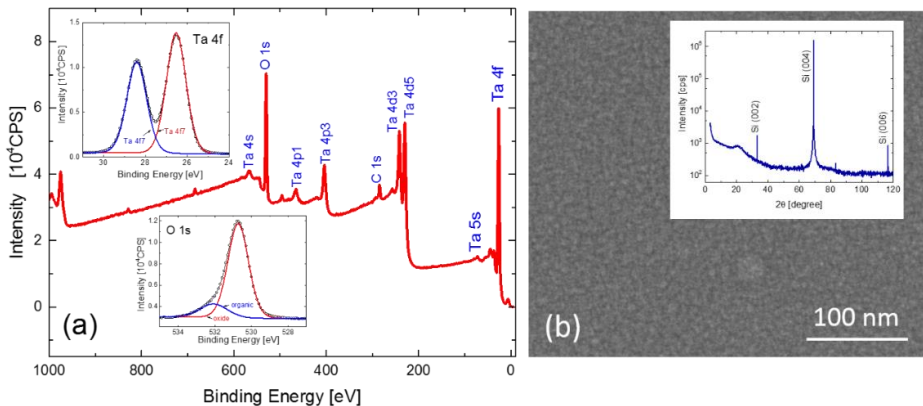


Figure 4.9: (a) XPS spectrum depicting the ALD Ta<sub>2</sub>O<sub>5</sub> specimen. Top insert and bottom insert show detailed XPS spectra scanning of Ta 4f and O 1s, respectively. (b) SEM image of the surface morphology of the ALD Ta<sub>2</sub>O<sub>5</sub>; the insert shows the corresponding XRD Bragg-Brentano pattern.

XPS is used to analyze the surface chemical composition. The complete spectrum (0-1000 eV) in Figure 4.9a demonstrates the presence of Ta, O, and C at the surface. The analysis of the Ta 4f and O1s peaks (inserts in Figure 4.9a) demonstrates the following:

- (i) Only one Ta-O phase is present at the surface.
- (ii) The O/Ta ratio of  $\sim 2.4$  obtained from the fitting of the spectra indicates that this phase is most likely the Ta<sub>2</sub>O<sub>5</sub> phase.
- (iii) Although C 1s signals are unavoidable due to carbon contamination of ex situ prepared samples and XPS chamber components, it can't be excluded that at least parts of the C stems from organic hydrocarbon contaminations with -OH, -C=O, and -COOH groups which might be residues from the ALD precursors. RBS measurements support this interpretation and also show a contamination of  $\sim 7.5$  atm% carbon in the films.

Furthermore, XRD analysis (insert in Figure 4.9b) demonstrates the absence of any regular (crystalline) structure of the Ta<sub>2</sub>O<sub>5</sub> film and according to the SEM image (Figure 4.9b) the film is quite smooth.

In a first experiment we record the  $\zeta$  potential of the different materials for the ozone cleaned surface and for comparison after deposition of APTES (cleaning and APTES deposition are described in chapter 3.1.1). In order to demonstrate the presence or absence of APTES SAMs after APTES deposition, fluorescence microscopy experiments are performed for the different oxides.

Figure 4.10a shows a set of titration experiments for the different oxides in the different states after cleaning and coating with APTES. In all cases, the titration measurement starts at pH  $\approx 5.5$  (1 mM KCl electrolyte), subsequently the pH value is increased incrementally with a basic (50 mM KOH) electrolyte. The titration experiments show the typical pH dependence of the  $\zeta$  potential of oxides in the pH regime above the isoelectric point (i.e. the pH value of  $\zeta = 0$ ). The  $\zeta$  potential decreases with increasing pH for all oxides and seems to saturate at high pH values (e.g. for SiO<sub>2</sub> and Ta<sub>2</sub>O<sub>5</sub>). However, there are two important differences between the different oxides:

- (i) First, there is a significant difference in the height of the  $\zeta$  potential for the different oxides. For example, at physiological conditions (pH  $\approx 7.4$ ),  $\zeta$  potentials of around -22 mV and -62 mV are determined for Al<sub>2</sub>O<sub>3</sub> and Ta<sub>2</sub>O<sub>5</sub>, respectively (Figure 4.10b). This represents a large difference in the surface potential, which should also affect the cell adhesion property of the different oxides.

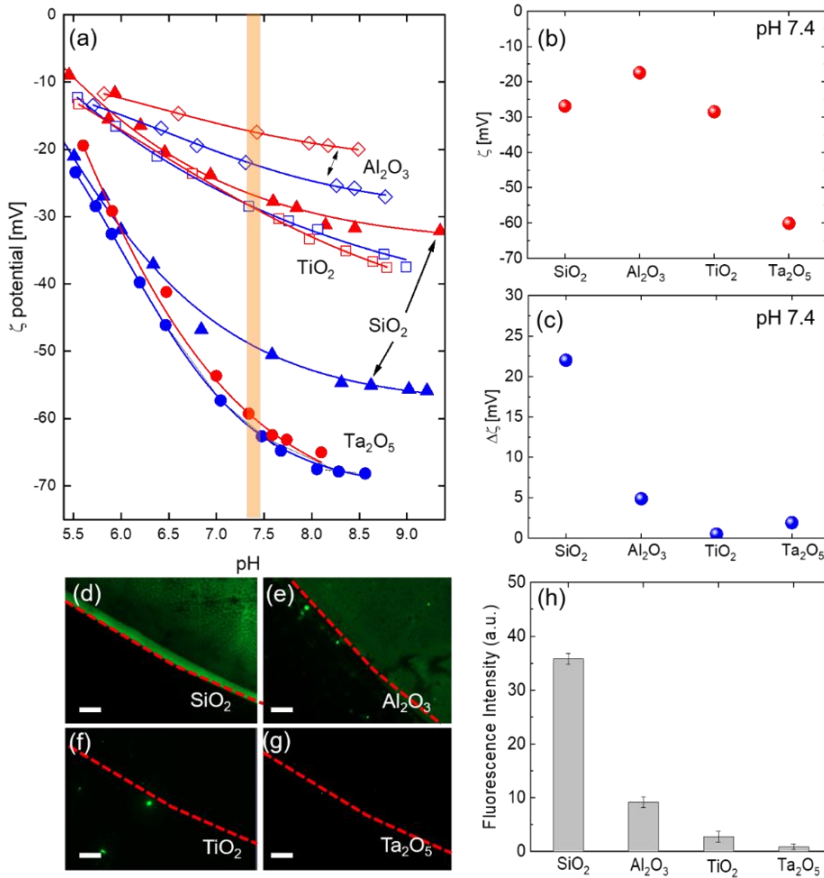


Figure 4.10: (a)  $\zeta$  potential of  $\text{TiO}_2$  (open squares),  $\text{Al}_2\text{O}_3$  (open diamonds),  $\text{Ta}_2\text{O}_5$  (solid circles), and  $\text{Si/SiO}_2$  (solid triangles) in the cleaned state (blue) and coated with an APTES SAM (red), respectively, as a function of pH value for 1 mM KCl electrolyte. The orange shaded area depicts the physiological pH value of 7.4. (b), (c) represent the  $\zeta$  potential (APTES coated) and  $\Delta\zeta$  (difference between the  $\zeta$  potential for APTES coated and cleaned state) for the different oxide films at pH 7.4. (d), (e), (f), (g) present the fluorescence microscopic image of FITC drops on  $\text{SiO}_2$ ,  $\text{Al}_2\text{O}_3$ ,  $\text{TiO}_2$  and  $\text{Ta}_2\text{O}_5$  treated with APTES, respectively. The dashed red lines mark the boarder of the drop separating the FITC covered area (upper part) and the area without FITC (lower part); the scale bar is  $100\mu\text{m}$ . (h) shows a comparison of the resulting FITC fluorescence intensities of APTES on the different oxides surfaces.

- (ii) Second, for some oxides ( $\text{SiO}_2$  and  $\text{Al}_2\text{O}_3$ ) the APTES deposition leads to a clearly visible increase of the  $\zeta$  potential, whereas for the others ( $\text{TiO}_2$  and  $\text{Ta}_2\text{O}_5$ ) no increase of the  $\zeta$  potential is recorded. The largest increase is actually visible for  $\text{SiO}_2$ , where the  $\zeta$  potential at physiological conditions changes from -49 mV to -

27 mV (Figure 4.10). From previous work [100, 115] we know that the enhancement of the surface potential is an indication for the successful deposition of APTES, i.e. the formation of an APTES SAM on the oxide.

In order to demonstrate the presence of APTES SAMs on the oxides, fluorescence experiments were performed. By depositing a drop of FITC on each sample and removing the unbound FITC after some time (chapter 3.3.5), we can visualize the presence of APTES on the oxide, since FITC will only remain at APTES molecules bound to the sample. Figure 4.10d-g show the edge of the drop for SiO<sub>2</sub>, Al<sub>2</sub>O<sub>3</sub>, TiO<sub>2</sub> and Ta<sub>2</sub>O<sub>5</sub>. Whereas the fluorescence signal is clearly visible for SiO<sub>2</sub>, no fluorescence can be observed for Ta<sub>2</sub>O<sub>5</sub>. Similar results are obtained for Al<sub>2</sub>O<sub>3</sub> (fluorescence is visible) and TiO<sub>2</sub> (no fluorescence). This is summarized in Figure 4.10h. Since there is clear correlation between the FITC's fluorescence intensity and the amount of APTES on the oxides [115], this supports the result of the  $\zeta$  potential measurement (compare Figures 4.10c and 4.10h) and leads to the conclusion that an APTES SAM formed on SiO<sub>2</sub> and Al<sub>2</sub>O<sub>3</sub>, but not on Ta<sub>2</sub>O<sub>5</sub> and TiO<sub>2</sub>.

The different properties of the oxides offer opportunities for the envisioned cell experiments. The large difference in the  $\zeta$  potential, and the fact that one oxide can be functionalized with APTES and the other not, especially make SiO<sub>2</sub> and Ta<sub>2</sub>O<sub>5</sub> promising candidates for comparative cell experiments.

#### 4.2.2 Neuronal cell growth on SiO<sub>2</sub> and Ta<sub>2</sub>O<sub>5</sub>

In a second step, we analyze the neuronal cell growth on SiO<sub>2</sub> and Ta<sub>2</sub>O<sub>5</sub> in the different states after cleaning and after APTES deposition. For comparison, BSG reference samples (only chemically cleaned; see experimental section) with and without PLL coating are added.

Figure 4.11 shows cortical neuron cells live/dead density obtained on Ta<sub>2</sub>O<sub>5</sub>, SiO<sub>2</sub>, and the reference samples (BSG) for the different treatments, Figure 4.11b-d show examples of fluorescence images obtained after live/dead staining (see experimental section), whereas in Figure 4.11a the statistics derived from these images (the results of 6 samples were always averaged for the statistics) are presented. The main results of this comparison are as follows:

- (i) Whereas cell cultures on SiO<sub>2</sub> show live cell densities comparable to the reference samples (BSG with and without PLL), the neuron live density on Ta<sub>2</sub>O<sub>5</sub> is significantly lower. Moreover, neurons only tend to form clusters (neurospheres), which will be discussed below, on Ta<sub>2</sub>O<sub>5</sub>.

- (ii) The impact of the APTES deposition on the cells' total density and cells' live density is opposite for  $\text{SiO}_2$  and  $\text{Ta}_2\text{O}_5$ . For  $\text{SiO}_2$ , both densities (total and live density) increase after APTES deposition, whereas the densities decrease in the case of  $\text{Ta}_2\text{O}_5$ .

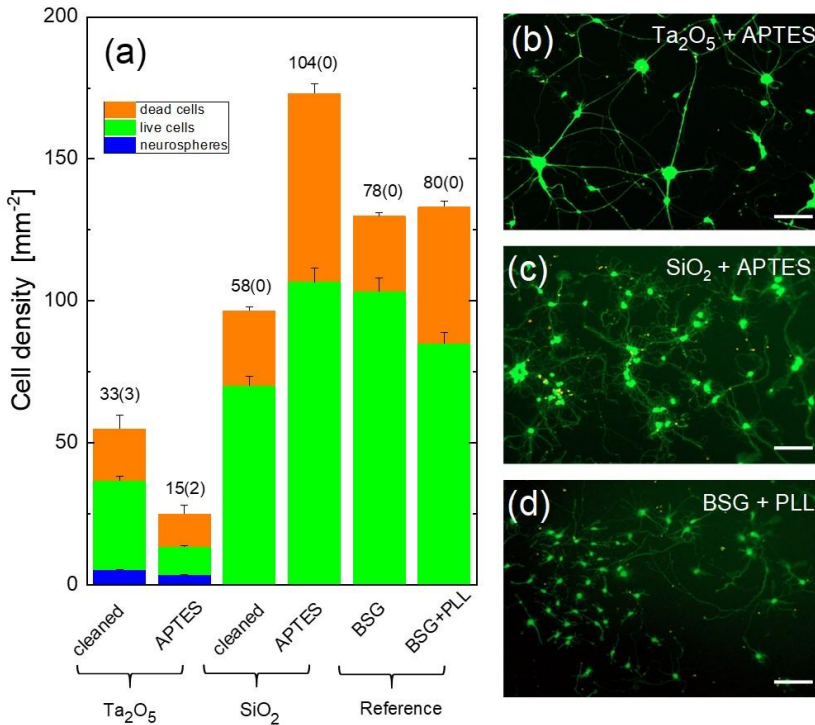


Figure 4.11: (a) Statistics of neurons after DIV 6 of incubation on  $\text{Ta}_2\text{O}_5$  and  $\text{Si}/\text{SiO}_2$  at different states (ozone cleaned and APTES-coated) and on BSG samples with and without PLL. The total number of live cells (green bars), dead cells (orange bars), and neurospheres (blue bars), the number of neurospheres (in brackets) obtained on average over several areas of size  $0.6 \text{ mm}^2$  are added together to form the different columns; for the statistics 6 samples were investigated for each group. (b), (c) and (d) represent fluorescent microscope images of live/dead cell distributions for APTES modified  $\text{Ta}_2\text{O}_5$  and  $\text{SiO}_2$  and BSG treated with PLL, respectively; the scale bar is  $100 \mu\text{m}$ .

These observations demanded further discussion. From Figure 4.10 we know that APTES chemically binds to  $\text{SiO}_2$  but not to  $\text{Ta}_2\text{O}_5$ . Nevertheless, it is known that during the gas

phase deposition, APTES is physisorbed on both oxide surfaces [100]. After deposition the physisorbed molecules will be desorbed. However, this desorption process is a very slow process and can take hours. Therefore, we encounter two different situations, which is supported by the  $\zeta$  potential analyses shown in Figure 4.12:

- in the case of the APTES deposition for  $\text{SiO}_2$ , we expect a layer of chemically bound APTES (SAM) and only a few physically bound molecules, whereas
- in the case of the  $\text{Ta}_2\text{O}_5$ , only physisorbed APTES is present (Figure 4.11), which can easily be removed from the surface.

Therefore for  $\text{SiO}_2$ , the APTES SAM leads to a large increase of the surface potential and thus to a significantly higher total density of cells (i.e. actually close to the seeding cell density used for the preparation (see Figure 4.12a), whereas in the case of  $\text{Ta}_2\text{O}_5$ , the cells will adhere to a physisorbed layer of APTES and therefore can easily be removed from the  $\text{Ta}_2\text{O}_5$  surface. Therefore, we have in one case (APTES chemisorbed SAM) an increase of the cell density and in the other case (physisorbed APTES) a decrease of the cell density.

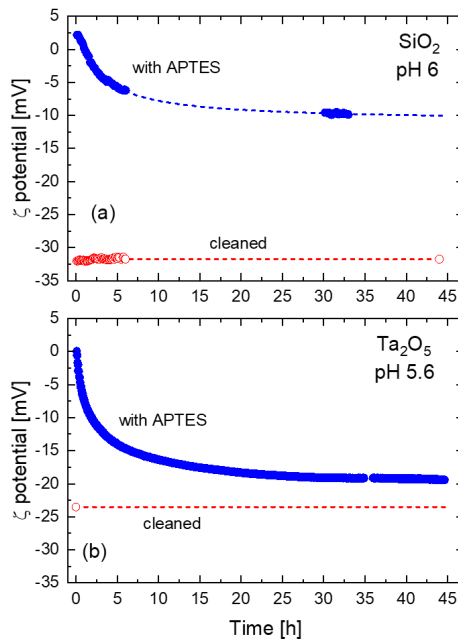
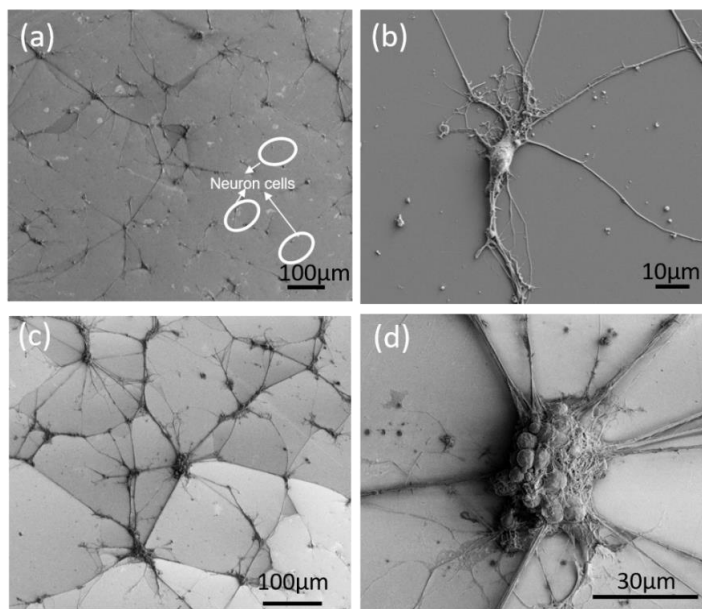


Figure 4.12: Comparison of the development of the  $\zeta$  potential for (a)  $\text{SiO}_2$  and (b)  $\text{Ta}_2\text{O}_5$  after coating with APTES (solid blue symbols) and cleaning (open red symbols) for streaming current measurement in a 1 mM KCl electrolyte at slightly different pH values. The APTES has been deposited at room temperature via gas-phase MLD using the standard parameters and a post-deposition time of 24h. Since the potential doesn't change for the cleaned state, the surface potential is extrapolated from a few data points.

With this explanation, we can also understand the first observation and especially the difference in the cell density shown in the Figure 4.11a. Neglecting the APTES-coated  $\text{Ta}_2\text{O}_5$  where cells might be detached due to the physisorbed APTES coating, the surface potential seems to be correlated with the cell density. The total cell density (live and dead cells) is lowest for cleaned  $\text{Ta}_2\text{O}_5$  ( $\zeta$  (pH 7.4)  $\approx -62$  mV), higher for cleaned  $\text{SiO}_2$  ( $\zeta$  (pH 7.4)  $\approx -49$  mV), and highest for APTES-coated  $\text{SiO}_2$  ( $\zeta$  (pH 7.4)  $\approx -27$  mV). The higher the surface potential, the more cells seem to adhere.



*Figure 4.13: SEM morphology of CPD cortical neuronal cells with different magnification on APTES-coated  $\text{SiO}_2$  (a), (b) and  $\text{Ta}_2\text{O}_5$  (c), (d).*

The formation of neurospheres might also be a result of the extremely negative surface potential of  $\text{Ta}_2\text{O}_5$ , since it is observed in the cases of both the cleaned and the APTES-coated  $\text{Ta}_2\text{O}_5$ . Figure 4.13 shows a comparison of neuron growth on  $\text{SiO}_2$  and  $\text{Ta}_2\text{O}_5$ , both coated with APTES. Whereas healthy individual cells with extended neurites are observed on  $\text{SiO}_2$ , cells tend to form neurospheres of sizes up to  $50 \mu\text{m}$  and tens of somas adhering together on  $\text{Ta}_2\text{O}_5$ . It even seems that most of these neurospheres are detached from the  $\text{Ta}_2\text{O}_5$  and adhere to the top of individual dead cells. Even their axons and dendrites seem to form bundles with poor adhesion to the  $\text{Ta}_2\text{O}_5$  surface, as indicated by lack of branching (Figure 4.13d).

In conclusion to this section, we can state that a large contrast exists for the neuronal cell growth on  $\text{SiO}_2$  and  $\text{Ta}_2\text{O}_5$ . Not only do cells tend to grow in neurospheres with poor

adhesion to the surface on  $\text{Ta}_2\text{O}_5$ , whereas they grow individually on  $\text{SiO}_2$ , but there is also a large difference in the total cell density for cultures on these oxides. For cleaned substrates, there is a twofold difference in cell population on  $\text{SiO}_2$  versus  $\text{Ta}_2\text{O}_5$ . By coating the oxides with APTES, this difference increases to eightfold. The higher the contrast, the more accurate substrate patterns are expected to be transferred to cell network geometries. Moreover, the density of living cells on APTES-coated  $\text{SiO}_2$  is comparable and even slightly higher than that of reference samples prepared by standard cell culture, for instance on PLL-coated BSG. In the following section, the large difference in cell growth on APTES-coated  $\text{SiO}_2$  and  $\text{Ta}_2\text{O}_5$  surfaces is used to demonstrate guided cell growth.

#### 4.2.3 Guided cell growth on patterned oxides

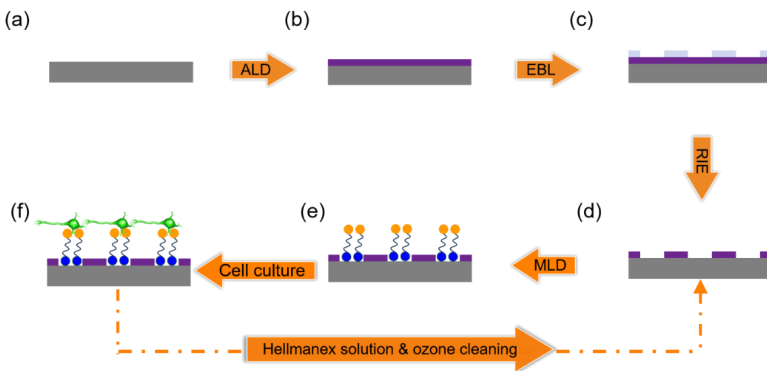


*Figure 4.14: Schematic of substrate preparation process, MLD modification and cell culture for the guided neuron growth: (a)  $\text{SiO}_2$ -terminated Si substrate, (b) ALD of  $\text{Ta}_2\text{O}_5$ , (c) e-beam lithography, (d) reactive ion etching in order to partially remove the ALD layer, (e) MLD of APTES forming SAMs on  $\text{SiO}_2$  surfaces and a physisorbed layer on  $\text{Ta}_2\text{O}_5$ , and (f) cortical neuron cell culture. After inspection and analysis, the cell culture can be removed with Hellmanex solution and after ozone-assisted removal of the remaining organic molecules, the process can be repeated starting with the MLD process (dashed-dotted line).*

In the following we use the large cell density contrast of neuron growth on the APTES SAM-coated  $\text{SiO}_2$  and  $\text{Ta}_2\text{O}_5$  to achieve guided cell growth. The schematic in Figure 4.14 illustrates the different preparation steps (chapter 3.2.2). The preparation of the patterned  $\text{SiO}_2$ - $\text{Ta}_2\text{O}_5$  oxide substrate starts with a 90 nm  $\text{SiO}_2$  terminated Si substrate, which is coated with a 30 nm thick ALD  $\text{Ta}_2\text{O}_5$  layer (Figure 4.14a and b). Using EBL and RIE, we generate the desired oxide pattern on the sample. As such, the sample represents a robust and reusable substrate for the subsequent deposition of molecules and cell culture. The

deposition of APTES is done in the usual way (chapter 3.1.1) starting with an ozone activation of 3 min, followed by the actual gas phase deposition of the molecules (10 min, 0.1 hPa, vapor pressure) and finalized by a 24 h post-deposition treatment in a vacuum [100]. The neuron cell culture starts directly after the MLD preparation according to the procedure given in the experimental section, once again using a cell seeding concentration of approximately  $28.6 \text{ k/cm}^2$ .

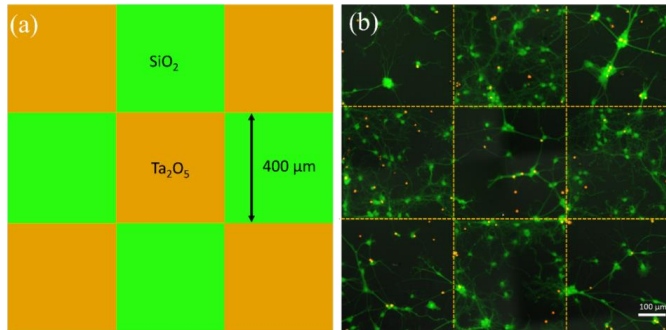


Figure 4.15: (a) Schematic of a “checkboard” structure patterned from  $\text{SiO}_2$  (green)- $\text{Ta}_2\text{O}_5$  (orange), the size of the squares is  $400 \mu\text{m}$ ; (b) fluorescent microscope images of cortical neuron cells forming networks inside  $\text{SiO}_2$  squares, whereas neurospheres are mainly seen on  $\text{Ta}_2\text{O}_5$  at DIV 6 of incubation.

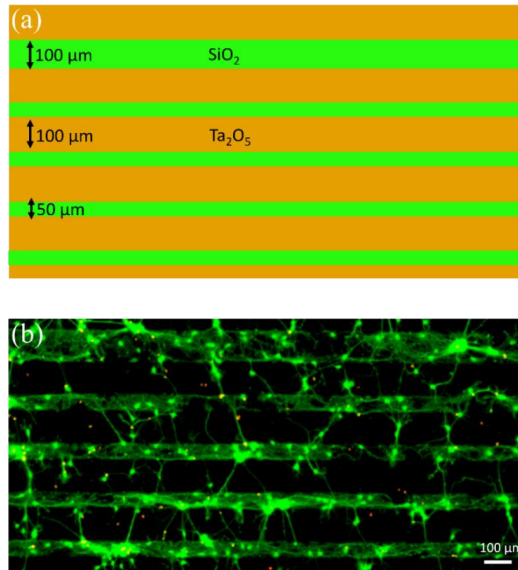


Figure 4.16: (a) Schematic of a larger strip structure patterned from  $\text{SiO}_2$  (green)- $\text{Ta}_2\text{O}_5$  (orange); the size of the  $\text{SiO}_2$  strips are  $100/50 \mu\text{m}$  and separated by  $100 \mu\text{m}$   $\text{Ta}_2\text{O}_5$  strips. (b) Regular neuron cells grow within the  $\text{SiO}_2$  strips separated by  $\text{Ta}_2\text{O}_5$ .

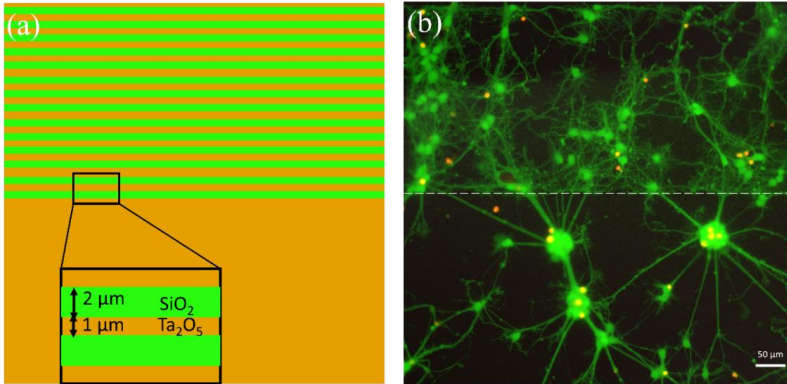


Figure 4.17: (a) Schematic of a strip structure patterned from  $\text{SiO}_2$  (green)- $\text{Ta}_2\text{O}_5$  (orange), the size of the  $\text{SiO}_2$  strip is  $2\ \mu\text{m}$  and separated by  $1\ \mu\text{m}$   $\text{Ta}_2\text{O}_5$  strips. (b) Fluorescent microscope images of cortical neuron cells forming networks inside the  $\text{SiO}_2$ - $\text{Ta}_2\text{O}_5$  patterned structures, whereas large neurospheres are forming on the  $\text{Ta}_2\text{O}_5$  part (below white dashed line) at DIV 6 of incubation.

For this primary test we chose three relatively simple structures:

- (i) larger  $\text{SiO}_2$  areas ( $400\ \mu\text{m} \times 400\ \mu\text{m}$  squares) surrounded by  $\text{Ta}_2\text{O}_5$  (Figure 4.15),
- (ii) large  $\text{SiO}_2$  strips (width of  $50\ \mu\text{m}$  or  $100\ \mu\text{m}$ ) surrounded by  $\text{Ta}_2\text{O}_5$  (Figure 4.16),
- (iii) small  $\text{SiO}_2$  strips (width of  $2\ \mu\text{m}$ ) separated by  $1\ \mu\text{m}$ -wide stripes of  $\text{Ta}_2\text{O}_5$  (Figure 4.17).

All patterns lead to a guided neuron growth behavior and show a growth morphology similar to that demonstrated in the previous section. Moreover, the neuron cell culture can be repeatedly prepared according to the scheme shown in Figure 4.15 leading a reproducible guided growth behavior similar to those shown in the following Figures 4.16 and 4.17.

- On  $\text{SiO}_2$  we observe a higher density of individual neurons, no neurospheres, and a high density of neurites.
- Whereas a much lower density of neurons, mainly neurospheres, bundled axons and a low density of dendrites are present on  $\text{Ta}_2\text{O}_5$  areas (Figure 4.16).
- Interestingly, the third structure in Figure 4.17, which consists of a series (137) of  $2\ \mu\text{m}$ -wide  $\text{SiO}_2$  stripes disrupted by  $1\ \mu\text{m}$   $\text{Ta}_2\text{O}_5$ , also behaves similarly to the plain  $\text{SiO}_2$  areas in Figure 4.11. It seems that the tiny  $\text{Ta}_2\text{O}_5$  disruptions do not affect the neuron growth. Not even the growth direction of the neurites seems to be affected by this  $\text{Ta}_2\text{O}_5$

structure size. The growth is at first glance identical to that of the larger  $\text{SiO}_2$  areas which agrees with observations in the literature [134].

- However, in this work we only tried a very small spacing as a first test. More work on different designs (e.g. variations of  $\text{SiO}_2$  linewidth and  $\text{Ta}_2\text{O}_5$  spacing) would be necessary to find out up to which distance neurons are capable to span their surrounding in this system and whether a directed growth of the neurites is possible with this type of patterning.

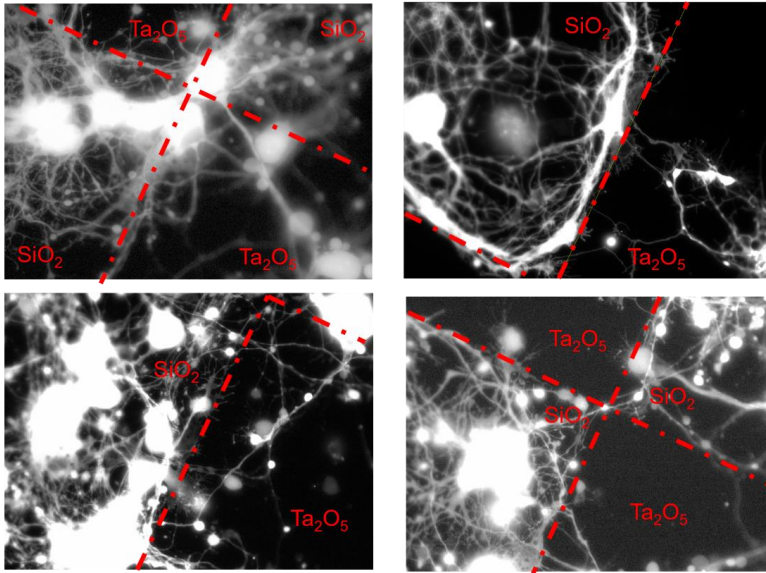


*Figure 4.18: Typical examples of the chosen areas on the  $\text{SiO}_2$  and  $\text{Ta}_2\text{O}_5$  patterned sample showing the neuronal morphology on  $\text{SiO}_2$  versus  $\text{Ta}_2\text{O}_5$ .*

In order to verify the different growth behaviors on  $\text{SiO}_2$  and  $\text{Ta}_2\text{O}_5$ , we analyzed the amount of surface coverage with neurites and growth cones, which can be taken as a measure for the growth activity of the neurons. The amount of neurite and growth cone covered surface is obtained from fluorescence images. By converting the images into gray scale images with adequate contrast, the substrate turns black, soma and neurite bundles become white, and the neurites and their growth cones are gray (Figure 4.18). The amount of gray pixels can then be taken as a measure for the amount of neurites and their growth cones.

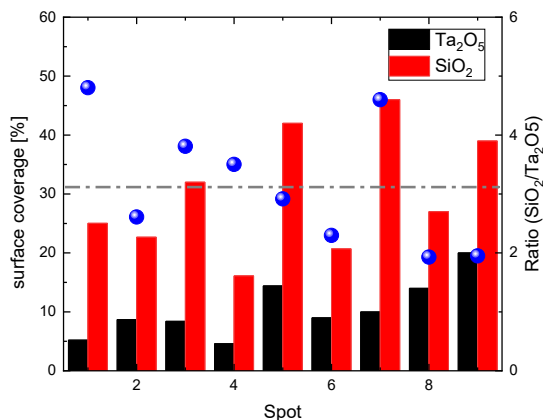


Figure 4.19: Neurite and growth cone surface coverage for nine different spots (size  $1.5 \times 10^4 \mu\text{m}^2$ ) on the patterned sample with similar areas of APTES-coated SiO<sub>2</sub> and Ta<sub>2</sub>O<sub>5</sub>. Red and black bars mark the respective surface coverage on SiO<sub>2</sub> and Ta<sub>2</sub>O<sub>5</sub>, the blue dots represent the ratio of the coverages of these two for the respective spots.

Figure 4.19 shows the resulting percentage of the surface covered by dendrites and growth cones for different positions on the patterned substrate. The positions are chosen arbitrarily at borders between SiO<sub>2</sub> and Ta<sub>2</sub>O<sub>5</sub> and an area of  $1.5 \times 10^4 \mu\text{m}^2$  is examined, which includes similar regions on SiO<sub>2</sub> and Ta<sub>2</sub>O<sub>5</sub>. Although the surface coverage varies for the different positions, it is always significantly higher for the SiO<sub>2</sub> area compared to the adjacent Ta<sub>2</sub>O<sub>5</sub> area. For SiO<sub>2</sub> it ranges from ~15 % to 45 %, whereas it is 5 % to 20 % for Ta<sub>2</sub>O<sub>5</sub>. On average the coverage with dendrites and growth cones is approximately 3.2 times larger for SiO<sub>2</sub> compared to Ta<sub>2</sub>O<sub>5</sub>. Although this number is smaller than the cell density contrast on plain APTES-coated SiO<sub>2</sub> and Ta<sub>2</sub>O<sub>5</sub> surfaces, it demonstrates that a preferential maturation of neurons on SiO<sub>2</sub> area (i.e. guided growth) is also present on patterned SiO<sub>2</sub>-Ta<sub>2</sub>O<sub>5</sub> surfaces.

#### 4.2.4 Conclusion

In this section, we demonstrated that neuronal cell growth can be guided on a substrate by the use of different oxides, which are additionally functionalized with organic molecules.

- (i) We demonstrated that the surface properties of the different oxides themselves are already quite different. For instance, at physiological conditions the  $\zeta$  potential ranges from approximately -62 mV (Ta<sub>2</sub>O<sub>5</sub>) to -49 mV (SiO<sub>2</sub>) or -22 mV (Al<sub>2</sub>O<sub>3</sub>).

- (ii) The oxide surface can be further modified by an additional functionalization with APTES layers. Only physisorbed layers (no chemical binding) can be achieved for some oxides (e.g. Ta<sub>2</sub>O<sub>5</sub>, TiO<sub>2</sub>), whereas APTES SAMs form on other oxides (e.g. SiO<sub>2</sub>, Al<sub>2</sub>O<sub>3</sub>). Not only does this affect the  $\zeta$  potential (e.g. the  $\zeta$  potential at physiological conditions increases from -49 mV to -27 mV on SiO<sub>2</sub>, whereas it is unaltered for Ta<sub>2</sub>O<sub>5</sub>), it also affects the neuronal cell growth. The already high cell density on SiO<sub>2</sub> increases by the chemically bound APTES SAM, whereas the already low cell density on Ta<sub>2</sub>O<sub>5</sub> is even further reduced by the physisorbed APTES layer.
- (iii) As a result we find a large difference in cell density (ratio of ~8) when comparing neuron cultures on SiO<sub>2</sub> and Ta<sub>2</sub>O<sub>5</sub>, both coated with APTES.
- (iv) Furthermore, neurons form the typical networks on SiO<sub>2</sub>, whereas they tend to cluster to form neurospheres on Ta<sub>2</sub>O<sub>5</sub>.
- (v) We utilized the large contrast in cell growth to achieve guided cell growth on reusable robust substrates. Using patterned Ta<sub>2</sub>O<sub>5</sub> layers on SiO<sub>2</sub> substrates functionalized with APTES, the large difference in cell density and growth morphology is also visible for the patterned oxides. For example, on average ~3.2 times larger areas covered with neurites and growth cones are observed on SiO<sub>2</sub> areas compared to Ta<sub>2</sub>O<sub>5</sub> areas.
- (vi) Finally, cell cultures and molecular layers can easily be removed and the cell experiment can be repeated after functionalization with the molecules, which makes this a robust substrate for cell experiments.

The general understanding and tailoring of inorganic surfaces via organic SAMs, demonstrated in this chapter for the combination of SiO<sub>2</sub>, Ta<sub>2</sub>O<sub>5</sub> and APTES, turned out to be a successful method to achieve guided cell growth on robust substrates for bioelectronics applications.

### 4.3 Cell-chip coupling on ALD passivated MEAs

In chapter 4.2 we demonstrated the guided growth of neuronal cells on patterned SiO<sub>2</sub>-Ta<sub>2</sub>O<sub>5</sub> structures. In a next step we try to add Pt metal electrodes, to form multi electrode arrays (MEAs), which could be used simultaneously with the patterned SiO<sub>2</sub>-Ta<sub>2</sub>O<sub>5</sub> structure to obtain guided cell growth and *in vitro* extracellular recording. This would represent another step towards robust neuroelectronics. This chapter is divided into the following steps:

- (i) Firstly (chapter 4.3.1), the electronic properties of the ALD oxide based MEAs are analyzed and compared with the commonly (in-house) used MEAs based on polyimide (PI).
- (ii) Secondly (chapter 4.3.2), HL-1 cell cultures are grown on the PI and ALD based MEAs. By analyzing the electronic signal, signal-noise ratio, and signal propagation of the HL-1 cells, the principle operation and cell chip communication of the novel MEAs is demonstrated.
- (iii) Finally (chapter 4.3.3), we try to demonstrate a guided neuronal growth on the novel ALD MEAs. Unfortunately, the chosen design (especially the size of channels for the growth of neurons) turned out to be too small to allow a dense network of neurons to mature. Therefore, we could not demonstrate the envisioned signal processing for neurons in the chosen patterns.

#### 4.3.1 Development and characterization of MEAs

The main criteria that can be used to design and characterize MEAs are:

- (i) *Impedance of the sensing electrodes*: Generally, it should be small to achieve a large signal transfer of the action potential. One way to minimize the impedance is to enlarge the effective area of the electrodes. However, in order to obtain a good spatial resolution, the electrodes should not be too large. Moreover, in order to measure single cell signals, electrodes should be of the size of an individual neuron, i.e. typically around 20  $\mu\text{m}$  in diameter.
- (ii) *Capacitive coupling of the feedlines*: In order to avoid cross-talk between the signaling line and other electrodes, a passivation layer is necessary which covers the feedlines and minimizes the parasitic capacitive coupling between the lines. In order to get a sufficient passivation, the layer has to be thick enough, free of pinholes, and possess a small enough permittivity.

The combinations of these two factors would lead to a good cell-chip coupling and a small crosstalk.

Figure 4.20a shows the inner part of our standard, in-house used PI MEA. All feedlines (width:  $28\ \mu\text{m}$ ; material: Pt) are passivated by a  $3\ \mu\text{m}$  thick PI layer ( $\epsilon_r \approx 4$ ) and terminate in individual electrodes, which are defined by an opening in the PI layer of  $24\ \mu\text{m}$  in diameter (Figure 4.20b), which is similar to the size of individual neurons.

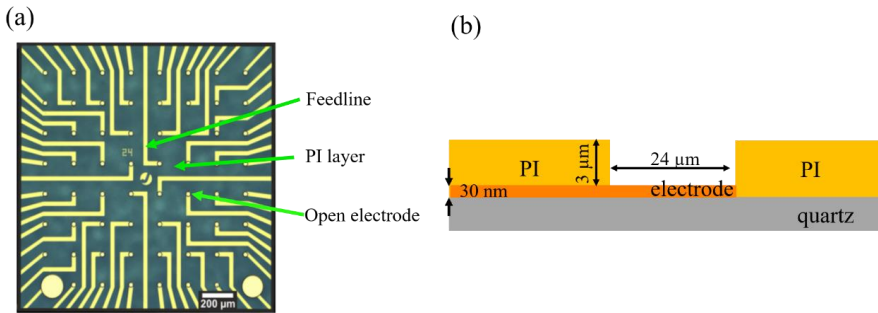


Figure 4.20: (a) Microscope image of a PI based standard MEA that is widely used in our institute. (b) Schematic of the cross section of the PI MEA with the most important design parameters. Figure (a) adapted from [104].

Based on this design and in order to allow a reliable comparison of the different types of MEAs, similar sizes of electrodes and feedlines are chosen for the new ALD based MEAs. However, a much thinner passivation layer (ALD oxide layer of  $\text{Al}_2\text{O}_3$ ,  $\text{TiO}_2$  or  $\text{Ta}_2\text{O}_5$ ) of  $30\ \text{nm}$  thickness is chosen. Moreover, these layers possess a permittivity which is larger than that of PI and holes (e.g. pinholes) cannot be excluded. Furthermore, openings between adjacent electrodes are patterned into the passivation layer down to the  $\text{SiO}_2$ , which are intended to allow the neurons to form networks within the opened area, whereas on the part of the ALD layer, no or hardly any network formation should take place. Different neuronal logic circuits are mimicked by these patterns (Figure 4.21).

The fabrication of the different ALD MEAs for the guided growth and signal recording experiments is based on CMOS technology. All of the preparation steps are carried out in the clean room (ISO-4) of the Helmholtz Nanoelectronic Facility (HNF). The fabrication process includes two EBL steps. In the first step the Pt electrodes are produced by lithography (EBL), Pt evaporation ( $30\ \text{nm}$ ) and successive lift off. Then a  $30\ \text{nm}$  thick ALD insulating layer of  $\text{Al}_2\text{O}_3$ ,  $\text{TiO}_2$  or  $\text{Ta}_2\text{O}_5$  is deposited onto the complete chip. Performing the next round of EBL combined with RIE, the electrodes as well as the channels for the cell growth between adjacent electrodes are opened. In this work, neuronal logic circuits (diverging circuit, converging circuit, reverberating circuit, and parallel after-discharge

circuit) are designed to mimic real logic neuroelectronic structures. In the end the samples are still transparent, so they can be used to monitor the cell cultures in long term experiments.

An example of the real structures and their corresponding schematics in the Autocad design is shown in Figure 4.22. Figure 4.22b shows a schematic cross section of electrode and feedline of the ALD MEA. The electrode size is  $24\ \mu\text{m} \times 24\ \mu\text{m}$ , the thickness of the Pt layer (electrode and feedline) as well as the passivation layer is 30 nm.

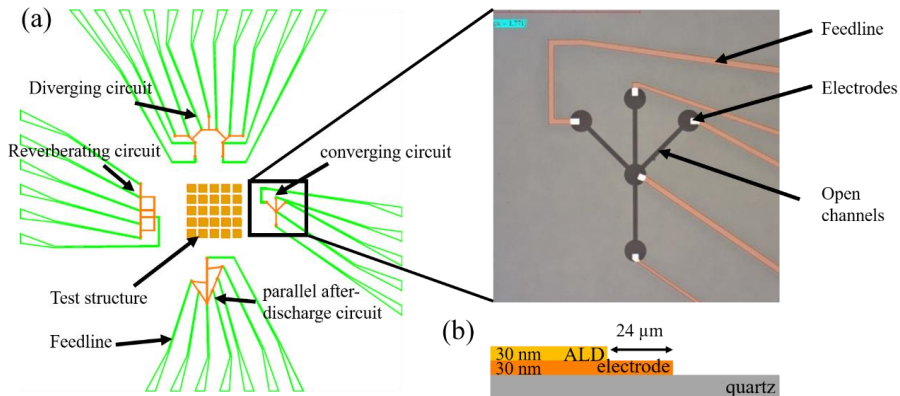


Figure 4.21: (a) Autocad design and microscope image (different logical circuits) of the ALD MEAs. (b) Schematic of the cross section of the electrode and feedline of the ALD MEA in the direction of the channel for the neurons growth.

Table 3. Different parameters of the PI and ALD MEAs.  $A_e$  represents the size of the opening electrodes,  $w$  is the width of the feedline,  $d$  is the thickness of the passivation layer and  $\epsilon_r$  is the estimated permittivity of the passivation layer.

	$A_e(\text{mm}^2)$	$w(\mu\text{m})$	$d(\mu\text{m})$	$\epsilon_r$
PI	452	28	3	4
ALD	576	24	0.03	6-10

The important parameters for the design and properties are listed in Table 3. According to the literature, the permittivities of perfect and crystalline  $\text{Al}_2\text{O}_3$ ,  $\text{TiO}_2$  and  $\text{Ta}_2\text{O}_5$  are 8, 47 and 25 respectively [135-137]. However, our ALD oxides have no crystalline structure (see for example Figure 4.9) which is a precondition for a large polarization. Our non-crystalline films should therefore show the standard permittivity of oxides, which should be in the range of 6-10.

For the main electronic test of the MEAs we used impedance spectroscopy measurements with a signal amplitude of 100 mV and a frequency range (instrument limitation) from 24 Hz to 3 MHz (note: frequency range of the brainwaves  $\sim 0.5\text{-}35$  Hz and APs  $\sim 3\text{-}1000$ Hz). For these experiments a glass ring with an inner diameter of 17.8 mm is glued on top of the MEA via PMDS. Adjacent electrodes are chosen for stimulation and recording (inset of Figure 4.23). The circuit can be represented by two identical impedances,  $Z$ , connected in series:

$$Z_{total} = \frac{Z}{2} \quad (15)$$

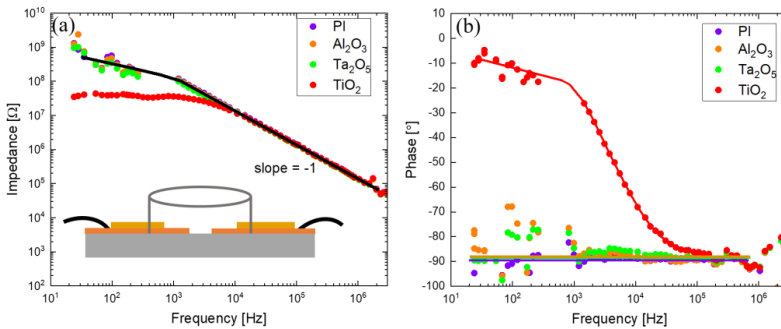


Figure 4.22: Bode plots of the impedance of the open circuit without electrolyte representing the impedance (a) and phase (b) versus frequency. The insert schematically presents the circuit used for the open test.

Let's start with a simple circuit test of the setup without electrolyte (Figure 4.22). In this test, PI, Ta<sub>2</sub>O<sub>5</sub> and Al<sub>2</sub>O<sub>3</sub> MEAs show a similar behavior. In all cases a typical capacitor behavior is observed with the characteristic slope of -1 of the impedance vs. frequency plot (Figure 4.22a) as well as the constant phase of around -90° (Figure 4.22b). Only the TiO<sub>2</sub> MEA shows a combination of resistor and capacitor behavior, which might be attributed to the conductance of this oxide. In fact, it is known that under certain conditions TiO<sub>2</sub> behaves like a p-doped semiconductor [138]. Nevertheless, its impedance is still very high even at low frequencies, which indicates that it might still be a reasonable isolator.

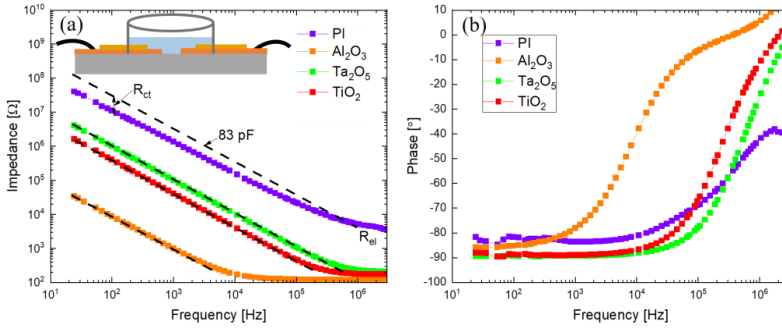


Figure 4.23: Bode plot of the impedance of the different MEAs with 1M KCl electrolyte showing the impedance (a) and phase (b) as function of frequency. The insert schematically presents the circuit which is now covered with electrolyte. The black dashed lines represent the fit with a single capacitor according to equation (16). The perfect agreement between experiment and theory obtained for the ALD MEA demonstrates the capacitive character of the electronic coupling. For PI, the fit (note, that the fit has to be fixed to the highest possible frequency) is steeper compared to the experimental values. This is indicative for an additional conductive contribution in this case. This is also visible in the low frequency value of the phase, which is  $> -90^\circ$ .

In the second test, the impedance of all MEAs embedded in 1 M KCl electrolyte is analyzed to mimic the situation of cell culture medium showing:

- All the MEAs show a capacitor behavior at the low frequencies only at high frequencies the electrolyte resistance takes over (Figure 4.23a and b). The PI MEA plot presents the largest impedance, whereas the  $\text{Ta}_2\text{O}_5$  and  $\text{TiO}_2$  MEAs show a similar behavior, the  $\text{Al}_2\text{O}_3$  MEA shows a low impedance, considering also the correspond unusual phase plot, we assume that the  $\text{Al}_2\text{O}_3$  layer is leaky.
- Nevertheless, in the low frequency regime which is important for electronic cell signal recording, all MEAs show a phase of around  $90^\circ$ . Therefore, it is reasonable to analyze the experimental data in the linear low-frequency part of the double logarithmic impedance plot in Figure 4.23a via:

$$C_m \cong \frac{1}{\omega Z} \quad (16)$$

Since both electrodes (plus feedlines) should be identical, the resulting capacitance  $C_{\text{exp}}$  of the individual contact should be:

$$C_{exp} = 2C_m \cong \frac{2}{\omega Z} \quad (17)$$

The experimentally determined capacitance is listed in Table 4 below, the resulting fit is added in Figure 4.23 (dashed lines). The ALD MEAs show a perfect agreement between fit and experimental value of  $|Z|$  which is an indication for the pure capacitive behavior of the impedance. Only for the PI MEA, fit and experimental value slightly disagree. This is an indication, that additionally to the capacitive coupling, a conductive contribution is present. This will be discussed below.

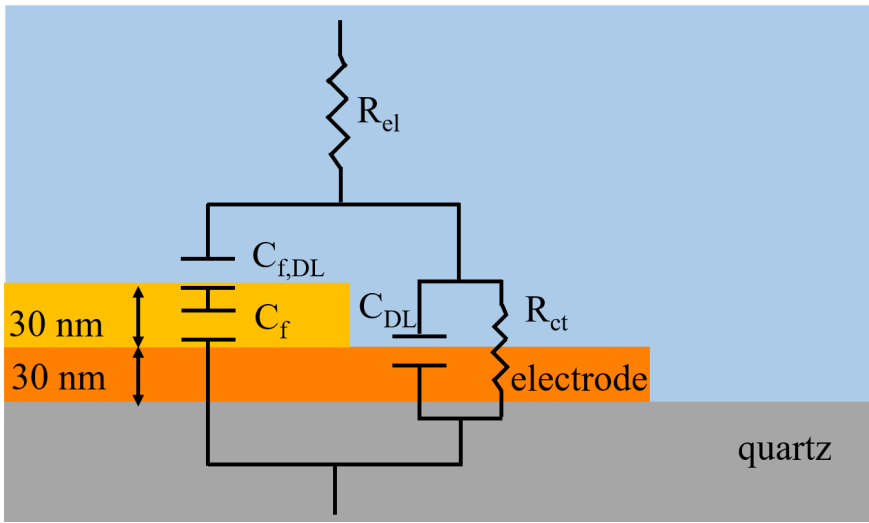


Figure 4.24: Schematic of the electrode-electrolyte interface and the corresponding circuit which contains an electrolyte resistance  $R_{el}$ , two capacitors  $C_{f,DL}$  of the immobile layer on the passivation and  $C_f$  of the passivation layer, and the  $C_{DL}$  in parallel with  $R_{ct}$ .

If we take a closer look at the electronic circuit of this experiment (Figure 4.24), the impedance does not only consist of the contribution of the open electrodes, but also the feedlines covered by the liquid should be taken into consideration. Whereas the impedance of the electrode can be approximated by a parallel arranged capacitance  $C_{DL}$  and charge transfer resistance  $R_{ct}$  of the Helmholtz layer, the impedance of the feedline can be understood as a serial arrangement of the capacitance  $C_f$  of the passivation layer and the capacitance  $C_{f,DL}$  of the Helmholtz layer on top of the passivation layer (Figure 4.24). All individual capacitors are parallel plate capacitors with:

$$C_{theory} = \frac{\epsilon_0 \epsilon_r}{d} A \quad (18)$$

where  $\epsilon_0$  is the vacuum permittivity and  $\epsilon_r$ ,  $d$ ,  $A$  represent the permittivity, thickness and

area of the respective component. By inserting the geometrical data and estimates for the permittivity, we obtain theoretical values for the resulting capacitances and, thus, electronic coupling of the MEAs to the electrolyte.

*Table 4. Calculated and measured capacities for different passivation layers based on the areas of the electrodes (PI:  $452 \mu\text{m}^2$ ; ALD:  $576 \mu\text{m}^2$ ) and feedline (PI:  $0.73 \text{mm}^2$ ; ALD:  $0.79 \text{mm}^2$ ), thickness (PI:  $\sim 3\mu\text{m}$ ; ALD:  $\sim 30\text{nm}$ ) and permittivity (PI:  $\sim 4$ ; ALD: 8 (estimated)) of the passivation layer, permittivity (7.5) and thickness (0.4 nm) of the Helmholtz layer [139].  $C_f$ ,  $C_{f,DL}$  and  $C_{DL}$  represent the capacitance of passivation layer, the capacitance of the Helmholtz layer on top of the passivation layer and the capacitance of the Helmholtz layer on top of electrode,  $A_f$  and  $A_e$  are the areas of the feedline and electrode, respectively.*

	theory				experiment	sensitivity		
	$C_f$ (pF)	$C_{f,DL}$ (pF)	$C_{DL}$ (pF)	$C_{total}$ (pF)	$C_{exp}$ (pF)	$C_f/A_f$ (F/m <sup>2</sup> )	$C_{DL}/A_e$ (F/m <sup>2</sup> )	$\frac{C_{DL}/A_e}{C_f/A_f}$
PI	8.6	$1.2 \times 10^5$	75	83	200	$1.2 \times 10^{-5}$	0.16	13000
TiO <sub>2</sub>	1900	$1.3 \times 10^5$	95	1995	7600	$1.3 \times 10^{-2}$	0.16	12
Al <sub>2</sub> O <sub>3</sub>	1900	$1.3 \times 10^5$	95	1995	320000	$1.3 \times 10^{-2}$	0.16	12
Ta <sub>2</sub> O <sub>5</sub>	1900	$1.3 \times 10^5$	95	1995	3100	$1.3 \times 10^{-2}$	0.16	12

The resulting experimental values (equation 17) and theoretical values (equation 18) are summarized in Table 4. It shows the following features:

- (i) The Helmholtz layer capacitance ( $C_{f,DL}$ ) of the feedline is always much larger than the feedline capacitance ( $C_f$ ) itself. Since these two capacitors act in series, the  $C_{f,DL}$  can be neglected for the further calculations.
- (ii) Only for the PI MEA the major capacitive contribution comes from the opening electrodes ( $C_{DL}$ ), the feedline capacitive coupling ( $C_f$ ) is approximately 9 times smaller. In case of the ALD MEAs, the capacitive coupling of the feedlines to the electrolyte plays the dominant role, it is approximately 20 times larger compared to the contribution on the open electrodes.
- (iii) The agreement between the experimental and theoretical values is reasonable for the PI, TiO<sub>2</sub> and Ta<sub>2</sub>O<sub>5</sub> MEAs. For the MEAs the experimental capacitance ( $C_{exp}$ ) is 2-4 times larger than the theoretical capacitance ( $C_{total}$ ). The discrepancy is acceptable and might come from the choice of parameters (for example, the

permittivity and thickness of the Helmholtz layer, size and permittivity of the ALD layer). However, the difference between the experimental and theoretical value is extremely large for the  $\text{Al}_2\text{O}_3$  MEAs. This could be attributed to leakage of the passivation layer which is also visible in the behavior of the phase of the impedance (Figure 4.23b).

- (iv) However, most important for the sensitivity of the MEA is the areal coupling of different components, since the signal is restricted to the cell in the end. For the same area, the capacitance of the electrode ( $C_{DL}/A_e$ ) is much larger compared with the areal capacitance of the feedline ( $C_f/A_f$ ) for all passivation layers. The ratio between the different sensitivities ( $C_{DL}A_f/C_fA_e$ ) is 12 or 13000 times larger for the electrodes with ALD or PI passivation, respectively. This indicates that the major signal is recorded via the electrode. However, due to the strong coupling of the feedlines of the ALD MEAs to the electrolyte, we expect a significant attenuation of the signal for the ALD passivation.
- (v) A schematic circuit (Figure 4.25) demonstrates the situation when recording neuronal cell signals with the ALD MEAs. The MEAs are still most sensitive at the electrodes (size comparable to the size of neurons), however the feedline couples strongly to the electrolyte. As a result, the signal amplitude but also the noise will be modified (reduced).

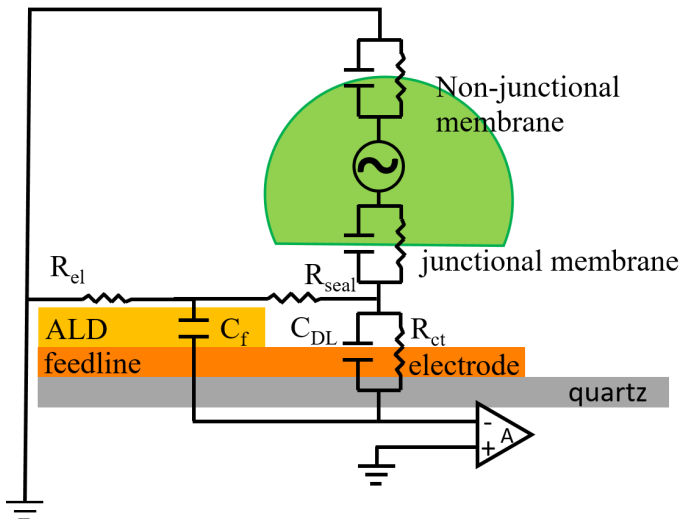


Figure 4.25: Schematic of the electric circuit for recording neuronal cells' action potential with ALD MEAs. The large feedline capacitor works as an attenuator, while the major signal is still coming from the electrode.

In order to test the signal propagation and cross talk within the MEAs, a stimulation potential of 100 mV is applied on one electrode to mimic the action potential generated by the electrogenic cells, while the other electrodes are used to record the signal (insert Figure 4.26).

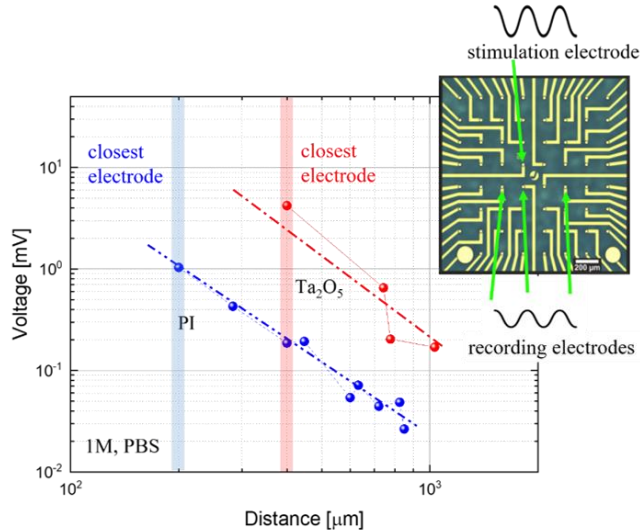


Figure 4.26: Voltage signal at electrodes adjacent to an electrode stimulated with a 100 mV pulse as function of the distance between both electrodes for a PI MEA (blue) and  $Ta_2O_5$  MEA (red) in PBS electrolyte. The blue and red shades represent the position of the closest electrodes for PI and  $Ta_2O_5$  MEA.

As shown in Figure 4.26, the stimulation signal (100 mV) is largely attenuated during propagation, the signal recorded on the electrodes are  $< 0.4$  mV for PI and  $< 10$  mV for the  $Ta_2O_5$  MEA at an electrode distance of 300  $\mu\text{m}$ . Even though the crosstalk is significantly larger of the ALD layer, the amplitude of the signal is still  $\sim 10$  times larger at the closest electrode. Therefore, we expect that the signal can still be recorded and that the cross-talk can be neglect.

### 4.3.2 Cell chip coupling for the different MEAs

In a first test, HL-1 cell cultures were chosen, since they tend to form confluent cell layers on the chip and, thus, should guarantee action potentials at the electrodes. The action potentials are repetitive and propagate through the cellular layer. The associated cell contraction is used to identify the maturity of the cell culture and, thus, the appropriate time to measure action potential signals. The cells are cultured on an encapsulated chips with

the different passivation layer coated with APTES until they form the expected confluent layer. When the cells reach a confluent state, they start to beat and produce the extracellular potentials, which can be recorded by the electrodes of the chip. Since the HL-1 cells form a syncytium, the signals propagate geometrically along the tissue. The recording of all electrodes on the chip is done simultaneously via the specially fabricated multichannel measurement system and controlled by the LabView-based software (see chapter 3.5.3).

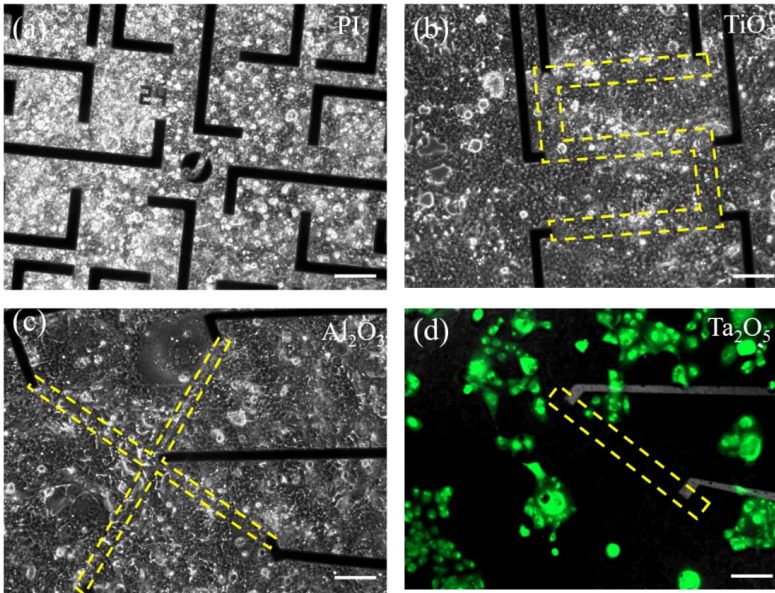


*Figure 4.27: Surface morphology of HL-1 cells on different MEAs at DIV 5 representing (a-c) microscope images of the cells distribution on PI, TiO<sub>2</sub> and Al<sub>2</sub>O<sub>3</sub> passivated MEAs respectively, and (d) a live staining florescent image of cells on Ta<sub>2</sub>O<sub>5</sub>. The white scale bars are 100 μm, the yellow dashed lines mark the open SiO<sub>2</sub> channels. All MEAs were seeded on the same day.*

Figure 4.27 shows typical HL-1 cell cultures at DIV 5 on the different MEAs. On PI, TiO<sub>2</sub> and Al<sub>2</sub>O<sub>3</sub> coated MEAs the cells form the expected confluent layers on the whole chip, whereas on Ta<sub>2</sub>O<sub>5</sub> only partially confluent layers form. This might be explained by the extremely negative surface potential of the Ta<sub>2</sub>O<sub>5</sub> layer. HL-1 cells seem to adhere and form confluent layers on materials with higher surface potential (PI, TiO<sub>2</sub> and Al<sub>2</sub>O<sub>3</sub>), whereas it doesn't adhere as well, forms clusters and is partially washed away during the change of the medium on Ta<sub>2</sub>O<sub>5</sub> due to the lower surface potential. An area where the cells are partially removed and don't form a confluent layer is shown in Figure 4.27d.

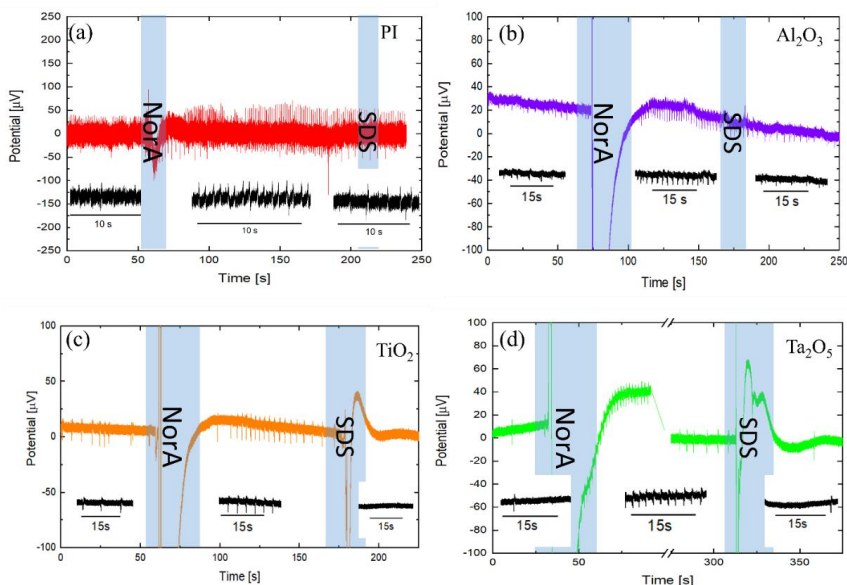


Figure 4.28: Action potential measurement of HL-1 cells on a (a) PI MEA, (b)  $\text{Al}_2\text{O}_3$  MEA, (c)  $\text{TiO}_2$  MEA and (d)  $\text{Ta}_2\text{O}_5$  MEA. The signals are recorded for 40-60s, then  $30\mu\text{l}$  NorA is added into the medium stimulating the cells, and after 180-320s, SDS is put into the medium, starting to perforate and dissolve the cellular layer, decreasing the amplitude and eventually ceasing the action potentials. The inserts indicate the three stages of the signal.

Figure 4.28 shows typical cell signals (action potentials) recorded for the HL-1 cell cultures at DIV 4 for the different MEAs. In order to prove the biological origin of the signals, stimulation and suppression experiments are performed on MEAs. While recording the signal time traces, norepinephrine (NorA), a drug for heart rate stimulation, is added to the medium. An increase of the NorA concentration from 0.1 mM to 0.2-0.3 mM in the medium, during the time indicated by the blue shade, leads to a significant increase of the beating frequency. After some time (2<sup>nd</sup> blue shaded regime) concentrated sodium dodecyl sulfate (SDS, a surfactant) solution is added to the same culture. The SDS perforates the cellular layer and in the end removes it from the chip's surface. This typically results in frequent but evanescent beatings which disappear completely after a couple of minutes, which is also the case for our MEAs.

We can therefore conclude that the spikes on the time trace originate from the HL-1 cells, i.e. we are able to record action potential from all MEAs.

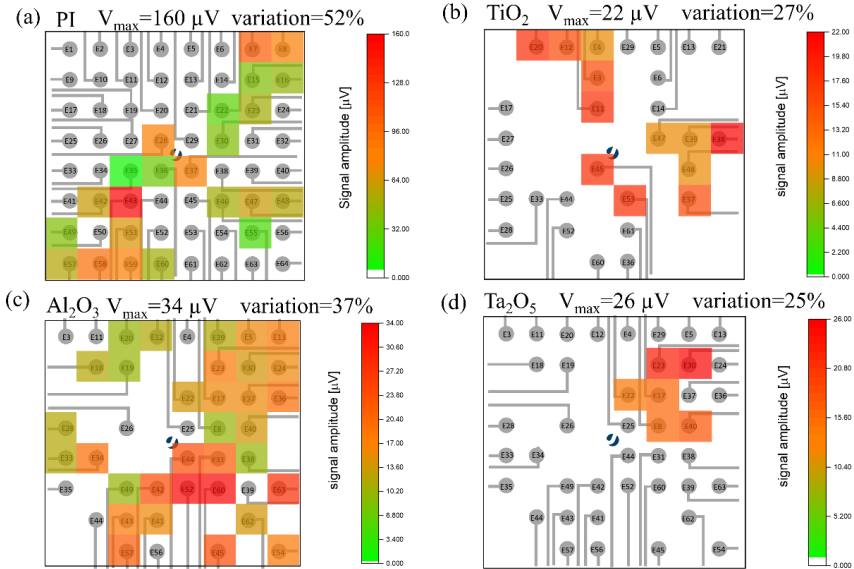


Figure 4.29: Heat plot of the signal amplitude on the different MEAs with (a) PI MEA, (b)  $\text{TiO}_2$ , (c)  $\text{Al}_2\text{O}_3$  and (d)  $\text{Ta}_2\text{O}_5$  as passivation.  $V_{\text{max}}$  represents the largest signal achieved on each of the MEAs, while the variation is defined as the standard deviation divided by the average value.

Normally we would expect that the amplitude of the signals should only slightly vary for the different channels, since the action potential propagates in the confluent layer of HL-1 cells. However, we observe a large difference not only between the different MEAs but also on the MEA (Figure 4.29). Actually, the PI MEA shows the largest signal but also a large signal variation (52%) for the different channels (only those showing signals are considered), whereas for ALD MEAs the signal is smaller and the variation is smaller (25%-37%), see Figure 4.30a. Before discussing the action potential amplitude, let's first consider the signal to noise ratio.

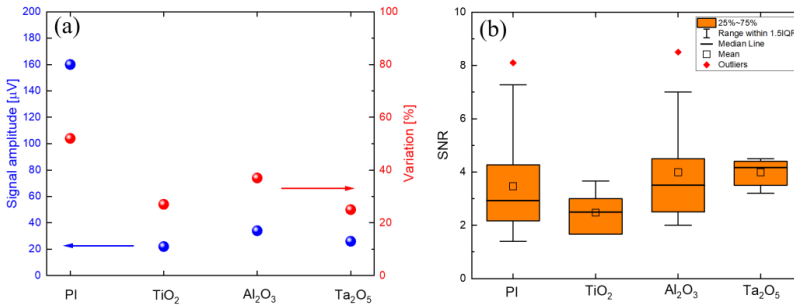


Figure 4.30: (a) Signal amplitude and their variations on different MEAs. The blue dots represent the largest signal that has been recorded, while the red dots are the variation coefficient of the heat plot (Figure 4.29). (b) Statistic of SNR of the action potential recordings for the different types of MEAs, the orange boxes illustrate the first quartile and the third quartile, the error bars represent the range of 1.5 times the interquartile range, the horizontal solid line in each box is the median value, the square is the average value, and the red diamonds represent the extreme values.

The signal to noise ratio (SNR) is actually the more important parameter for the characterization of the electronic cell chip coupling. For a comprehensive analysis we analyzed the SNR of the overall timetraces of all channels. By extracting their noise values, action potentials are extracted and their average amplitude (peak to peak) values. Surprisingly, the resulting average SNR is similar for all MEAs (Figure 4.30b), it lies at  $\sim 3$  and seems to be even best for the Ta<sub>2</sub>O<sub>5</sub> MEA. This represents a very promising result for the recording of cell signals in general. The large difference in the amplitude in combination with the promising small difference in the SNR of the different MEAs is surprising at first sight. It will be explained in the following by the difference of the electronic properties of the different MEAs.

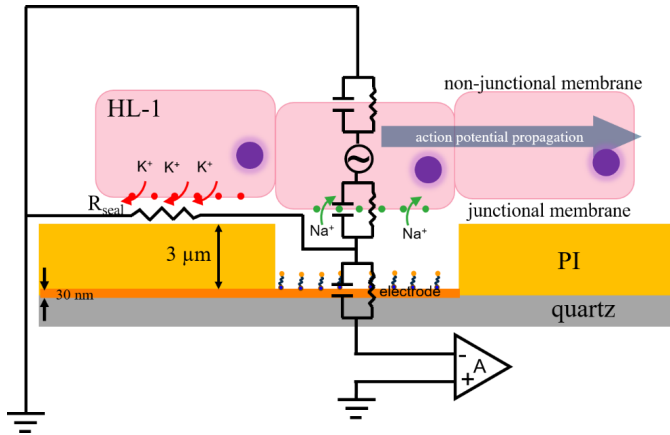


Figure 4.31: Equivalent circuit of the HL-1 cells' confluent layer on APTES coated PI MEAs.

Let's first consider the conventional PI MEA. The schematic in Figure 4.31 shows the equivalent circuit of the HL-1 cells' confluent layer on an APTES coated PI MEA. The opening of the electrode is  $24\ \mu\text{m}$  in diameter, which match the cell size, the PI passivation layer is around  $3\ \mu\text{m}$  thick, whereas the APTES SAM layer on the Pt should be only  $\sim 0.7\ \text{nm}$  thick [140]. The HL-1 cells form a confluent layer on top of the  $3\ \mu\text{m}$  elevated passivation layer, which makes it impossible for cells above the contact to be attached to the APTES layer on the electrodes. The resulting gap between cell and electrode is relatively large leading to a small sealing resistance. Therefore, we obtain the standard signal amplitude of  $100\text{-}400\ \mu\text{V}$  [81], but at the same time, the small sealing resistance leads to a large coupling of electrical signal (noise) to the electrode. Therefore, we obtain a standard signal with a standard SNR of  $\sim 3$ .

As for the ALD MEAs, the equivalent circuit should be slightly different (Figure 4.32). Unlike the thick PI layer, the ALD layers only possess a thickness of  $30\ \text{nm}$ , identical to the thickness of feedlines. Although this is still thicker than the  $0.7\ \text{nm}$  thick APTES layer, we expect that the cells can now bind to the electrodes as well as to the open channels with the APTES SAM covered  $\text{SiO}_2$ . As a result, we get a much better sealing of the cell, resulting a higher sealing resistance. In the end we get a much better coupling between cell and electrode.

However, at the same time, the thin ALD layer will cause a large capacitive coupling of the feedline to the electrode. It acts as a parallel capacitor and attenuates the signal and the SNR. Both effects affect the electronic signal and lead to a reduced signal but at the same time to a strongly reduced noise, and thus a more or less identical SNR of  $\sim 3$ .

Moreover, neither the leaky  $\text{Al}_2\text{O}_3$  passivation nor the semi-conducting behavior of the  $\text{TiO}_2$  layer seems to affect the SNR.

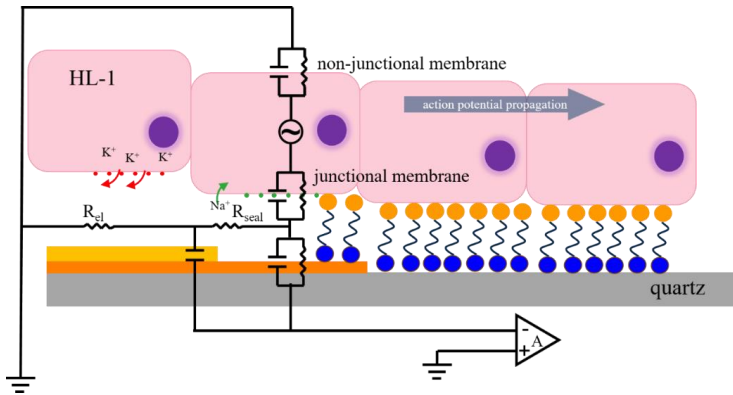


Figure 4.32: Equivalent circuit of the HL-1 cells' confluent layer on the APTES coated ALD MEA.

For all APTES coated MEAs we were able to record cellular activity from several channels on the chip. Some of the time traces are plotted in the left part of Figure 4.33. The time delay between different channels indicates that the signal is propagating through the cellular layer. For some of the MEAs more than 10 channels show action potentials, which allows to trace the spatial propagation of the signal (Figure 4.33 right part). We can try to identify pacemaker's position from the heat plots. For example, the pace maker is most likely at the left bottom corner of the PI passivated MEA (Figure 4.33b).

However, for the ALD chips the analysis is more difficult. For example, in some cases we observed pairs or different amounts of asynchronous action potentials which made us assume that there might be more than one pace makers beating at different frequencies and interfering with each other. Since for the ALD MEAs only a limited number of channels are working, it is difficult to locate the position of the pacemakers in this case.

In summary, all MEAs can be used for recording signal from HL-1 cells even though on  $\text{Ta}_2\text{O}_5$  HL-1 cells are not forming a complete confluent layer. A stimulation-suppression experiment demonstrates that the recorded signals stem from the HL-1 cells. The largest signal is acquired on PI MEAs, on the ALD MEAs the signals are much smaller. However, in all the cases we achieved a similar SNR of  $\sim 3$ .

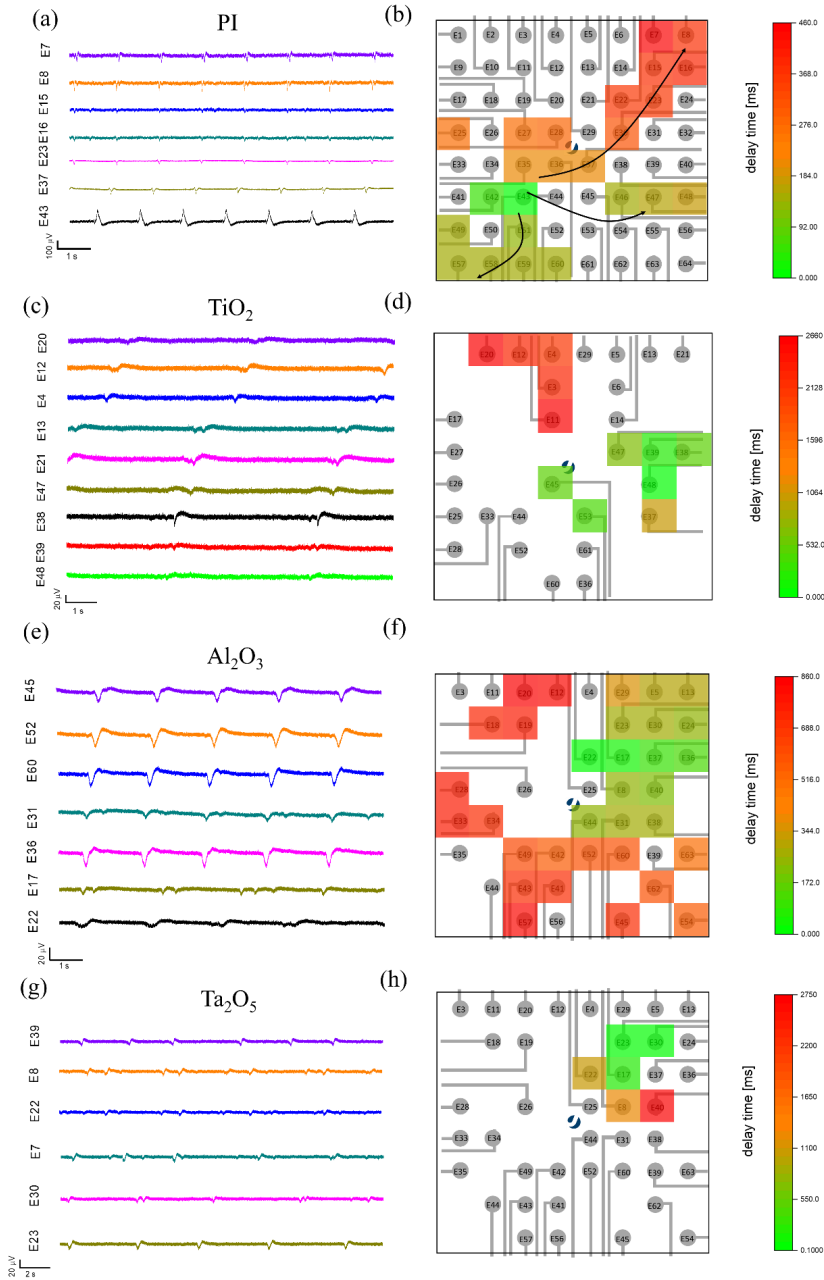


Figure 4.33: In vitro recordings for HL-1 cells on differently passivated APTES coated MEAs, showing time traces of action potentials and the corresponding heat plot of the time traces for (a)-(b) PI, (c)-(d)  $\text{TiO}_2$ , (e)-(f)  $\text{Al}_2\text{O}_3$  and (g)-(h)  $\text{Ta}_2\text{O}_5$  passivation.

### 4.3.3 Neuron cultures on ALD MEAs

Finally, in order to compare their cell affinity neuronal cells are seeded on the APTES coated MEAs. Before neuron cell seeding, all the samples are put into the MLD device for an APTES deposition, deposition parameters and post deposition treatment are identical to that used in the former chapter.

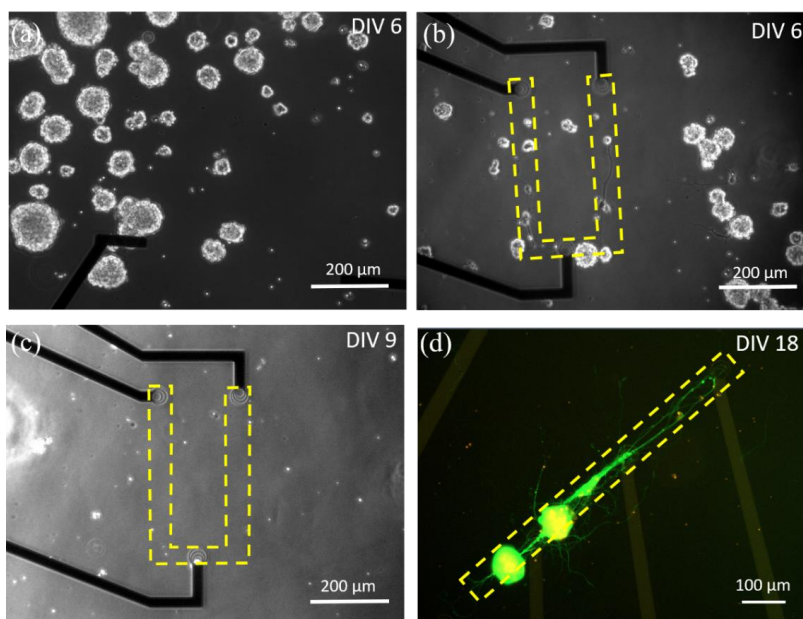


Figure 4.34: Cortical neuron cells distribution on  $Ta_2O_5$  MEAs showing (a) areas on  $Ta_2O_5$  with mainly freely moving clusters of neurons (neuronspheres) and (b-c) cortical neuron cells distribution in the vicinity of the open  $SiO_2$  channels at DIV 6, DIV 9 and DIV 18. The dashed yellow lines represent the open  $SiO_2$  channels and (d) shows a live-dead staining of one structure.

Let's illustrate the problems and the chance of this cell experiments on the example of the  $Ta_2O_5$  MEA (Figure 4.34). Figure 4.34a illustrates the main problem, cells seem to rather adhere to other cells than to adhere to the  $Ta_2O_5$  surface (probably due to the low surface potential). This way they form clusters of neurons (so called neuronspheres) which can migrate on the surface collecting more and more cells. During the change of medium some (or for a complete change nearly all) of the neuronspheres are removed leaving a (nearly) empty chip. This is visible in Figure 4.34(c).

Only in a few cases (and careful preparation), we could obtain the envisioned exclusive growth of neurons in the open  $SiO_2$  channels. One example of this is shown in Figure 4.34d,

where cells are able to survive on the chips up to 18 days when the experiment was terminated by a live-dead staining, which kills the cells.

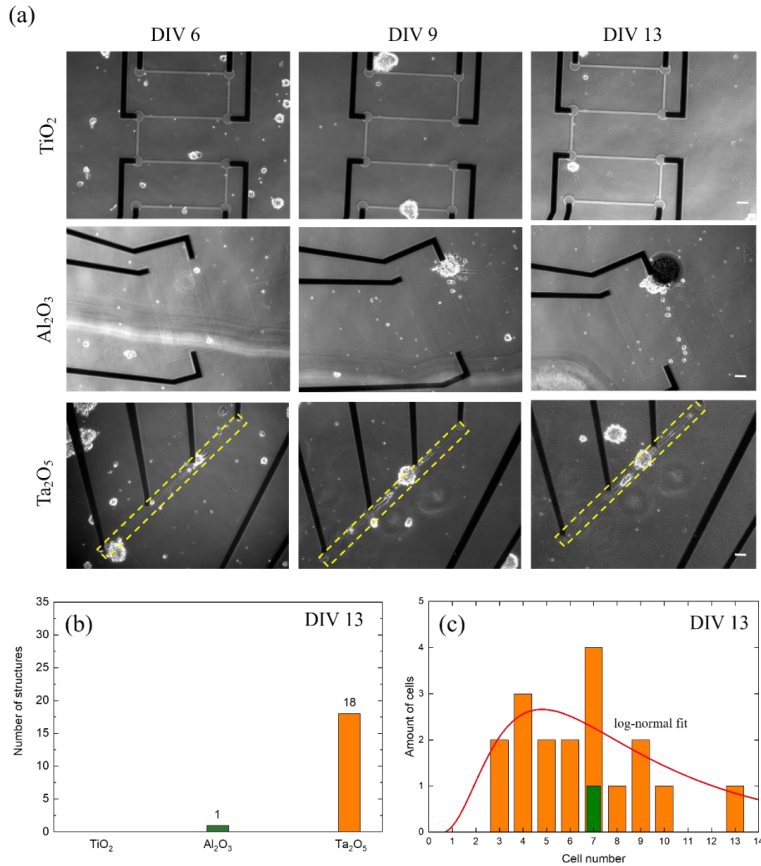


Figure 4.35. (a) Microscope image of neuron cell cultures on the different ALD MEAs for DIV 6, 9 and 13, the scale bar represents 100  $\mu\text{m}$ , (b) number of structures out of 31 which contain cells (the neuronspheres are excluded), and (c) distribution of the number of cells in the structures of the Ta<sub>2</sub>O<sub>5</sub> MEA (orange) and Al<sub>2</sub>O<sub>3</sub>(green). All statistics are done at DIV 13, the red curve represents a log-normal fit of the Ta<sub>2</sub>O<sub>5</sub> data.

In general, all ALD MEAs show the tendency to form neuronspheres (Figure 4.35a), indicating that the surface of the passivation layer is less attractive for the cells than neighboring cells or neuronspheres (the open SiO<sub>2</sub> channels seem to be too small). As a consequence, the cell density is very low (seeding density was 100k/chip). As a consequence, there were no visible neuron networks in the SiO<sub>2</sub> channels of TiO<sub>2</sub> MEA and only one single neuron network appears on the Al<sub>2</sub>O<sub>3</sub> MEA, whereas many of the structures on Ta<sub>2</sub>O<sub>5</sub> showed the guided cell growth, similar to the results shown in chapter

4.2. This might be attributed to the relatively small difference in the surface potential of, on one hand,  $\text{TiO}_2$  and  $\text{Al}_2\text{O}_3$ , and, on the other hand,  $\text{SiO}_2$ . Therefore, after the seeding of the cells, the electrostatic force is similar, the cells settle down randomly on the surface. With the time, the  $\text{TiO}_2$  and  $\text{Al}_2\text{O}_3$  seem not to be suitable for the neuron cells, therefore the cells rather form neuronspheres than stay on the surface.

However, in case of  $\text{Ta}_2\text{O}_5$  the deposited APTES doesn't attach firmly on the passivation layer. Therefore, the strongly negative surface potential compared with the APTES coated  $\text{SiO}_2$  in the open channels leads to a preferential attachment of cells on the positively charged  $\text{SiO}_2$  channel, resulting a neuron cell culture in the structure. Unfortunately, the statistical data (Figure 4.35b) indicate that for our design and preparation process (especially seeding density 100k) the number of cells that could form a neuron network in the channel is too small. The log-normal fit of the data indicates a mean cell density of 5-6, which is definitely too small for signal recording or even processing.

In this section it has been shown, that the envisioned guided neuron cell growth has been achieved only for the  $\text{Ta}_2\text{O}_5$  MEA, which shows the largest contrast in the surface potential. However, we were not able to record the cell signals from the neuron cells due to the small density of cells in the  $\text{SiO}_2$  channel of the test structures.

#### 4.3.4 Conclusion

In this final step we produced MEAs using the different oxides ( $\text{TiO}_2$ ,  $\text{Al}_2\text{O}_3$  and  $\text{Ta}_2\text{O}_5$ ) as a passivation layer and at the same time for the guidance of neuronal growth. For the latter, channels down to the  $\text{SiO}_2$  of the substrate were etched into the passivation layer, which should serve as areas for cell growth. These novel ALD MEAs were tested and compared with standard PI passivated MEAs.

- (i) The comparison of the electronic properties of the different MEAs showed that although the  $\text{Al}_2\text{O}_3$  passivation seems to be leaky and the  $\text{TiO}_2$  passivation is semiconducting, all MEAs should work. However, in contrast to the PI MEA, all ALD MEAs possess a large electronic coupling between the feedlines and the electrolyte.
- (ii) The test of recording of cell signals using HL-1 cells demonstrated that although the AP signal was significantly smaller for the ALD MEAs compared to the PI MEA, the signal-to-noise ratio was identical, i.e.  $\text{SNR} \approx 3$ , for all MEAs.
- (iii) Finally, the test of the guided growth of cortical neurons on the ALD MEAs showed that similar to the results shown in chapter 4.2, the best guidance is

obtained for the Ta<sub>2</sub>O<sub>5</sub> MEA. Cells survived the complete experimental duration of 18 days.

However, the total number of neurons in the individual test structure was too small to allow a neuronal network to be formed. Therefore, most likely structures with broader channel are necessary for these experiments.

## 5. Conclusion and outlook

In this work we introduced a novel method to tailor the interface of neuroelectronic devices in a way that (i) it becomes biocompatible and (ii) at the same time allows a guided growth of neurons on the substrate. By using different oxides which are functionalized with organic molecules, we can generate biocompatible areas onto which neurons either adhere, grow and mature, or preferably don't adhere. Furthermore, the resulting interface is extremely thin and robust, and therefore promises an electronic signal transfer in neuroelectronic devices (Figure 5.1). The work has been divided in three steps:

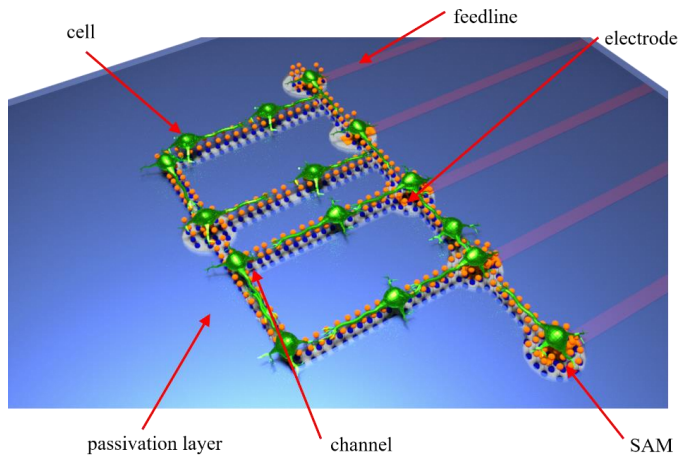


*Figure 5.1: Schematic of a neuroelectronic circuit based on a thin oxide passivation layer with channels for guided cell growth and a functionalization with organic molecules which forms SAMs in the channels for neuron growth and only physisorbed on the oxide passivation.*

In a first step, we investigated and optimized the formation and properties of self-assembled APTES monolayers of the organic molecule APTES on a standard surface, i.e. SiO<sub>2</sub>. In

order to achieve a well-controlled and reproducible deposition, we chose a gas-phase based MLD technique.

- We found that a post-deposition treatment (PDT) is crucial to the formation of APTES SAMs on SiO<sub>2</sub> for a deposition at room temperature. A PDT of at least 24 hours is necessary to achieve a stable, robust and high-quality SAM layer. Higher deposition temperature might reduce the required time.
- The electrokinetic potential turned out to be an ideal tool to analyze the state and stability of a freshly functionalized surface. We could not only determine the activation state of the SiO<sub>2</sub> surface which is vital for the binding of the organic molecules to the substrate, also the stability of the APTES coating could be monitored.

In a second step, we demonstrated that a different adhesiveness of neuronal cells can be achieved on different oxides functionalized with organic molecules. This allowed a guided cell growth (density and even directional) if combinations of oxides are used on a patterned substrate.

- We observed that only physisorbed layers can be achieved on some oxides (Ta<sub>2</sub>O<sub>5</sub> and TiO<sub>2</sub>), whereas chemically bound APTES SAMs form on others (SiO<sub>2</sub> and Al<sub>2</sub>O<sub>3</sub>).
- By utilizing the large difference in the surface potential in combination with the difference in the stability of the APTES coating, we chose the combination of SiO<sub>2</sub> (perfect adhesion of APTES and cells) and Ta<sub>2</sub>O<sub>5</sub> (little adhesion of APTES and cells) for tests of guided cell growth. In this system we obtained a large difference in cell density (ratio of ~8) and coverage with dendrites and growth cones (ratio of ~3.2).

In a final step, we demonstrated the new concept to neuroelectronic devices. We used extremely thin (30nm) ALD passivation consisting of the different oxides (TiO<sub>2</sub>, Al<sub>2</sub>O<sub>3</sub>, Ta<sub>2</sub>O<sub>5</sub>) on standard SiO<sub>2</sub> based MEAs. By opening the passivation not only at the electronic contact but also at areas at which cells are supposed to adhere and grow, patterned neuronal structures should be obtained and their electronic signals should be recorded.

- We demonstrated that in spite of the thin passivation and the resulting large capacitive coupling between the feedlines and electrolyte, all ALD MEAs can be used.
- Moreover, HL-1 cell experiments demonstrated that due to the large electronic coupling the ALD MEAs show much smaller action potential signal compared to standard PI passivated MEAs. However, at the same time the noise is also strongly reduced leading to a nearly identical signal-to-noise ratio (SNR≈3) for all (ALD and PI-passivated) MEAs. Since the SNR is the important parameter, the performance of the new MEAs is identical to that of the standard type of MEA.

- Finally, neuronal cell cultures were tested for the novel ALD MEAs using various test patterns for the guided cell growth. The channel size of  $\sim 50 \mu\text{m}$  for the test patterns led to a guided cell growth, however it was probably too small to allow the development of neuronal networks and, thus, the recording of neuronal signals.

In conclusion, even though we could not record signals from the neuronal networks in the final experiment, we successfully introduced a systemic method of combining SAMs and oxides to tailor biocompatibility and adhesion of cells and, thus, improve the robustness and (possible) even the electronic coupling of neuroelectronic interfaces. At the same time, the combinations of oxides and molecular layer can be used for a guided neuronal cell growth which not only allows the formation of complex 2D neuronal structures but, in case of the implementation into multi-electrode arrays (MEAs), an analysis of signal propagation and signal processing in neuronal structures. Therefore, this technology could be very promising for many neuroelectronic applications ranging from prostheses to *in vitro* long-term investigations.

Nevertheless, there are a number of necessary or possible improvements, which could be applied to this new technique (Figure 5.2):

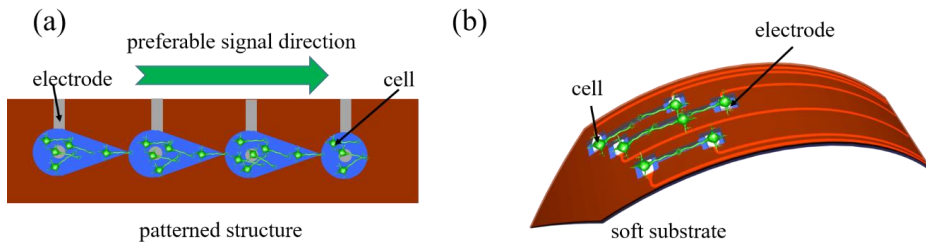


Figure 5.2: Schematic of ALD oxide based neuroelectronics with structured channels for preferable signal direction detection (a) and *in vivo* probe (b).

- Definitely the patterning of the oxide, used in the last part of the thesis to obtain complex 2D-structured neuronal networks, has to be improved. The size of the channels used in this work turned out to be too small to allow a development of neuronal network. In a first step, the channel size has to be enlarged.
- Alternatively, one could think of using more complex channels (Figure 5.2a) which could lead to the growth of networks, single neuron, and only axon depending on the size of the channel. This way, one could for instance obtain a growth with a preferential signal direction.
- Finally, a replacement of the rigid substrate (quartz was used in this work) by soft materials (for instance biocompatible soft polymers) could reduce the large mechanical

mismatch (Young's modulus) between cells and substrate. This could improve the cells growth behavior strongly and, moreover, could lead to a long-term stability of the cell-electrode contact (Figure 5.2b).

To conclude this work, I believe that the combination of organic molecules and oxides represents a promising opportunity for neuroelectronic applications.

---

## References

- [1] Yeoh, O. Can hacking the human brain produce medical miracles? <https://www.nst.com.my/lifestyle/sunday-vibes/2018/06/380777/can-hacking-human-brain-produce-medical-miracles>.
- [2] Berger, M. Nanotechnology for neural interfaces. <https://www.nanowerk.com/spotlight/spotid=47571.php>
- [3] Collins, K. Bionic hand can feed physical sensations directly to the brain. <https://www.wired.co.uk/article/darpa-creates-feeling-prosthetic-arm>.
- [4] Park, Y. Design and Fabrication of Soft Artificial Skin Using Embedded Microchannels and Liquid Conductors. *IEEE SENSORS JOURNAL*. **2012**, 12, 2711-2718.
- [5] Rogers, J. Cellular-scale, Injectable Electronics. <https://bioelectronics.northwestern.edu/research/cellular-scale-injectable-electronics.html>.
- [6] Taha, M.; Ashraf, H.; Caesarendra, W. A Brief Description of Cyclic Voltammetry Transducer-Based Non-Enzymatic Glucose Biosensor Using Synthesized Graphene Electrodes. *Appl. Syst. Innov.* **2020**, 3, 32.
- [7] Wrobel, G.; Hoeller, M.; Ingebrant, S.; Dieluweit, S.; Sommerhage, F.; Bochem, H.; Offenhaeusser, A. Transmission Electron Microscopy Study of the Cell-sensor Interface. *J. R. Soc. Interface*. **2008**, 5, 213-222.
- [8] Blau, A. Cell Adhesion Promotion Strategies for Signal Transduction Enhancement in Microelectrode Array *in vitro* Electrophysiology: An Introductory Overview and Critical Discussion. *Current Opinion in Colloid and Interface Science*. **2013**, 18, 481-492.
- [9] Trafton, A. New tool offers snapshots of neuron activity. <https://news.mit.edu/2017/new-tool-offers-snapshots-neuron-activity-0626>.
- [10] Ermis, M.; Antmen, E.; Hasirci, V. Micro and Nanofabrication methods to control cell-substrate interactions and cell behavior: A review from the tissue engineering perspective. *Bioactive Materials*. **2018**, 3, 355-369.
- [11] Voldman, J.; Gray, M.; Schmidt, M.; Microfabrication in biology and medicine. *Annu. Rev. Biomed. Eng.* **1999**, 1, 401-425.
- [12] Rajnicek, A.; Britland, S.; McCaig, C. Contact guidance of CNS neurites on grooved quartz: influence of groove dimensions, neuronal age and cell type, *J. Cell Sci.* **1997**, 110, 2905-2913.
- [13] Hutmacher, D. Scaffold design and fabrication technologies for engineering tissues: state of the art and future perspectives, *J. Biomater. Sci. Polym.* **2001**, 12, 107-124.
- [14] Charest, J.; Bryant, L.; Garcia, A.; King, W. Hot embossing for micropatterned cell substrates, *Biomaterials*. **2004**, 25, 4767-4775.
- [15] Hasirci, V.; Kenar, H.; Novel surface patterning approaches for tissue engineering and their effect on cell behavior, *Nanomedicine*. **2006**, 1, 73-90.

- [16] Mahmud, G.; Campbell, C.; Bishop, K.; Komarova, Y.; Chaga, O.; Soh, S.; Huda, S.; Kandere-Grzybowska, K.; Grzybowski, B. Directing cell motions on micropatterned ratchets, *Nat. Phys.* **2009**, 5, 606-612.
- [17] Hasirci, V.; Pepe-Mooney, B. Understanding the cell behavior on nano-/micro-patterned surfaces, *Nanomedicine*. **2012**, 7, 1375-1389.
- [18] Martínez, E.; Engel, E.; Planell, J.; Samitier, J. Effects of artificial micro- and nano-structured surfaces on cell behavior. *Ann. Anat. - Anat. Anzeiger*. **2009**, 191, 126-135.
- [19] Lim, J.; Donahue, H. Cell sensing and response to micro- and nanostructured surfaces produced by chemical and topographic patterning. *Tissue Eng.* **2007**, 13, 1879-1891.
- [20] Bettinger, C.; Langer, R.; Borenstein, J. Engineering substrate topography at the micro- and nanoscale to control cell function, *Angew. Chem. Int.* **2009**, 48, 5406-5415.
- [21] Khalili, A.; Ahmad, M. A Review of Cell Adhesion Studies for Biomedical and Biological Applications, *Int. J. Mol. Sci.* **2015**, 16, 18149-18184.
- [22] Goddard, J.; Hotchkiss, J. Polymer surface modification for the attachment of bioactive compounds, *Prog. Polym. Sci.* **2007**, 32, 698-725.
- [23] Xu, L.; Siedlecki, C. Effects of surface wettability and contact time on protein adhesion to biomaterial surfaces, *Biomaterials*. **2007**, 28, 3273-3283.
- [24] Schneider, G.; English, A.; Abraham, M.; Zaharias, R.; Stanford, C.; Keller, J. The effect of hydrogel charge density on cell attachment. *Biomaterials*. **2004**, 25, 3023-3028.
- [25] Huang, W.; Anvari, B.; Torres, J.; LeBaron, R.; Athanasiou, K. Temporal effects of cell adhesion on mechanical characteristics of the single chondrocyte. *J. Orthop. Res.* **2003**, 21, 88-95.
- [26] Helenius, J.; Heisenberg, C.; Gaub, H.; Muller, D. Single-cell force spectroscopy. *J. Cell Sci.* **2008**, 121, 1785-1791.
- [27] Bacakova, L.; Filova, E.; Parizek, M.; Rumi, T.; Svorcik, V. Modulation of cell adhesion, proliferation and differentiation on materials designed for body implants. *Biotechnology Advances*, **2011**, 29, 739-767.
- [28] Kubova, O.; Svorcik, V.; Heitz, J.; Moritz, S.; Romanin, C.; Matejka, P. Characterization and cytocompatibility of carbon layers prepared by photo-induced chemical vapor deposition. *Thin Solid Films* **2007**, 515, 6765-72.
- [29] Parizek, M.; Kasalkova, N.; Bacakova, L.; Slepicka, P.; Lisa, V.; Blazkova, M. Improved adhesion, growth and maturation of vascular smooth muscle cells on polyethylene grafted with bioactive molecules and carbon particles. *Int J Mol Sci.* **2009**, 10, 4352-74.
- [30] Kanchanawong, P.; Shtengel, G.; Pasapera, A.; Ramko, E.; Davidson, M.; Hess, H. Nanoscale architecture of integrin-based cell adhesions. *Nature* **2010**, 468, 580-4.
- [31] Xu, L.; Siedlecki, C. Effects of surface wettability and contact time on protein adhesion to biomaterial surfaces. *Biomaterials* **2007**, 28, 3273-3283.

- [32] Svorcik, V.; Kasalkova, N.; Slepicka, P.; Zaruba, K.; Kral, V.; Bacakova, L. Cytocompatibility of Ar<sup>+</sup> plasma treated and Au nanoparticle-grafted PE. *Nucl Instr Meth Phys Res B*. **2009**, 267, 1904-10.
- [33] Eisenberg, J.; Beaumont, K.; Takawira, D.; Hopkinson, S.; Mrksich, M.; Budinger, G.; Jones, J. Plectin-containing, centrally localized focal adhesions exert traction forces in primary lung epithelial cells, *J. Cell Sci*. **2013**, 126, 3746-3755.
- [34] Kasalkova, N.; Slepicka, P.; Kolska, Z.; Sajadl, P.; Bacakova, L.; Rimpelova, S.; Svorcik V. Cell adhesion and proliferation on polyethylene grafted with Au nanoparticles. *Nuclear Instruments and Methods in Physics Research B*. **2012**, 272, 391-395.
- [35] Liu, L.; Chen, S.; Giachelli, C.; Ratner, B.; Jiang, S. Controlling osteopontin orientation on surfaces to modulate endothelial cell adhesion. *J Biomed Mater Res A* **2005**, 74, 23-31.
- [36] Masui, M.; Takata, H.; Kominami, T. Cell adhesion and the negative cell surface charges in embryonic cells of the starfish *Asterina pectinifera*. *Electrophoresis* **2002**, 23, 2087-95.
- [37] Bet MR, Goissis G, Vargas S, Selistre-de-Araujo HS. Cell adhesion and cytotoxicity studies over polyanionic collagen surfaces with variable negative charge and wettability. *Biomaterials* **2003**, 24, 131-7.
- [38] Tiller, J.; Bonner, G.; Pan, L.; Klibanov, A. Improving biomaterial properties of collage films by chemical modification. *Biotechnol Bioeng* **2001**, 73, 246-52.
- [39] Lee, H.; Hong, J.; Goo, H.; Lee, W.; Park, K.; Kim, S. Improved blood compatibility and decreased VSMC proliferation of surface-modified metal grafted with sulfonated PEG or heparin. *J Biomater Sci Polym*. **2002**, 13, 939-52.
- [40] Kim, H.; Kim, S.; Kim, M.; Lee, E.; Oh, H.; Oh, W. Varying Ti-6Al-4V surface roughness induces different early morphologic and molecular responses in MG63 osteoblast-like cells. *J Biomed Mater Res* **2005**, 74, 366-73.
- [41] Schmaltz, T. Sforazzini, G. Reichert, T. Frauenrath, H. Self-Assembled Monolayers as Patterning Tool for Organic Electronic Devices. *Adv Mater*. **2017**, 1605286, 1-25.
- [42] Yoo, P.; Choi, S.; Kim, J.; Suh, D.; Baek, S.; Kim, T.; Lee, H. Alternative to pentacene patterning for organic thin film transistor. *Chem Mater*. **2004**, 16, 5000.
- [43] Zhang, L.; Kaplan, D. Neural Engineering: From Advanced Biomaterials to 3D Fabrication Techniques. **2016**
- [44] Lee, K.; Lim, J.; Mirkin, C. Protein Nanostructures Formed via Direct-Write Dip-Pen Nanolithography. *J. Am. Chem. Soc.* **2003**, 12, 5588-5589.
- [45] Nam, J.; Han, S.; Lee, K.; Liu, X.; Ratner, M.; Mirkin, C. Bioactive protein nanoarrays on nickel oxide surfaces formed by dip-pen nanolithography. *Angew. Chem. Int. Ed.* **2004**, 43, 1246-1249.
- [46] Lim, J.; Ginger, D.; Lee, K.; Heo, J.; Nam, J.; Mirkin, C. Direct-Write Dip-Pen Nanolithography of Proteins on Modified Silicon Oxide Surfaces. *Angew. Chem. Int. Ed.*

**2003**, 42, 2309-2312.

[47] Salaita, K.; Lee, S.; Wang, X.; Huang, L.; Dellinger, T.; Liu, C.; Mirkin, C. Sub-100 nm, centimeter-scale, parallel dip-pen nanolithography. *Small*. **2005**, 1, 940-5.

[48] Salaita, K.; Wang, Y.; Fragala, J.; Vega, R.; Liu, C.; Mirkin, C. Massively parallel dip-pen nanolithography with 55 000-pen two-dimensional arrays. *Angew. Chem. Int. Ed.* **2006**, 45, 7220-3.

[49] Huo, F.; Zheng, Z.; Zheng, G.; Giam, L.; Zhang, H.; Mirkin, C. Polymer Pen Lithography. *Science* **2008**, 321, 1658-1660.

[50] Sahin, O.; Ashokkumar, M.; Ajayan, P. Micro- and nanopatterning of biomaterial surfaces. *Fundamental Biomaterials: Metals*. **2018**, 67-78.

[51] Brodoceanu, D.; Kraus, T. Micro- and Nanopatterning of Biomaterial Surfaces. *Biomaterials Surface Science*. **2013**. 285-309.

[52] Kim, D.; Lee, H.; Lee, Y.; Nam, J.; Levchenko, A. Biomimetic Nanopatterns as Enabling Tools for Analysis and Control of Live Cells. *Adv. Mater.* **2010**, 22, 4551-4566.

[53] Brodoceanu, D.; Kraus, T. Micro- and Nanopatterning of Biomaterial Surfaces. *Biomaterials Surface Science*, **2013**, 285-309.

[54] Ioannis, L.; Liakos, R.; Newman, E.; Morgan, R. Study of the Resistance of SAMs on Aluminium to Acidic and Basic Solutions Using Dynamic Contact Angle Measurement. *Langmuir*. **2007**, 23, 995-999.

[55] Park, J.; Shon, J. Corrosion protection by epoxy coating containing multi-walled carbon nanotubes. *Journal of Industrial and Engineering Chemistry* **2013**, 19, 849-853.

[56] Iwata, H.; Arima, Y. Effect of wettability and surface functional groups on protein adsorption and cell adhesion using well-defined mixed self-assembled monolayers. *Biomaterials* **2007**, 28, 3074-3082.

[57] Perkins, C. Molecular Anchors for Self-Assembled Monolayers on ZnO: A Direct Comparison of the Thiol and Phosphonic Acid Moieties, *J. Phys. Chem. C*. **2009**, 113, 18276-18286.

[58] Newton, L.; Slater, T.; Clark, N.; Vijayaraghavan, A. Self-assembled monolayers (SAMs) on metallic surfaces (gold and graphene) for electronic applications, *J. Mater. Chem. C*, **2013**, 1, 376-393.

[59] Jans, K.; Bonroy, K.; De Palma, R.; Reekmans, G.; Jans, H.; Laureyn, W.; Smet, M.; Borghs, G.; Maes, G. Stability of Mixed PEO-Thiol SAMs for Biosensing Applications. *Langmuir* **2008**, 24, 3949-3954.

[60] Lessel, M.; Bäumchen, O.; Klos, M.; Hähl, H.; Fetzer, R.; Paulus, M.; Seemann, R.; Jacobs, K. Self-assembled silane monolayers: an efficient step-by-step recipe for high-quality, low energy surfaces. *Surface and Interface Analysis*, **2015**, 47, 557-564.

[61] Haensch, C.; Hoepfener, S.; Schubert, U. Chemical modification of self-assembled silane based monolayers by surface reactions. *Chem. Soc. Rev.* **2010**, 39, 2323-2334.

- [62] Karakoy, M.; Gultepe, E.; Pandey, S.; Khashab, M.; Gracias, D. Silane surface modification for improved bioadhesion of esophageal stents. *Applied Surface Science*, 2014, 311, 684-689.
- [63] Hofer, R.; Textor, M.; Spencer, N. Alkyl Phosphate Monolayers, Self-Assembled from Aqueous Solution onto Metal Oxide Surfaces. *Langmuir* **2001**, 17, 4014-4020.
- [64] Gnauck, M.; Jaehne, E.; Blaettler, T.; Tosatti, S.; Textor, M.; Adler, H. Carboxy-Terminated Oligo(ethylene glycol)-Alkane Phosphate: Synthesis and Self-Assembly on Titanium Oxide Surfaces. *Langmuir* **2007**, 23, 377-381.
- [65] Kim, B.; Choi, S.; Zhu, X.; Frisbie, C. Molecular Tunnel Junctions Based on  $\pi$ -Conjugated Oligoacene Thiols and Dithiols between Ag, Au, and Pt Contacts: Effect of Surface Linking Group and Metal Work Function. *J. Am. Chem. Soc.* **2011**, 133, 49, 19864-19877.
- [66] Bhushan, B.; Kwak, K. Gupta, S.; Lee, S. Nanoscale adhesion, friction and wear studies of biomolecules on silane polymer-coated silica and alumina-based surfaces. *J R Soc Interface*. **2009**, 6, 719-733.
- [67] Picarda, L.; Phalip, P.; Fleury, E.; Ganachauda, F. Chemical adhesion of silicone elastomers on primed metal surfaces: A comprehensive survey of open and patent literatures. *Progress in Organic Coatings* **2015**, 80, 120-141.
- [68] Arkles, B. Silane Coupling Agents: Connecting across Boundaries, Gelest, 2014
- [69] Xia, Y.; Whitesides, G. Soft Lithography. *Annual Review of Materials Research*, **1998**, 28, 153-184.
- [70] Maboudian, R.; Howe, R. Critical Review: Adhesion in surface micromechanical structures. *Journal of Vacuum Science & Technology B*, **1997**, 15,1.
- [71] Gunda, N.; Singh, M.; Norman, L.; Kaur, K.; Mitra, S. Optimization and characterization of biomolecule immobilization on silicon substrates using (3-aminopropyl) triethoxysilane (APTES) and glutaraldehyde linker. *Applied Surface Science* **2014**, 305, 522-530.
- [72] Collart-Dutilleul, P.; Secret, E.; Panayotov, I.; de Periere, D.; Martin-Palma, R.; Torres-Costa, V. Martin, M.; Gergely, C.; Durand, J.; Cunin, F.; Cuisinier, F. Adhesion and Proliferation of Human Mesenchymal Stem Cells from Dental Pulp on Porous Silicon Scaffolds. *ACS Appl. Mater. Interfaces* **2014**, 6, 1719-1728.
- [73] Linda, A.; Lee, C.; O'Ferrall, C. Covalent Attachment of Synthetic DNA to Self-Assembled Monolayer Films. *Nucleic Acids Research*, **1996**, 24, 3031-3039.
- [74] Hikosaka, R.; Nagata, F.; Tomita, M.; Kato, K. Adsorption and desorption characteristics of DNA onto the surface of amino functional mesoporous silica with various particle morphologies. *Colloids and Surfaces B: Biointerfaces*. **2016**, 140, 262-268.
- [75] Haddada, M.; Blanchard, J.; Casale, S.; Krafft, J.; Vallee, A.; Methivier, C.; Boujday, S. Optimizing the immobilization of gold nanoparticles on functionalized silicon surfaces: amine- vs thiol-terminated silane. *Gold Bull*, **2013**, 46, 335-341.

- [76] Markov, A.; Maybeck, V.; Wolf, N.; Mayer, D.; Offenhäusser, A.; Wördenweber, R. Engineering of Neuron Growth and Enhancing Cell-Chip Communication via Mixed SAMs. *ACS Appl. Mater. Interfaces* **2018**, 10, 18507-18514.
- [77] Spira, M.; Hai, A. Multi-electrode array technologies for neuroscience and cardiology, *NATURE NANOTECHNOLOGY*, **2013**, 8, 83-94.
- [78] Hutzler, M. et al. High-resolution multitransistor array recording of electrical field potentials in cultured brain slices. *J. Neurophysiol.* **2006**, 96, 1638-1645.
- [79] Berdondini, L. et al. Active pixel sensor array for high spatio-temporal resolution electrophysiological recordings from single cell to large scale neuronal networks. *Lab Chip.* **2009**, 2644-2651.
- [80] Jones, I. et al. The potential of microelectrode arrays and microelectronics for biomedical research and diagnostics. *Anal. Bioanal. Chem.* **2011**, 399, 2313-2329.
- [81] Kireev D. Graphene Devices for Extra Cellular Measurements. Ph.D thesis, RWTH Aachen, Aachen. **2017**.
- [82] Action potentials. <http://hyperphysics.phy-astr.gsu.edu/hbase/Biology/actpot.html>
- [83] Action potentials. <https://teachmephysiology.com/nervous-system/synapses/action-potential/>
- [84] The Student Physiologist. <https://thephysiologist.org/study-materials/cardiac-action-potentials/>
- [85] Iwanaga, Y.; Braun, D.; Fromherz, P. No correlation of focal contacts and close adhesion by comparing GFP-vinculin and fluorescence interference of Dil. *Eur. Biophysics J. Biophysics Lett.* **2001**, 30, 17-26.
- [86] Lambacher, A.; Fromherz, P. Luminescence of dye molecules on oxidized silicon and fluorescence interference contrast microscopy of biomembranes. *J. Opt. Soc. Am. B* **2002**, 19, 1435-1453.
- [87] Gleixner, R.; Fromherz, P. The extracellular electrical resistivity in cell adhesion. *Biophys. J.* 2006, 90, 2600-2611.
- [88] Spatz, J.; Geiger, B. Molecular engineering of cellular environments: cell adhesion to nano-digital surfaces. *Methods Cell Biol.* **2007**, 83, 89-111.
- [89] Fromherz, P. Three levels of neuroelectronic interfacing: silicon chips with ion channels, nerve cells, and brain tissue. *Ann. NY Acad. Sci.* **2006**, 1093, 143-160.
- [90] Maccione, A. et al. Experimental investigation on spontaneously active hippocampal cultures recorded by means of high-density MEAs: analysis of the spatial resolution effects. *Front. Neuroeng.* **2010**, 3, 1-12.
- [91] Buitenweg, J.; Rutten, W.; Marani, E. Geometry-based finite-element modeling of the electrical contact between a cultured neuron and a microelectrode. *IEEE Trans. Biomed. Eng.* **2003**, 50, 501-509.
- [92] Frey, U.; Egert, U.; Heer, F.; Hafizovic, S.; Hierlemann, A. Microelectronic system for high-resolution mapping of extracellular electric fields applied to brain slices. *Biosens.*

*Bioelectron.* **2009**, 24, 2191-2198.

[93] Oka, H.; Shimono, K.; Ogawa, R.; Sugihara, H.; Taketani, M. A new planar multielectrode array for extracellular recording: application to hippocampal acute slice. *J. Neurosci. Methods* **1999**, 93, 61-67.

[94] Kim, J.; Kang, G.; Nam, Y.; Choi, Y.; Surface-modified microelectrode array with flake nanostructure for neural recording and stimulation. *Nanotechnology*, **2010**, 21, 85303.

[95] Bruggemann, D. et al. Nanostructured gold microelectrodes for extracellular recording from electrogenic cells. *Nanotechnology*, **2011**, 22, 265104.

[96] Shein, M. et al. Engineered neuronal circuits shaped and interfaced with carbon nanotube microelectrode arrays. *Biomed. Microdevices*, **2009**, 11, 495-501.

[97] Helmholtz, H. Studien ueber electrische Grenzschichten. *Annalen der Physik und Chemie*, **1879**, 243, 337-382.

[98] Gouy, M. Sur la constitution de la charge electrique a la surface dun electrolyte. *Journal de Physique Theorique et Appliquee*, **1910**, 9, 457-468.

[99] Chapman, D. L. LI. A contribution to the theory of electrocapillarity. *Philosophical Magazine Series*. **1913**, 25, 475-481.

[100] F. Scholz. Electroanalytical methods, *Springer* **2010**.

[101] Bard, A.; Faulkner, L; Electrochemical Methods: Fundamentals and Applications. *Wiley*, **2000**.

[102] Stern, O. Zur Theorie der Elektrolytischen Doppelschicht. *Zeitschrift fuer Elektrochemie und angewandte physikalische Chemie*. **1924**, 30, 508-516.

[103] Yuan, X.; Wolf, N.; Mayer, D.; Offenhäusser, A.; Wördenweber, R. Vapor-Phase Deposition and Electronic Characterization of 3-Aminopropyltriethoxysilane Self-Assembled Monolayers on Silicon Dioxide. *Langmuir* **2019**, 35, 8183-8190.

[104] Markov, A. Tailoring and characterisation of bioelectronic interfaces. Ph.D thesis, Cologne University, Cologne. **2017**.

[105] Markov, A.; Greben, K.; Mayer, D.; Offenhäusser, A.; Wördenweber, R. In Situ Analysis of the Growth and Dielectric Properties of Organic Self-Assembled Monolayers: A Way to Tailor Organic Layers for Electronic Applications. *ACS Appl. Mater. Interfaces* **2016**, 8, 16451-16456.

[106] Ehrler, J. Fabrication and Characterization of a new MEA Topography using ALD Passivation. 2019.

[107] Atomic Layer Deposition.

<https://www.imtek.de/professuren/nano/forschung/aldsurface>

[108] How does Electron Beam Evaporation work? <https://www.tungsten.com/how-does-electron-beam-evaporation-work/>

- [109] Airaksinen V. Handbook of Silicon Based MEMS Materials and Technologies (Second Edition). *Micro and Nano Technologies* **2015**, 381-390.
- [110] Wang, H. Chu, P. Characterization of Biomaterials. **2013**, 105-174.
- [111] Hebbbar, R.; Isloor, A.; Ismail, A. Membrane Characterization, **2017**, 219-255.
- [112] Young T. An essay on the cohesion of fluids. *Philos Trans R Soc Lond* **1805**, 95, 65-87.
- [113] Hunter, R. Zeta Potential in Colloid Science: Principles and Applications; Academic Press: London, **1981**.
- [114] Greben, K.; Li, P.; Mayer, D.; Offenhäusser, A.; Wördenweber, R. Immobilization and Surface Functionalization of Gold Nanoparticles Monitored via Streaming Current/potential Measurements. *J. Phys. Chem. B* **2015**, 119, 5988-5994.
- [115] Yahia, L.; Mireless, L. X-ray photoelectron spectroscopy (XPS) and time-of-flight secondary ion mass spectrometry (ToF SIMS), *Characterization of Polymeric Biomaterials* **2017**, 83-97.
- [116] Akhtar, K.; Khan, S.; Khan, S.; Asiri, A. Scanning Electron Microscopy: Principle and Applications in Nanomaterials Characterization. *Handbook of Materials Characterization*, 113-145.
- [117] Sebastian Dunst and Pavel Tomancak. Imaging Flies by Fluorescence Microscopy: Principles, Technologies, and Applications. *Genetics*, **2019**, 211, 15-34.
- [118] Hermanson, G. Fluorescent Probes. *Bioconjugate Techniques* (Third edition) **2013**, 395-463.
- [119] Schindelin, J.; Arganda-Carreras, I.; Frise, E. et al. Fiji: an open-source platform for biological-image analysis. *Nature methods*, **2012**, 9, 676-682.
- [120] Yuan, X.; Wolf, N.; Hondrich, T.; Shokoohimehr, P.; Milos, F.; Glass, M.; Mayer, D.; Maybeck, V.; Prömpers, M.; Offenhäusser, A.; Wördenweber, R. Engineering Biocompatible Interfaces via Combinations of Oxide Films and Organic Self-Assembled Monolayers. *ACS Appl. Mater. Interfaces* **2020**, 12, 14, 17121-17129.
- [121] Claycomb, W.; Lanson Jr, N.; Stallworth, B.; Egeland, D.; Delcarpio, J.; Bahinski, A.; Izzo Jr, N. HL-1 cells: A cardiac muscle cell line that contracts and retains phenotypic characteristics of the adult cardiomyocyte. *PNAS*. 1998. 95, 2979-2984.
- [122] Vandenberg, E.; Bertilsson, L.; Liedberg, B.; Uvdal, K.; Erlandsson, R.; Elwing, H.; Lundström, I. Structure of 3-Aminopropyl Triethoxy Silane on Silicon Oxide. *J. Colloid Interface Sci.* **1991**, 147, 103-118.
- [123] Markov, A.; Wolf, N.; Yuan, X.; Mayer, D.; Maybeck, V.; Offenhäusser, A.; Wördenweber, R. Controlled Engineering of Oxide Surfaces for Bioelectronics Applications Using Organic Mixed Monolayers. *ACS Appl. Mater. Interfaces* **2017**, 9, 29265-29272.
- [124] Batyrev, I.; Tuttle, B.; Fleetwood, D.; Schrimpf, R.; Tsetseris, L.; Pantelides, S. Reactions of Water Molecules in Silica-Based Network Glasses. *Phys. Rev. Lett.* **2008**, 100, 110

1-4.

[125] Kuo, C.; Chang, H.; Liu, C.; Lee, S.; You, Y.; Shyue, J. Effect of Surface Chemical Composition on the Surface Potential and Iso-Electric Point of Silicon Substrates Modified with Self-Assembled Monolayers. *Phys. Chem. Chem. Phys.* **2011**, *13*, 3649-3653.

[126] Cai, K.; Frant, M.; Bossert, J.; Hildebrand, G.; Liefeth, K.; Jandt, K. Surface Functionalized Titanium Thin Films: Zeta-Potential, Protein Adsorption and Cell Proliferation. *Colloids and Surfaces B: Biointerfaces* **2006**, *50*, 1-8.

[127] Borukhov, I.; Andelman, D.; Orland, H. Steric Effects in Electrolytes: A Modified Poisson-Boltzmann Equation. *Phys. Rev. Lett.* **1997**, *79*, 435-438.

[128] Lyklema, J. Surface Conduction. *J. Phys. Condens. Matter* **2001**, *13*, 5027-5034.

[129] Sharma, M.; Resta, R.; Car, R. Dipolar Correlations and the Dielectric Permittivity of Water. *Phys. Rev. Lett.* **2007**, *98*, 1-4.

[130] Suni, T.; Henttinen, K.; Suni, I.; Mäkinen, J. Effects of Plasma Activation on Hydrophilic Bonding of Si and SiO<sub>2</sub>. *J. Electrochem. Soc.* **2002**, *149*, 348-351.

[131] Stevens, M. Thoughts on the Structure of Alkylsilane Monolayers. *Langmuir* **1999**, *15*, 2773-2778.

[132] Vezenov, D.; Noy, A.; Rozsnyai, L.; Lieber, C. Force Titrations and Ionization State Sensitive Imaging of Functional Groups in Aqueous Solutions by Chemical Force Microscopy. *J. Am. Chem. Soc.* **1997**, *119*, 2006-2015.

[133] Chaiyasut, C.; Tsuda, T. Isoelectric Points Estimation of Proteins by Electroosmotic Flow: pH Relationship Using Physically Adsorbed Proteins on Silica Gel. *Chromatography* **2001**, *22*, 91-95.

[134] Petrelli, A.; Marconi, E.; Salerno, M.; De Pietri Tonelli, D.; Berdondini, L.; Dante, S. Nano-volume Drop Patterning for Rapid on-chip Neuronal Connect-ability Assays. *Lab Chip*. **2013**, *13*, 4419-4429.

[135] Jakschik, S.; Schroeder, U.; Hecht, T.; Gutsche, M.; Seidl, H.; Bartha, J. Crystallization behavior of thin ALD-AlO films. *Thin Solid Films* **2003**, *425*, 216-220.

[136] Wei, D. *et al.* Influence of Atomic Layer Deposition Temperatures on TiO<sub>2</sub>/n-Si MOS Capacitor. *ECS Journal of Solid State Science and Technology*. **2013**, *5*, 110-114.

[137] Macagno, V.; Schultze, J. The Growth and Properties of Thin Oxide Layers on Tantalum Electrodes. *Journal of Electroanalytical Chemistry and Interfacial Electrochemistry*. **1984**, *180*, 157-170.

[138] Wang, S.; Pan, L.; Song, J.; Mi, W.; Zou, J.; Wang, L.; Zhang, X.; Titanium-Defected Undoped Anatase TiO<sub>2</sub> with p-Type Conductivity, Room-Temperature Ferromagnetism, and Remarkable Photocatalytic Performance. *J. Am. Chem. Soc.* **2015**, *137*, 2975-2983.

[139] Teschke, O.; Ceotto, G.; de Souza, E. Interfacial Water Dielectric-permittivity-profile Measurements Using Atomic Force Microscopy. *PHYSICAL REVIEW E*. **2001**, *64*, 011605.

[140] Wolf, N.; Yuan, X.; Hassani, H.; Milos, F.; Mayer, D.; Breuer, U.; Offenhäusser, A.; Wördenweber, R. Surface Functionalization of Platinum Electrodes with APTES for Bioelectronic Applications. *ACS Applied Bio Materials*, **2020**, 3, 7113-7121.

## Acknowledgements

I wish to express sincere thanks to all the people during my PhD Work. Many thanks to the IBI-3 institute, collaborators, and the following people in particular:

Prof. Dr. Andreas Offenhäusser, thank you for providing us a platform for success in the academic environment, I really appreciate the kind atmosphere that you organized for the summer school and winter school, which makes me really comfortable and relaxed.

Prof. Dr. Roger Wördenweber, many thanks to you for the endless support that you offered me and the fact that you always see the positive part in any situation, which really inspired me and also is much valuable compared with so many lectures we got from the university. The coffee meeting and weekly work reports really helped me a lot not only with my English but also for the brilliant suggestions. Although the knowledge is already quite far more than enough, I would say, the way of doing science and achieving the knowledge is more important, after these four years training, finally I got it.

Dr. Dirk Mayer, thank you so much for the nice discussions, advices and guidance from the chemical part, it really helped quite a lot. You are like an old friend to me.

Special thanks must go to the contribution of Vanessa, Bettina, Timm, Pegah, Jiali and Frano. Thank you so much for everything you kindly offered during the cells experiment. Special thanks to Dr. Heinrich Hartmann, Dr. Uwe Breuer and Dr. Gregor Mussler for helping me with the experiments.

Many thanks to the cleanroom team: Dr. J gen Moers, Matthias Geitner, Michael Prömpers, Dr. Elmar Neumann, Stephany Bunte, Dr. Florian Lentz, the Helmholtz Nanoelectronic Facility (HNF) for productive cooperation, and Agnieszka Kurek and Harm Knoops from Oxford Instruments Plasma Technology for providing standard recipe parameters for the deposition of the different oxides.

My colleagues from oxide functional group for all the support and discussion. From the moment I enter the research group I felt welcomed and we had so many great memories. Rolf, thank you for your support during the last four years. Yang, thank you for searching

the apartment for me and the nice meals, you set a good example for us. Niko, thank you for everything, you are always being helpful and cheerful, not only sharing the sleeping room three times with me, finding fancy coins for me, also joining your 30<sup>th</sup> party, was really impressive, I will never forget we were waiting along the Rhein river at 2:00 am because of you. Sijia, we came together and were also from the same university in China, we also rode a bicycle in the middle of nowhere in the midnight together. I wish you everything goes well and never get lost again in the middle of nowhere, even if, better with a light. Manuel, Dennis and Pratika thank you for creating a nice working environment.

I hope I did not miss anyone, otherwise, please be happy that you will have my deepest thanks from my inner heart, as you know, it is far beyond any words.

Finally, I cannot be here and complete this thesis without all the love, support and motivation from my family, my parents and my sister, they are always patient to me, allow me to have a look overseas and willing to help me take care of my wife and my little baby during my last year work, my wife, really great to meet her in this world, she always calms me down when I am in bad mood, without her patience and love, I cannot manage this. For my grandfather, I wish he would be proud of me, being the first one who achieves the doctor degree in our family. Grandmother, you took care of me when I was young, I benefit so much from you, every time when I saw your smiling face, all the pressure I felt would be released. As for my little boy, I cannot wait a day to go back to spend all the time with you, daddy loves you.

We are now living in a society which is full of changes, information loadings and cross-subject problems, achieving a PhD degree should never be the end of my study, in fact, it will always remind me to have an independent thinking, the ability to learn the knowledge of other subjects, keep calm and always be optimistic to the future, therefore, I would thank Prof. Roger Wördenweber again for setting such a good example for us.

The road ahead will be long, our climb will be steep, but I will try my best.

路漫漫其修远兮，吾将上下而求索。

This thesis is dedicated to my grandfather for being my inspiration.



Band / Volume 232

**Optically induced magnetization reversal in Co/Pt multilayers**

Role of domain wall dynamics

U. Parlak (2021), ix, 162, XII pp

ISBN: 978-3-95806-536-9

Band / Volume 233

**Application of Silicon Photomultipliers in Neutron Detectors**

S. Kumar (2021), xxvi, 157 pp

ISBN: 978-3-95806-537-6

Band / Volume 234

**Towards Magneto-Elastomeric Nanocomposites with Supramolecular Activity**

L. S. Fruhner (2021), XVI, 213 pp

ISBN: 978-3-95806-538-3

Band / Volume 235

**Geometric and Electronic Properties of Heteromolecular Organic Monolayers on Noble Metal Substrates Studied by Photoemission Spectroscopy and X-ray Standing Waves**

G. van Straaten (2021), vii, 115 pp

ISBN: 978-3-95806-539-0

Band / Volume 236

**Nanoparticle assemblies: Order by self-organization and collective magnetism**

A. Qdemat (2021), xix, 282 pp

ISBN: 978-3-95806-542-0

Band / Volume 237

**$\gamma$ -Aminobutyrate as carbon and nitrogen source for *Corynebacterium glutamicum* and regulation of the catabolic genes by GabR**

L. Zhu (2021), 111 pp

ISBN: 978-3-95806-543-7

Band / Volume 238

**Single-Trap Phenomena in Nanowire Biosensors**

Y. Kutovyi (2021), 171 pp

ISBN: 978-3-95806-544-4

Band / Volume 239

**Single crystal growth and neutron scattering studies of novel quantum materials**

X. Wang (2021), VI, 145 pp

ISBN: 978-3-95806-546-8

Band / Volume 240

**Structure and Dynamics of Magnetocaloric Materials**

N. A. Maraytta (2021), vii, 146 pp

ISBN: 978-3-95806-557-4

Band / Volume 241

**Novel insights into the transcriptional regulation of cell division  
in *Corynebacterium glutamicum***

K. J. Kraxner (2021), V, 83 pp

ISBN: 978-3-95806-560-4

Band / Volume 242

**Interplay of proximity effects in superconductor/ferromagnet  
heterostructures**

A. Stellhorn (2021), ix, 219 pp

ISBN: 978-3-95806-562-8

Band / Volume 243

**Silencing and counter-silencing of the Lsr2-like protein CgpS in  
*Corynebacterium glutamicum***

J. Wiechert (2021), IV, 265 pp

ISBN: 978-3-95806-569-7

Band / Volume 244

**Molecular Layer Functionalized Neuroelectronic Interfaces:**

From Sub-Nanometer Molecular Surface Functionalization to  
Improved Mechanical and Electronic Cell-Chip Coupling

N. R. Wolf (2021), IV, 101, xx pp

ISBN: 978-3-95806-570-3

Band / Volume 245

**Surface Acoustic Waves in Strain-Engineered Thin (K,Na)NbO<sub>3</sub> Films:**

From Basic Research to Application in Molecular Sensing

S. Liang (2021), VI, 125 pp

ISBN: 978-3-95806-571-0

Band / Volume 246

**Tailoring neuroelectronic interfaces via combinations  
of oxides and molecular layers**

X. Yuan (2021), 113 pp

ISBN: 978-3-95806-572-7

Weitere **Schriften des Verlags im Forschungszentrum Jülich** unter

<http://www.zb1.fz-juelich.de/verlagextern1/index.asp>



Schlüsseltechnologien / Key Technologies

Band / Volume 246

ISBN 978-3-95806-572-7

Mitglied der Helmholtz-Gemeinschaft

